þÿGalaxy clusters strong gravitational lensing: toward t
images set detection via photometric analysis of HST images

Auteur : Mertens, Vincent
Promoteur(s) : Mahler, Guillaume
Faculté : Faculté des Sciences
Diplôme : Master en sciences spatiales, à finalité approfondie
Année académique : 2025-2026
URI/URL : http://hdl.handle.net/2268.2/25603

Galaxy clusters' strong gravitational lensing: toward the automation of multiple images set detection via photometric analysis of HST images

Master in Space Sciences - Research focus

Candidate:
Vincent MERTENS
Supervisor:
Dr. Guillaume MAHLER

Reading Committee:
Dr. Ludovic DELCHAMBRE
Pr. Emmanuel JEHIN
Dr. David LAGATTUTA
Pr. Dominique SLUSE

Academic Year: 2025 - 2026

Abstract

The detection of multiple images of background sources in strong lensing systems is a crucial step for cluster mass-modeling and the inference of cosmological constraints. This work presents an end-to-end pipeline designed as a first step toward the automated identification of multiple-image sets in crowded cluster fields, encompassing the entire analysis from multi-band source detection to spectral energy distribution (SED) similarity matching. Applied to HST images of the cluster SPT-CL J0356-5337, the pipeline effectively rejected the vast majority of the 19,925 initial candidate pairs, successfully identifying known lensed images as top mutual matches. However, the complex crowded field environment, characterized by flux contamination, deblending challenges, and noise-dominated faint sources, introduced a high-scoring tail of unlensed pairs. Rather than mere limitations, these high-scoring pairs serve as valuable diagnostics, highlighting the boundaries of global extraction parameters and the need for robust cluster-member decontamination. This interpretable and transparent approach offers a complementary framework that can serve as an insightful exploration tool and holds potential for scaling up to future wide-field lensing surveys.

Acknowledgments

This work represents the end of several years of study. Whether it was during my Bachelor's degree in Physics or this Master's in Space Sciences, I have never been alone, and it is deeply important to me to thank the people who have supported me along the way.

First and foremost, I would like to express my gratitude to my supervisor, Guillaume Mahler. Through his availability, his invaluable inputs, and his feedbacks, I was fortunate to have a deeply supportive and caring supervisor who made me feel guided throughout this project.

I would also like to thank the members of my lecture committee, Ludovic Delchambre, Emmanuel Jehin, David Lagattuta, and Dominique Sluse, for the time they dedicated to reviewing and evaluating this work.

I am also deeply grateful to my entire family, especially my father, for their unwavering support and trust throughout these long years.

Special and heartfelt thanks go to Laura, without whom this project would never have been possible. Thank you for your emotional support, your careful proofreading and corrections, and your help even when you could not understand a single word of the research topic.

Finally, I would like to thank the friends I made along the way for their daily support, presence, and all the good memories. Thank you to my fellow astrophysicists: Lucas, Alyssa, Morgane, Basile, Rosario, Mica, and many others. Thanks also to those wonderful people I met outside the university lecture halls: Florent, Maxime, Sofian, Romain, Matthieu and Maëlle.

À ma Mamy,
partie trop tôt pour voir l'accomplissement de mes études.
Ton souvenir m'accompagne chaque jour.

Contents

1 Introduction

Throughout History, mankind has always raised its head toward the sky. From the Mesopotamian civilizations to the 15^{th} century explorers, stars and the immensity of cosmos have been a source of questioning. They were sometimes regarded as divinities and often represent order and direction. Some have tried to translate the laws of this immensity into physical laws such as Galileo Galilei, Nicolaus Copernicus, Isaac Newton, or Edwin Hubble.

The foundations of our understanding rely on the theory of general relativity, formulated by Albert Einstein, which constitutes a general framework to describe gravitation. His theory postulates that a distribution of mass-energy curves space-time. In this curved space-time, light propagates following null geodesics. A consequence of this propagation is the manifestation of a phenomenon called strong gravitational lensing. When the background light source, the massive object acting as a lens, and the observer are aligned (or nearly aligned) along the line of sight, several null geodesics can connect the source to the observer. Each of these trajectories corresponds to a possible solution to the propagation problem, resulting in the formation of multiple images of the source. These images may appear distorted in different structures (arcs, ring, ..) and magnified depending on the mass distribution and the geometric configuration of the source-deflector-observer system. The study of such image configurations represents the most direct and precise approach to estimating mass and its spatial distribution. Strong lensing therefore constitutes an ideal probe of dark matter properties. Indeed, since dark matter interacts exclusively through gravity and not through electromagnetic interactions, it remains virtually undetectable by conventional observational means, which makes its study particularly challenging. However, modern astrophysics is entering an era of "Big Data" with the launch of large surveys such as Euclid. The amount of collected data is thus sky-rocketing.

Where a human could formerly spend days manually analysing a few images searching for cosmic mirages, the modern surveys are set to propose thousands of potential candidates. Confronted with this much available data, manual inspection becomes prohibitive in terms of time due to the human speed. The automation of detection and matching of multiple images, produced by gravitational lensing, thus represents a broader challenge in efficiently handling the ever-growing volume of astronomical data. This work contributes to the transition toward the automated analysis of large-scale astronomical data. We explore an alternative to computationally heavy, often complex, algorithms, focussing on a statistical photometric method. This master thesis aspires to test the viability of the detection of multiple images sets based solely on the photometric signature of galaxies to propose a light and transparent pipeline for the preliminary selection in the massive catalogs of tomorrow.

2 Galaxy clusters

2.1 Formation of clusters

Galaxy clusters are the largest structures in the Universe. However, to understand their formation, one must also consider the role of smaller-scale structures that serve as its building blocs.

2.1.1 Initial perturbations

In its early stages, the Universe was on average homogeneous and isotropic, consisting of a dense energetic fluid in expansion. This expansion is a dynamical process that is not fueled by internal reactions, but rather emerges as a geometric property of spacetime, following the Friedmann-Lemaître equations. During its initial moments, the Universe underwent an exponential expansion driven by the energy of a hypothetical scalar field known as the inflaton (Guth, 2000). Within the framework of quantum field theory, it is proposed that every field experiences microscopic fluctuations. Indeed, even in the quantum void, corresponding to the field configuration of minimal energy, the uncertainty principle dictates that the field's amplitude oscillates spontaneously. In the case of the inflaton, these variations create small energy variations. They were initially limited to subatomic scales but were stretched to macroscopic scales by the expansion to the point where some could not longer be compensated by the pressure (Liddle and Lyth, 2000).

Those fluctuations lead to density perturbations in the primordial photon-baryon plasma. Those perturbations are gaussian, adiabatic and have approximately a constant scale (Planck Colaboration et al., 2020). Because of this constant scale, the power spectrum is not concentrated on any particular scale and structures of every sizes get formed. The abundance of clusters directly depends on this initial distribution (Dodelson, 2003).
These perturbations are essentials as they will determine where matter will accumulate, the characteristic mass of the halos, and geometry of the cosmic web. Mass accumulates at the nodes of this so-called web, through gravitational interactions, and galaxies group themselves together to create the clusters of galaxies that we see today.

2.1.2 The role of Dark Matter

The current consensus in modern cosmology is that the baryonic matter only represents 4.9% of the total energy density of the Universe. However, to explain the formation of large structures, it is necessary to introduce the notion of dark matter, which accounts for 26.4% of the total energy density (Planck Colaboration et al., 2020). Unlike baryonic matter, it is theorized only to interact through gravity and not electromagnetic forces. For this reason, it cannot be observed directly and has to be studied through its gravitational influence on its surroundings.

It is worth noting that dark matter is thought to be non-baryonic, and therefore decoupled from baryon-photon interactions, allowing it to begin gravitational collapse earlier than baryonic matter. Various dark matter models have been proposed to account for this behaviour. Depending on its physical properties, notably its speed and interaction, dark matter may have very different effects on the growth of primordial perturbations. Among these models, "cold" dark matter (Peebles, 1982) is characterized by slow thermal speed, which prevents the small-scale perturbations from being erased, favoring thus the formation of structure. On the contrary, "hot" dark matter is composed of relativistic particles, whose high speed induces free-streaming, effectively erasing the growth of perturbations below a given scale. Relativistic neutrinos constitute an example of candidate for this type of dark matter.

Cold dark matter can also collapse around very small density fluctuations which is an indication of a hierarchical formation of halos, from the smallest to the largest (Peebles, 1980). The dark matter organizes itself in a large cosmic web where the nodes correspond to regions of maximal density.

2.1.3 Coupling of the baryons and linear growth

The evolution of the early Universe is marked by a pivotal transition known as the recombination, occurring approximately 380 000 years after the Big Bang. Before this epoch, the Universe consisted of an ionized plasma: photons, protons and free electrons. Photons were constantly scattered by free electrons through Thomson scattering. Because of this process, the baryon-photon fluid was highly coupled. The photon pressure was very high and prevented baryons from collapsing gravitationally, even within dark matter wells. The fluctuations of baryon density took the form of acoustic waves: Baryon Acoustic Oscillations (Hu and Sugiyama, 1996).

During the recombination, electrons and protons combined to form hydrogen causing the fraction of electrons to decrease drastically. The baryon-photon fluid decoupled and the photons began moving freely in the form of remnant radiation: the Cosmic Microwave Background (CMB).
Once the photon pressure disappeared, there was nothing left to oppose gravity, and baryons were free to collapse into the dark matter wells that had already formed. The areas of over density became the predecessor of baryonic halos, an accumulation of baryon in the gravitational potential of dark matter. They represent the first step toward galaxy and cluster formation. As they aggregated, these baryonic halos formed overly-dense regions known as proto-clusters, which were still undergoing collapse. The clusters observed nowadays are thus directly linked to dark matter wells and to photon-baryon decoupling.

The expanding Universe was, at that point, dominated by matter. The initial fluctuations grew under the effect of gravity. During this phase and for small perturbations $\delta \equiv \frac{\Delta\rho}{\rho} \ll 1$, we have that $\delta \propto a(t)$, where a is the scale factor. When $\delta \sim 1$, the linear regime is not valid anymore as the density perturbations cannot be considered small.

2.1.4 Non-linear collapse

After the previous phase of linear growth, some of the perturbations reached a density of $\delta \sim 1$. This is enough to classify those regions as more than just perturbations. The linear theory became invalid and massive halos became gravitationally bound. They could be considered as single objects due to their own gravity surpassing the forces tending to separate them (e.g. their speed). The moment where the gravity begins to outweigh the local expansion is called the turn-around. This happened when the density reached a critical threshold. After this turnaround, the region collapsed spherically, which is a theoretical approximation of reality, and reached dynamical equilibrium through virialization. The result was a stable halo that can be well modeled through N-body simulations (Press and Schechter, 1974). The baryons fell into these halos to form a hot gas, effectively becoming the initial environment of galaxies and clusters (Kravtsov and Borgani, 2012; Peacock, 1998).

2.1.5 Hierarchical formation and mergers

The standard cosmological model, known as the ΛCDM, describes the evolution of the Universe within the framework of general relativity assuming a dominant contribution from cold dark matter and a cosmological constant associated with dark energy, which drives the expansion. Within this framework, structure formation proceeds hierarchically (bottom-up formation), as small-scale density fluctuations collapse earlier and subsequently merge to form larger systems.

The dark matter halos grow through two main processes:

1. Smooth accretion: In-falling of dark matter and baryonic matter in halo following the cosmic string.

2. Catastrophic merger: Two massive halos merge to create a larger one which increases its mass significantly.

Mergers can be classified as minor and major depending on the mass ratio. Over time, repeated mergers led to the formation of increasingly massive systems, eventually leading to the creation of galaxy clusters. They progressively virialized, reaching dynamical equilibrium between gravitational collapse and internal motions (Kravtsov and Borgani, 2012).

2.2 Properties of clusters

Galaxy clusters are the most massive gravitationally bound structures in the Universe. Situated on top of the structure formation hierarchy when it comes to the ΛCDM model, they are the products of the gravitational collapse of primordial density fluctuations as well as successive accretion and fusion processes forming zones of galactic over-densities. Galaxies within clusters have peculiar velocities relative to the overall cluster motion. The number of galaxies in a cluster is characterized by the richness. It can be classified as rich when there are more than 50 to 100 galaxies in a given radius and above a certain luminosity. The total mass of a rich galaxy cluster can reach $10^{14} - 10^{15}\ M_{\odot}$. This mass is distributed among different elements (Bahcall, 1996; Lin and Mohr, 2004; Planck Colaboration et al., 2020):

1. Galaxies and stars ($\sim 1 - 3\%$ of total cluster mass)
2. Intracluster medium ($\sim 12 - 15\%$ of total cluster mass)
3. Dark matter halo ($\sim 85\%$ of total cluster mass)

Because galaxy clustering occurs over a large range of spatial scales, there is no unique definition of a "rich" cluster. The definition depends on the observational criteria used to identify the systems. Clusters were historically cataloged by G. Abell (Abell, 1958), who compiled a catalog of 2,712 galaxies following a precise criterion. A cluster had to contain at least 50 galaxies in the magnitude range[1] $[m_3\ ,\ m_3 + 2]$, within a radius $R_A = \frac{1.7}{z}$, known as the Abell radius. The catalog was completed for clusters in the redshift range $0.02 < z < 0.2$. Later, Fritz Zwicky refined this definition in his own catalog (Zwicky et al., 1961). In this case, 50 galaxies had to lie in the magnitude range $[m_1\ ,\ m_1 + 3]$. Instead of adopting a fixed radius, the cluster boundary was defined by the contour where the galaxy surface density reached twice the background density. Because these criteria are less restrictive than Abell's, this catalog includes more galaxies.
Following these early catalogs, cluster searches were progressively extended to deeper and larger parts of the sky. Improved surveys and, later, digital sky surveys enabled the construction of more complete catalogs (Wen and Han, 2024; Wen et al., 2012) and the detection of clusters at higher redshifts. Furthermore, clusters began to be identified through other observational signatures such as their X-ray emission.

Let us now dive into the main properties and characteristics of galaxy clusters.

[1]The m_i notation refers to the apparent magnitude of the i-th brightest galaxy

2.2.1 Thermodynamics of the intracluster medium

The space between the galaxies in a cluster is filled with a hot plasma, known as the intracluster medium (ICM). It accounts for most of the baryonic mass in a cluster, and is mainly composed of ionized hydrogen, helium with a few metals. It can reach temperatures up to $10^8 K$ (Sparke and Gallagher, 2007). Two main distinct models proposed an origin of this medium.
The first one is the infall model of primordial gas. Intergalactic gas that was not part of any structure falls into the cluster due to gravitation (Gunn and Gott, 1972). This gas is then heated by compression and shock waves. As simulations have shown, a nearly stable gas is formed after infalling (Cowie and Perrenod, 1978). Although the luminosity remains roughly constant, it can evolve if the cluster potential changes over time due to potential shock heating leading to changes in density and temperature.
The second model makes the hypothesis that the presence of metal in the ICM is an indicator that it has been enriched by stars and galaxies. Gas can be expelled by supernovae, collision of galaxies or even ram pressure stripping. Models indicate that galaxies can expel up to $\sim 30 - 50\%$ of their stellar mass in the ICM (Biermann, 1978).
The ICM could thus originate from a mix between mainly primordial gas that fell into a cluster as well as a part of gas ejected from galaxies.

Hot plasma is known to be subject to thermal bremsstrahlung. It refers to the radiation produced by the deceleration of a charged particle when it hits another charged particle. Its kinetic energy is thus converted into radiation. Observations of this radiation allow us to determine physical properties of the plasma, such as temperature and density (Sparke and Gallagher, 2007). Originally, the first detection of extragalactic X-ray radiation was M87 in the Virgo cluster (Bradt et al., 1967), followed by the Perseus and Coma clusters. Different satellites were then used, such as the Einstein Observatory, leading to the first results of the observation campaign:

1. The clusters of galaxies are very common and bright sources of X-ray radiation (10^{44} - 10^{46} erg s^{-1}).

2. The emission is extended ($\sim$ hundreds of kpc).

3. The absence of strong low-energy absorption points to negligible dust extinction, consistent with emission from a diffuse, optically thin plasma.

4. No important temporal variability, pointing to a stable emitting medium.

These properties suggest an extended, low-density emitting medium, characteristic of diffuse plasma commonly found in the Universe (Forman et al., 1972).
Apart from the thermal bremsstrahlung, different mechanisms have been proposed to explain the origin of the X-ray emission. Among them, we find the emission from stellar sources but it was later discarded as the produced emission would be granular and too weak. The typical temperature of the accepted bremsstrahlung radiation is close

to $10^7 - 10^8$ K, producing an exponential spectrum from a diffuse and smooth emission. This origin of the emission is supported by the presence of emission lines corresponding to heavy elements (ionized iron) and the distribution of the gas similar to that of the galaxies (Sarazin, 1986; Sparke and Gallagher, 2007).
Another property of the ICM lies in its influence on the cosmic microwave background. Indeed, the CMB is present behind every cluster in the Universe. It is characterized by the emission spectrum of a black body of $2.7\,K$, and considered an observable remnant of the recombination period. As CMB photons pass through a cluster, they scatter of the high-energy electrons of the ICM. Since the electrons are more energetic, they transfer energy to the photons through inverse Compton scattering. The spectrum of the CMB is thus modified in the direction of the cluster. During an average diffusion, the modification on the spectrum depends on the frequency and can be characterized as $\frac{\Delta\nu}{\nu} = \frac{4kT_e}{m_e c^2}$. This results in a decrease of the intensity at low frequencies (referred to as microwave diminution) and increase at high frequencies due to the "displacement" of low energy photons toward high energy (Sunyaev and Zeldovich, 1972; Zeldovich and Sunyaev, 1969). These temperature distortions in the CMB can be used to detect high-redshift clusters of galaxies (Staniszewski et al., 2009).

The ICM evolves under the influence of radiative cooling and heating processes. The current state of the cluster reflects a balance between these processes. The main mechanism responsible for the cooling of the ICM is the X-ray emission of the hot gas due to bremsstrahlung and atomic line emission. If the cooling time in the center is smaller than the age of the cluster, the gas may start to cool down. In order to counter this cooling, different heating mechanisms have been identified. Historically, it was thought that gas from the outer layers would flow toward the center to maintain hydrostatic equilibrium. This would have led to new areas of star formation (Fabian, 1994; Sarazin, 1986). However, observations did not align with this theory as the cooling flows could not be observed as predicted (Peterson et al., 2003). This leads to classic cooling flow being highly suppressed or counteracted. Clusters with such cooling are called cool-core clusters. Currently, cluster cores are believed to undergo self-regulated heating and cooling. The dominant heating mechanism is thought to be feedback from active galactic nuclei (AGN). Gas cooled by radiation starts to fall into the supermassive black hole of the galaxy through accretion. It then expels part of the gained energy in the shape of relativistic plasma jets. These jets create shock-waves and hot gas bubbles in the ICM which heats the surrounding medium and stops the cooling of the ICM (Fabian et al., 2003; McNamara and Nulsen, 2007).

2.2.2 Structure of matter and density profiles

The gravity of the dark matter halo essentially defines the shape and dynamics of the cluster as it encompasses most of the galaxies and the ICM, and holds them in the cluster. By definition, as it is formed through the hierarchical merging of smaller dark matter structures, it does not interact electromagnetically and cannot thus be observed. However, its presence can be deduced from its different gravitational effects:

- By measuring the individual speeds of galaxies in a cluster, we conclude that they should separate due to their high speeds, ultimately dislocating the cluster. However, the rotation speed of the galaxies at large distance from the cluster remains constant (flat rotation curve). If it holds together, it is due to an "invisible mass" that exercises enough gravitational attraction to hold the galaxies together.

- The ICM in galaxy clusters is at hydrostatic equilibrium and at high temperature. In order for it to stay that hot and compressed without drifting away in space, a substantial amount of pressure is needed. The total mass of gas and galaxies is not enough for it to be the case and the dark matter is thought to provide that strong needed attraction.

- Gravitational lensing is the most direct method to probe the dark matter halo as it does not rely on supposition of the ICM. This effect will be further addressed in a following section. Gravitational lensing is essentially the deviation of light rays due to the presence of mass. It is a strong indicator of the presence of the halo as the observed deviation is more important than what the integrality of the baryonic matter could cause. Because the curvature of space-time only depends on the total mass, the observed deviation of distant galaxies allows to map directly the halo.

The dark matter halo is generally more extended than the ICM and the galaxies, with a density that decreases toward the exterior. Halos are continuously evolving systems. They cycle through hierarchical formation via fusion and accretion then gravitational relaxation toward a quasi-stable state (Kravtsov and Borgani, 2012).

Different processes and properties can be stated to shape the internal structure of the halo. In order to go from a disorganized cloud of particles to a stable halo, two processes have been identified. The first one is a violent relaxation (Kravtsov and Borgani, 2012; Lynden-Bell, 1967). Since the dark matter particles do not collide, they relax and stabilize through variations in the gravitational potential. This potential varies rapidly and the particles exchange their speed in order to reach an equilibrium. It is said to be violent as it is a rapid process that happens at the scale of the cluster collapse. The second process concerns the interaction between dark matter and baryonic matter, namely the adiabatic contraction. When gas cools and aggregates to form a galaxy, its gravity increases in the center. The halo responds to this modification by contracting slowly and deforming itself. The halos of dark matter then reach, after hierarchical collapse, a stable profile of density, dispersion of speed and shape.

The density distribution in the stabilized halos is thought to follow the same universal law. The halos end up having a dense core and diffuse periphery, stabilized by the orbital motion of their particles. A well known density profile is the Navarro-Frenck-White profile (Navarro et al., 1995, 1996, 1997) and is noted:

$$\rho_{NFW}(r) = \frac{4\rho_s}{\left(\frac{r}{R_s}\left(1+\frac{r}{R_s}\right)^2\right)}$$

R_s is the scaling radius and represents the transition between the core and the periphery of the halo. ρ_s is the characteristic density related to the concentration of the halo. It represents the density at radius R_s which normalizes the equation. This expression can be re-expressed in a cosmological way by linking it to global density of the Universe as:

$$\frac{\rho(r)}{\rho_{crit}} = \frac{\delta_c}{\left(\frac{r}{R_s}\right)\left(1+\frac{r}{R_s}\right)^2}$$

ρ_{crit} is the critical density of the universe, or the density needed for it to be flat, and δ_c represents the characteristic density parameter, expressing how much denser the center of the halo is, compared to the average density of the Universe.
The concentration translates the relation between the density of the core and its periphery. The NFW profile is characterized by a logarithmic slope of -1 in the center, leading to a cusp or "peak" at the center and a slope of -3 at the periphery, meaning that the density drops fast. This profile has been introduced following multiple N-body simulations. It has the benefit to be rather robust to variation of the type of halos.
As the NFW profile is characterized by a peak in density in the center of the halo, the Einasto profile is characterized by a flatter center. While the first one was defined by two distinct slopes, the second is a continuous curve. It is defined by:

$$\rho_E(r) = \rho_s exp\left[\frac{2}{\alpha}\left(1-\left(\frac{r}{r_s}\right)^{\alpha}\right)\right]$$

where α is an additional parameter that controls the logarithmic slope depending on the radius which lies between $0.16 - 0.3$, better capturing the subtleties of the density variation than the NFW profile (Einasto, 1965; Kravtsov and Borgani, 2012; Merritt et al., 2006).
The shape and density profile of the halo are partially inherited from the shape of the initial over-densities. The steeper they are, the more concentrated the halo will be. Once that halo is formed, the accumulation of matter continues through accretion. When those particles fall toward the center, the already present dark matter contracts to compensate the increase in gravity. It is also worth noting that major mergers redistribute a fraction of the mass but do not alter the global shape of the profile. Indeed, after a violent collision,

the final halo density profile has an NFW shape. As the collision redistributes a part of the energy, gravitational collapse ultimately imposes its universal shape, highlighting the robustness of the profile (Kazantzidis et al., 2006; Lithwick and Dalal, 2011).
There is a relation between the total mass of a dark matter (DM) halo and the redshift of its cluster. An old cluster, at high redshift, was formed during a time where the universe was smaller. It thus attracts much denser matter therefore conferring a compact core. Nowadays, at lower redshift ($z = 0$), the halo attracts more diffuse matter. However, the concentration varies weakly with the redshift (Bullock, 2002; Kravtsov and Borgani, 2012).

A last step in the analysis of the dark matter halos properties would be to summarize their geometry. In reality, halos are triaxial ellipsoids as dark matter does not fall toward the center uniformly but is channelled by cosmic filaments and arrives along privilege directions, hence the stretched shape. Halos do not flow randomly in space but tend to be found at the nodes of a giant web of matter: the cosmic web. Regarding their orientations, the longest axis of the halo tends to point toward the filament that supplies it. Depending on the direction of observation, the light-ray deviation will be different, introducing a bias in lensing method for mass estimation if a spherical halo is considered (Jing and Suto, 2002; Kravtsov and Borgani, 2012).

2.2.3 Scaling relations

Scaling relations are widely used in astrophysics to connect observable quantities to underlying physical properties. In the case of galaxy clusters, they are particularly useful, as key properties such as the mass are difficult to measure and are dominated by dark matter. These relations therefore provide an indirect but powerful way to probe the physical properties of clusters.

In order to properly introduce those scaling relations, we need to introduce the self-similar model. It states as hypothesis that clusters are formed from initial scale-free conditions with a single spherical collapse due to the gravitational potential. All the clusters at a same redshift are identical after rescaling and their properties follow simple power laws with mass and redshift. The collapsing region virializes, and the velocities of the different components reach equilibrium with the gravitational potential (Böhringer et al., 2012; Kaiser, 1986). The virialized halo can be delimited via the virial radius R_Δ, defined as a dimensionless number Δ multiplied by the critical density of the universe ρ_c. We have:

$$\frac{M_\Delta}{\frac{4}{3}\pi R_\Delta^3} = \Delta \rho_c(z)$$

With $\Omega_M = 0.3$ and $\Omega_\Lambda = 0.7$, we find $\Delta_{vir}(z = 0) \approx 100$ (Bryan and Norman, 1998). An over-density of 100 means that the enclosed region is 100 times denser than the critical density of the Universe. Clusters can be considered self-similar once they are scaled to a constant over-density radius at all redshifts. A standard scale for X-ray observations is taking $\Delta = 500$, corresponding to R_{500}, to measure the properties of the ICM. The self-similarity hypothesis leads to the existence of relations between the properties of the cluster in the form of a power law $Y = AE(z)^{\gamma}X^{B}$ where A, B, and γ represent the normalization, slope and redshift evolution respectively (Lovisari and Maughan, 2022). $E(z)$ describes the redshift evolution of the Hubble parameter $\left(\frac{H(z)}{H_0}\right)$. Some relations will be listed below.

- **M_{gas}–M relation**:

  $$M_{gas} = f_{gas}M \quad \text{(general)}$$

  Self-similar:

  $$M_{gas} \propto M\,E(z)^{0}$$

  This implies that clusters contain approximately the same baryonic fraction (f_{gas}) independently of redshift.

- **T_X–M relation**:

  $$T_X \propto \frac{M}{R} \quad \text{(virial theorem)}$$

  Self-similar:

  $$T_X \propto M^{2/3}E(z)^{2/3}$$

  This expression is valid if the ICM is isothermal and in virial equilibrium. More massive clusters are hotter, and at fixed mass, high-redshift clusters are hotter because the Universe was denser.

- **L_X–M relation**:

  $$L_X \propto \rho_{gas}^{2}T_X^{1/2}R^{3}$$

  Self-similar bolometric:

  $$L_X \propto M^{4/3}E(z)^{7/3} \quad \text{(massive, bremsstrahlung dominated)}$$

  Self-similar soft band:

  $$L_X \propto M\,E(z)^{2}$$

  For low-temperature systems, line emission modifies the temperature dependence. It is worth noting that this relation depends highly on the gas density, since bremsstrahlung emission scales with the square of the electron density.

Among these relations, a mass proxy is an observable quantity that is strongly correlated with the cluster mass and can be directly measured (unlike the total mass). The scatter defines how the relation between the proxy and the actual mass of the cluster is precise. Low-scatter mass proxies therefore provide precise and robust estimates of the cluster mass. These relations are:

- **$\boldsymbol{Y_X - M}$ relation**:
  $$Y_X \equiv T_X M_{\mathrm{gas}} \propto E(z)^{2/3} M^{5/3}$$
  Y_X is proportional to the total thermal energy of the intracluster medium and serves as a low-scatter mass proxy robust to cluster dynamical state and ICM assumptions.

- **$\boldsymbol{Y_{SZ} - M}$ relation**:
  $$Y_{SZ} \propto E(z)^{2/3} M^{5/3}$$
  Like Y_X, it represents the total thermal energy of the cluster but measured through distortions of the CMB rather than X-ray emission. Because CMB photons interact with the ICM via inverse Compton scattering, the CMB spectrum is distorted in the direction of the cluster. This makes the Sunyaev-Zel'dovich effect a unique proxy, as its surface brightness is independent of the redshift. It acts as a low-scatter mass proxy although it is affected at some level by cooling and feedback processes when simulated.

(Kravtsov and Borgani, 2012; Lovisari and Maughan, 2022)

3 Foundations of gravitational lensing

The origin of gravitational lensing can be traced back to the 1930s when Fritz Zwicky suggested that galaxy clusters were dominated by an invisible mass. He predicted that the deviation of these light rays would allow to measure the clusters mass and amplify objects located far away (Zwicky, 1937). The modern theory of lensing was then reformulated in the 1960s but became truly observational with the discovery of the first doubly lensed quasar (Walsh et al., 1979). Even though they were considered too diffuse, clusters were recognized as effective lenses with the introduction of the cold dark matter paradigm. The discovery of giant arcs revealed the strong lensing regime, which will be deeply defined later in this section, while the statistical survey of background galaxies reveals the weak lensing regime. Later, the development of the CCD and deployment of the Hubble Space Telescope allowed the identification of multiple systems of multiple images in the heart of galaxy clusters. Lensing via galaxy clusters is nowadays a central tool to probe the distribution of dark matter, to test models of structure formation, and to study high redshift background galaxies (Kneib and Natarajan, 2011).

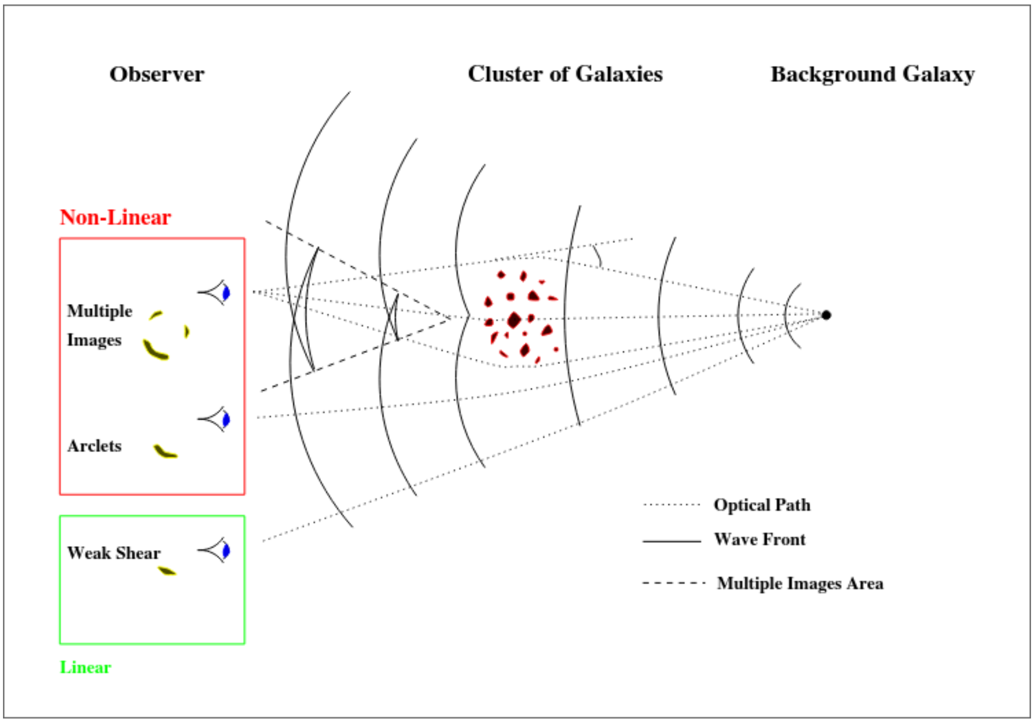

Figure 1: Schematic representation of the different gravitational lensing regimes (Kneib and Natarajan, 2011)

The theory behind gravitational lensing can be introduced and applied to clusters of galaxies. Being extremely massive, they deform space-time locally as stipulated by general relativity. The light emitted by a background source, a galaxy, is deviated while trying to travel through the cluster. In the most massive clusters, the center density can produce multiple images of a same source which can sometimes appear in the form of arcs, characteristic of strong lensing regime. The strongly lensed galaxies thus appear elongated, amplified and tangentially aligned. The observed shape is a combination of the original shape and the distortion due to the clusters presence. A less precise alignment will lead to individually undetectable distortions and require the use of statistical analysis, characteristic of the weak lensing regime (Figure 1).

3.1 Thin lens approximation and equation

Gravitational lensing theory rests on the cosmological principle which stipulates that the Universe is homogeneous and isotropic at large scales. This hypothesis is correct for the scales governed by long range ($\sim Gpc$) gravitation. This basically implies that we do not occupy a privileged position in the Universe. By making this assumption, the solution of the Einstein equation is limited to the Friedman-Lemaître-Robertson-Walker (FLRW) metric. It is described by the scale factor $a(t)$, describing the distance between objects as spacetime expands, and a curvature parameter k, describing the geometry of the space. This metric allows for the measurement of cosmological distances.

$$ds^2 = c^2 dt^2 - a^2(t)\left(\frac{dr^2}{1-kr^2} + r^2 d\theta^2 + r^2 \sin^2\theta d\varphi^2\right)$$

Any concentration of mass, whether it is stars, galaxies or clusters, disturbs locally the cosmological metric. Under the weak field approximation, the general relativity equation can be effectively reduced in a simple gravitational potential that allows the computation of the light deviation as if the concentration of mass was a single lens. It makes the assumption that the gravity is not too strong, approximating the metric to a flat field with a small local perturbation. It also assumes that the local mass concentrations distribution does not change while being crossed by light (Weinberg, 1994).
This deviation of light can be simplified in order to be studied through the thin lens approximation. It breaks the problem down to a single flat lens that bends the light rays travelling from a background source to an observer (Figure 2). The deviation then depends on the projected mass distribution of the lens and the internal distance in the observer-lens-source system. The deviated photons follow zero geodesics and the deviation can be obtained by applying Fermat's potential, stating that the light will follow a path of stationary travel time. The equation describing the whole system can be written (Kneib and Natarajan, 2011):

$$\boldsymbol{\theta}_I = \boldsymbol{\theta}_S + \frac{D_{LS}}{D_{OS}}\boldsymbol{\alpha}(\boldsymbol{\theta}_I)$$

The angle of deflection $\alpha(\theta_I)$ is linked to the projected gravitational potential. We can obtain the following expression, where $\vec{\nabla}_\varphi$ is the lens potential, a simplified version of the projected potential that contains the cosmological distance (Weinberg, 1994):

$$\boldsymbol{\theta}_S = \boldsymbol{\theta}_I - \boldsymbol{\nabla}\varphi(\boldsymbol{\theta}_I)$$

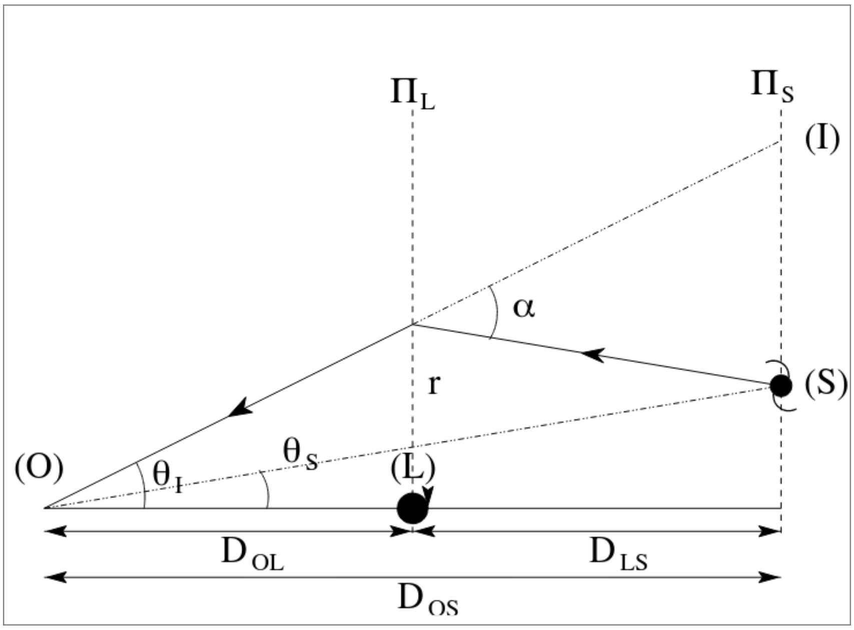

Figure 2: Geometric representation of the thin lens approximation (Kneib and Natarajan, 2011).

3.2 Local quantities and image distortions

The lensing can be described as a mathematical application that links the source plan to the image plan. In the case of a thin lens, this transformation is described locally by a Jacobian matrix called the amplification matrix.

$$\frac{d\boldsymbol{\theta}_S}{d\boldsymbol{\theta}_I} = \mathbf{A}^{-1} = \begin{pmatrix} 1-\partial_{xx}\varphi & -\partial_{xy}\varphi \\ -\partial_{xy}\varphi & 1-\partial_{yy}\varphi \end{pmatrix} = \begin{pmatrix} 1-\kappa-\gamma_1 & -\gamma_2 \\ -\gamma_2 & 1-\kappa+\gamma_1 \end{pmatrix}$$

This matrix links the small displacements in the plane of the image to those in the plane of the source. The amplification matrix can be written as a function of two physical quantities: the convergence κ and the shear γ. The convergence represents the change in size and luminosity of the image without changing its shape. It is linked to the lens potential through $\kappa = \frac{\Delta\varphi}{2}$. The shear vector changes the shape of the object and is responsible for the appearance of arcs. It is defined as $\gamma_1 = \frac{\partial_{xx}\varphi - \partial_{yy}\varphi}{2}$, $\gamma_2 = \partial_{xy}\varphi$.

The convergence can be rewritten as the ratio between the projected mass density and the critical surface density Σ_{crit}. The latter can be seen as the minimal density needed for a cluster to produce a "strong lensing effect". It depends on the angular distances in the observer-lens-source system and is defined as:

$$\Sigma_{\text{crit}} = \frac{c^2}{4\pi G}\frac{D_{OS}}{D_{LS}D_{OL}}$$

As previously mentioned, this mathematical quantity represents a criterion for the existence of a strong lensing region. When the surface density reaches or exceeds Σ_{crit}, the strong lensing regime is reached. These critical regions in a cluster are thus regions where the convergence is close to or greater than one. The background galaxies crossing these regions have a strong possibility to be multiply imaged. The density required for the appearance of this regime is much greater than the critical cosmological density.

The magnification μ, corresponding to the amplification of luminosity and size, is given by the determinant of the amplification matrix and thus depends on the convergence κ and the shear γ.

$$\mu^{-1} = \det(\mathbf{A}^{-1}) = (1-\kappa)^2 - \gamma^2 = (1-\kappa)^2(1-g^2)$$

The quantity noted $g = \frac{\gamma}{1-\kappa}$ is the reduced shear. It is what scientists actually measure when observing the shapes of the galaxies as it is not simple to separate shear from the convergence simply by observing an image. Looking at the definition of the magnification, we can notice that an infinite magnification occurs when an eigenvalue of the matrix disappear which corresponds to $g = 1$. This defines what is called critical lines in the image plane. The mapping of these critical lines on the source plane defines the caustic lines which, unlike critical lines, can intersect. Two main types of critical lines can be identified. The first one is tangential critical lines, producing tangential arcs and giant arcs. The second one is radial critical lines, producing radial arcs closer to the center.
For a circularly symmetric mass distribution, the critical lines are circular. The tangential caustic collapses to a single point and the radial critical line lies always inside the tangential one. For this type of mass distribution, the projected mass lying inside a given radius r is given by:

$$M(r) = \frac{c^2}{4G}\frac{D_{OS}D_{OL}}{D_{LS}} r\partial_r\varphi(r) = \pi\Sigma_{\mathrm{crit}} r\partial_r\varphi(r)$$

The Einstein radius r_E corresponds to the tangential critical radius and encloses a mean surface density equals to the critical surface density Σ_{crit}. It simplifies as:

$$M(r_E) = \pi\Sigma_{\mathrm{crit}} r_E^2$$

This radius increases with the mass concentration and depends on the redshifts of the lens and the source via Σ_{crit}.
The radial critical line is sensitive to the slope of the mass profile which makes it a strong constraint on the central mass distribution. In a realistic (non-circular) cluster, critical and caustic lines become complex and cannot be derived easily. They require numerical methods. Their identification is a key step to constrain the mass and concentration of a cluster (Kneib and Natarajan, 2011).

3.3 Multiple images

The critical lines in a gravitational lensing system are not directly observable. However, their presence is revealed by the presence of multiple-images located on either side of them. The tangential arcs are found close to the tangential critical lines, while radial arcs form near radial critical lines. In simple systems, we can identify radial and tangential pair configurations (Miralda-Escude and Fort, 1993). Depending on the lens mass distribution, a single background source can produce triplets, quadruplets, quintuplets or higher-order image systems. The number of multiple-images corresponds to the number of solutions of the lens equation. The catastrophe theory predicts that crossing a caustic in the source plane will create two additional images (Schneider et al., 1992; Zeeman, 1976). For non-singular mass distributions, gravitational lensing formally produces an odd number of images. However, in practice, some of them are demagnified or obscured, especially the central image hidden by the brightest cluster galaxy, making them difficult to detect.

The symmetry of multiple-images is determined by the sign of the eigenvalues of the magnification matrix, which defines the image parity. If their product is negative, the image undergoes a mirror inversion corresponding to a change of parity. It can be used to model with precision the shape of the lens by comparing the orientation of the different detected images. Three observable parity configurations exist for simple mass distributions: $(+,+)$, $(+,-)$ and $(-,-)$ (Schneider et al., 1992). A parity flip occurs each time an image crosses a critical line, corresponding to a sign change in one eigenvalue. Mirror symmetry between images, one appearing flipped and the other not, is a powerful and robust criterion to identify multiple-image systems.

Historically, multiple-images were first identified within giant arcs, however they do not necessary correspond to multiple images of a single source. Some giant arcs are single highly magnified images, while others may consist of several arclets from different background sources at different redshifts, distinguishable by their colors. Morphological similarity, like the repeated internal structure, is a key criterion to associate images to a same source. It is worth noting that gravitational lensing is achromatic which means that multiple images of the same source exhibit similar colors across photometric bands. They can also be identified through strong emission in specific wavelength ranges (infrared), where the same source appears repeatedly. The most secure confirmation of a multiple-images system is achieved through cluster lens modeling, which will test whether candidate images are consistent with a single source. Lens models can predict the position of counter-images and provide redshift estimates for multiply-lensed sources. For large cluster samples, there is a strong need for automated identification methods based on morphology, color information, and lensing constraints (Kneib and Natarajan, 2011).

3.4 Applications of strong gravitational lensing

3.4.1 Mass distribution and modeling

One of the main applications of gravitational lenses are their use for the mass distribution modeling of the cluster. It consists in constructing the gravitational potential of the galaxy clusters so that it can reproduce the observed lensing effects, such as the positions and shapes of the multiple images. In other words, a defined mass profile is adjusted on the cluster. Two different approaches exist to accomplish this: parametric models, based on predefined physical profiles, and non-parametric models, which are more flexible as they are less constrained (Kochanek, 2004).
In parametric approaches, the mass is represented by a limited number of distinct structures. These structures include both small scale components (galaxies) and large scale components (dark matter, ICM), which are described by several parameters that depend on the defined mass profile. A simple model often consists of a singular isothermal sphere (SIS) characterized by a constant velocity dispersion (σ) as well as an $r = 0$ singularity as:

$$\rho(r) = \frac{\sigma^2}{2\pi G r^2}$$

Other more complex profiles can be used such as the NFW mass profile introduced in a precedent section (see Section 2.2.2). These sophisticated profiles also come with an additional number of parameters. In the case where observations are limited, it is better to use simple models in order to avoid the imbalance between the number of parameters and available constraints (Kochanek, 2004; Kravtsov and Borgani, 2012).

It is the positions of the multiple images that constrain the mass modeling. However, to represent a cluster accurately, complex models are required and a single constraint is not enough. It can be explained by the inherent structure of the galaxies. Indeed, their mass is mainly dominated by dark matter halos (Kneib and Natarajan, 2011). In clusters, these halos are modified by the environment as they are partially stripped by tidal forces which limits their extension (Natarajan et al., 2009). Strong lensing features prove that individual galaxy-scale perturbations and dark matter halos affect the observed arc configurations and thus require explicit inclusion in cluster mass models (Kneib et al., 1996). A cluster is therefore modeled through the combination of a global halo, representing the dark matter and the ICM, and multiple sub-halos associated with galaxies (Kneib and Natarajan, 2011). Although each galaxy has a limited local effect, their cumulative effect represents a non-negligible part of the mass and improves the reproduction of the images (Natarajan et al., 2007). To make use of the limited constraints, namely the set of multiple images, the complexity can be reduced by linking the properties of the halos to the luminosities of the galaxies through scaling relations.

Modern methods in parametric modeling rely on a Bayesian inference framework, in which prior distributions and observational data are combined to constrain the model. This method is particularly suitable when the data alone is not sufficient to constrain every parameters. The prior distributions therefore allow to limit the degeneracy. It is thus very relevant in strong lensing where the number of observational constrains is often limited.
This Bayesian formalism takes its name from the Bayes theorem, expressed as:

$$\mathrm{P}(p|D,M) = \frac{\mathrm{P}(D|p,M) \times \mathrm{P}(p|M)}{\mathrm{P}(D|M)}$$

In this expression, p represents the parameters, D the data and M the model. The different terms on which the Bayesian framework relies can be identified as the likelihood $\mathrm{P}(D|p,M)$ (model-data fit), the prior $\mathrm{P}(p|M)$ (Probability Density Function of the parameters), the evidence $\mathrm{P}(D|M)$ (marginal likelihood), and the posterior $\mathrm{P}(p|D,M)$. The best models are the ones that maximize the posterior probability, ensuring the coherence with the priors. The evidence plays a key role by favoring simple models as it acts as an Occam's razor. In practice, MCMC (Markov chain Monte Carlo) based methods have been implemented to sample the parameter space and account for uncertainties which allows to identify and quantify the degeneracies between the parameters and the model. The main algorithm used nowadays is named *Lenstool* and was the product of a collaboration between different researchers (Jullo et al., 2007).

In parallel, non-parametric methods have been developed to model the mass distribution of clusters and to deal with the increasing amount of constraints, namely multiple images, provided by deep space observations with space telescopes (Broadhurst et al., 2005; Saha and Williams, 1997). Their main advantage is their high flexibility, allowing the exploration of complex mass distributions (Bradač et al., 2006). One of the main techniques consists of representing the mass distribution using a pixel grid or radial basis functions, such as Gaussians, rather than analytical profiles. This method provides a support where each pixel is technically independent from the others until regularisation. Their main problem is that the amount of freedom given may result in degeneracies where multiple models can explain the solutions rendering the identification of the right solution tedious. Different constraints, such as the aforementioned regularisation or physical limitations, may thus be introduced in order to get credible results. A limitation of such methods is that they often neglect part of galaxy halos yet important in explaining the lensing effects (Saha and Williams, 1997). A solution may lie in hybrid models that combine the flexibility of non-parametric models with parametric halo modeling for a more realistic representation which are then fed to MCMC algorithms (Jullo and Kneib, 2009).

3.4.2 Investigate the nature of dark matter

Gravitational lensing, whether it is in the strong or weak lensing, is a useful tool when it comes to studying dark matter. As mentioned in previous sections, the observed large separation between observed baryonic matter and the gravitational potential responsible for the observed effect represents a direct evidence of the existence of dark matter, independent of the gravitational model. Mapping the mass distribution of the cluster partially corresponds to mapping the dark matter distribution. The lenses signal implies the existence of these invisible concentrations of mass, more massive than the surrounding gas, and spatially shifted (Clowe et al., 2006).

3.4.3 Amplifying far away objects

Strong lensing acts as a cosmic magnifying glass or natural telescope. It amplifies the luminosity of sources located far away. A large number of these objects would otherwise be unobservable such as primordial galaxies and first stars. A good example of this is the Frontier Fields program that used HST and Spitzer to observe the deep Universe. Its main objective was to observe high redshift galaxies, hopefully during the reionisation period. It combines six gravitational lens systems and its observations allow to observe sources with a magnitude superior to 29, improving the statistics of high redshift galaxies. The collected data can, for example, improve constraints on the luminosity function of high redshift galaxies (Lotz et al., 2017; Robertson et al., 2015) .

3.4.4 Measure of Hubble's constant H_0

The lens systems with multiple images of a variables source, such as a quasar, allow to measure the time delay between these different images. These delays depend on the geometry of the Universe and can lead to the deduction of the Hubble constant. A main example is the *H0LiCOW* collaboration, a program that aims to measure the Hubble constant without relying on classical methods such as scaling relations. This field of study, called time delay cosmography, is based on the fact that the arrival time of light from different images is delayed due to a combination of an increase in the path length and the gravitational time delay induced by the lens's potential. The time delay for an image is given by:

$$t(\theta, \beta) = \frac{D_{\Delta t}}{c}\phi(\theta, \beta)$$

Where $\phi(\theta, \beta)$ is the Fermat potential, expressed as:

$$\phi(\theta, \beta) = \frac{(\theta - \beta)^2}{2} - \psi(\theta)$$

In this case, θ characterizes the position of the observed image, β the real position of the source and $\psi(\theta)$ the deflection potential which assures that the mass distribution of the system is taken into account.

The key term here is the time-delay distance $D_{\Delta t}$, a combination of the different cosmological distances, expressed as:

$$D_{\Delta t} = (1 + z_d)\frac{D_d D_s}{D_{ds}}$$

Where D_s is the distance to the source, D_d is the distance to the deflector (lens) and D_{ds} the distance between the source and the deflector. The time-delay distance is proportional to H_0^{-1}. Measuring the time delays and modeling the lens amounts to estimate H_0.
The main problem of this method lies in the mass-sheet degeneracy (MSD) where different mass distributions can reproduce the observation but give different values of H_0. This degeneracy comes either from the model of the lens or the mass located along the line of sight, and demands additional constraint to produce realistic results for the estimation of the constant. This method thus proves itself to be powerful but highly dependent on the previous modeling of the cluster mass distribution (Refsdal, 1964; Schneider and Sluse, 2013; Suyu et al., 2017; Wong et al., 2024).

4 Background and related work

The first identification of gravitational lens systems among large surveys is a key step in most strong lensing analysis work. Indeed, as explained in the previous section, before thinking about modeling, multiple image sets are needed. For this matching of multiple images into sets to be possible, an image of a cluster classified as gravitational lens system is required. The following subsections present the detection of gravitational lenses, the matching of multiple images in strong lensing clusters, the automation of such a matching, and the limitations of these techniques.

4.1 Detection of the lens systems

Different methods for the detection of the lens systems are relevant and used nowadays, each with different levels of human intervention and/or automation. A first step into this overview would be to mention that many pipelines include a human visual verification step at their end. Detection methods based solely on human visual inspection have also been developed. Although time-consuming and tedious, they have already yielded good results, with consistent outputs between different observers and a good detection ability. Special attention must be paid to the algorithm used to display the images (Metcalf et al., 2019).

A different method consists in finding gravitational lenses by identifying gravitational arcs in survey images. These methods, labelled "Arc-Finders", distinguish arcs from morphologically similar sources, such as edge-on galaxies, through their shape, elongation, and curvature. Examples of algorithms implementing this technique are detailed below.
A first example was developed in Alard, 2006. The general idea is to associate with each point of the image a score that translates how much the local structure is elongated. To get this information, he started by identifying the main direction of the structure then, performed a transformation to that frame to evaluate the shape of the detected object. A global map showing the elongated zones is thus built. A selection criterion is then used to isolate highly elongated zones and regroup them in coherent objects. And finally, each object is characterized by shape and elongation so that potential arcs can be filtered. A final visual verification is then performed on a reduced number of candidates.
A second example of algorithm is explained in Seidel and Bartelmann, 2007. Unlike the precedent algorithm, it is mainly based on the local analysis of discrete elements that are then merged into larger structures (bottom-up technique), rather than a global map of the image. The image is here divided into small zones which are displaced and analysed independently, putting a strong focus on the coherence between zones. It constructs the different objects explicitly through repeated clustering and graph representation of the characteristics of the zones. It focuses on the coherence of geometric structures rather than on direct detection in the transformed image after filtering.

Machine learning is also present as a detection technique. The general method consists in transforming each image in a set of numerical characteristics. These characteristics describe the shape, outline or even texture of the image and its content. Supervised learning models are then trained on an ensemble of these features to learn the distinction between lens systems and the rest. The relevance of a model strongly depends on the ensemble of features chosen.
Among these techniques, the use of support vector machine (SVM) can be found (Hartley et al., 2017). In this algorithm, the image is first transformed to better outline the arc-type structures. The classical extraction of features can then be performed through oriented "Gabor" filters which highlight the tangential structures of gravitational lensing. The results of the filter response can thus be synthesized in a vector that will be used to classify them through the training of a non-linear SVM. The core idea is thus to detect specific geometrical patterns and then learn a complex frontier to classify them.
Simpler models such as LR (Logistic Regression) can also be used (Avestruz et al., 2019). This algorithm uses, for example, a different feature extraction based on HOG (Histogram of Oriented Gradients). It consists in analysing in which direction the light changes the fastest. In the end, the gathered features encompass the distribution of the outlines distribution and are synthesized in a vector on which the LR algorithm is trained.
Regardless of the machine learning algorithm used for classification, the core of the pipeline will be the extraction of features to summarize an image and their storage as so-called features vector.

Deep learning methods can be used for lens system detection. The particular use of CNN (Convolutional Neural Networks) is well adapted to this task as they are particularly suited for natural image analysis (Lecun et al., 1998). Their architecture is based on the extraction of image features through the application of small filters called kernels. They are learned directly during training and detect a pattern, texture or shape. They ultimately produce feature maps. Just as regular neural networks, non-linear transformations are then applied to model complex structures followed by pooling layers. In contrast to traditional machine learning techniques, the beforehand definition of the filter is not needed as they are automatically tuned during the learning phase of the algorithm. These models are trained on datasets of images (or data cubes when multiple bands are available), where lensing systems are labelled accordingly. The CNN then learns to distinguish between images containing gravitational lenses and those that do not (Metcalf et al., 2019).

4.2 Identification of multiple images sets

Historically, the matching of multiple image sets in strong lensing systems relied on human visual inspection. This matching was based on deformation and color, and validated by an expert. However, this approach is prone to confirmation bias and observer fatigue. Signature properties of such systems were also searched for, such as their geometrical configuration and parity.

Nowadays, methods have evolved and rely mainly on lens modeling. A mass distribution is first assumed, and a model is then fitted to the selected image candidates, predicting the positions of their multiple images in a physically consistent way (Broadhurst et al., 2005). The matching is therefore not performed directly, but inferred from the model. A candidate image is selected and a backward mapping is performed, projecting it into the source plane. The second step in this method is to perform the exact opposite, a forward modeling. The reconstructed source is re-lensed and the positions of the multiple image set is predicted. Finally, the observed and predicted positions are compared and the model is optimized to find a general coherence. In this framework, the matching process is directly integrated into the model optimization. In other terms, a matching is not performed, but the validation of the model implies it. One of these optimisation tool can be the MCMC based algorithm *Lenstool* (Jullo et al., 2007) detailed in the previous section (see Section 3.4.1). Another, lighter but less flexible, method consists of assuming that mass follows light. It can thus be used as a proxy to create an approximate model based solely on the light distribution. This can be illustrated by a superposition of each cluster galaxies modeled by a power-law mass density profile weighted by its luminosity (Zitrin et al., 2015). These LTM (Light-Traces-Mass) algorithms give less precise results than *Lenstool* as they are empirical and less flexible, but can be used for fast initial modeling.
Another example is the *YattaLens* algorithm (Sonnenfeld et al., 2018). It combines different aspects of the field by processing the image, applying color criteria and modeling. It starts by modeling and then subtracting the light of the deflector so that faint surrounding structures can be observed. The algorithm then detects, using the *SExtractor* software (Bertin and Arnouts, 1996), elongated sources close to the center that are suspected to be arcs. When a candidate is detected, its environment is analyzed by modeling its neighbors and computing the colors to identify sources from parasitic objects. The coherent structures are then regrouped in systems of multiple images based on their color. For each system, a parametric lens mass model is fitted to the data. The candidate is selected only if this gravitational lensing configuration explains the observed image positions and fluxes better than the hypothesis of unlensed, independent background sources. It is a complete method that detects the strong lens systems then uses potential multiple images sets to model the lens and validate the detection. However, it is based on a preliminary morphological detection (e.g. arcs). The color-based criterion acts as a secondary filter, reached only when elongated structures have been detected.

4.2.1 Early automated approaches

Nowadays, the different methods aforementioned have been compiled in pipelines such as MIFAL (Carrasco et al., 2020). It represents a proof of concept assembling the different algorithms developed in this section. It requires three essential components:

1. A catalog of arc candidates. It can be the output of an Arc-Finder type algorithm.
2. A photometric catalog. Each candidate has to be linked to a photometric redshift and a Spectral Energy Distribution (SED) or color obtained from a number of bands.
3. An initial mass distribution model of the lens. It is based on the LTM (Light-Traces-Mass) model which assures a good first approximation and is constructed before the matching of multiple images.

Once these prerequisites are met, the arc candidate catalog is used to fine tune the initial lens model. Different distance of lenses are explored by testing a range of source redshifts and repeating the computation for multiple configurations. Each candidate is then projected onto the source plane then reprojected onto the image plane to predict the positions of the set of multiple images. The search for real set candidates is then started by selecting objects close to the predicted image positions, with similar redshifts and similar surface brightness. A preliminary list can thus be constructed by regrouping the images into potential systems, combining duplicates and computing an average redshift per set. The different systems can then be refined. They are reorganised by combining similar systems and updating their general properties. An evaluation based on a score is then performed. The score used takes the shape of a χ^2 combination based on the redshift, position, color, and surface brightness.

$$\chi^2_{image} = \chi^2_r + \chi^2_z + \chi^2_{color} + \chi^2_{SB}$$

The final selection is performed by keeping the images with a good score, discarding the others and limiting the number of images per set. A global score per set is then computed. The produced catalog contains the final set of multiple images for the system. They can also be used to refine the mass model. The algorithm can then be relaunched to verify, optimize, or correct the results. The possibility to use typical lens configuration or image parity to improve the final result can also be exploited.

4.3 Limitations

Based on the preceding overview of these different methodologies, the limitations currently influencing the strong gravitational lensing field can be divided into two categories: intrinsic conceptual limitations, which are characterized by physics and geometry, and operational technical limitations, which depend on data quality and computational power. While the latter can be mitigated through technological advancements, the former represents permanent degenerate boundaries in lens modeling.
Among the intrinsic conceptual limitations, the most important one is the heavy dependency on an initial lens mass distribution. Indeed, multiple algorithm techniques in the lens system detection or multiple images matching base themselves on a preliminary mass model. Even though simple models like LTM can easily be obtained, they still represent a layer of approximation introduced directly into the pipeline. Furthermore, this approach relies on evaluating internal self-consistency: the multiple images are used to constrain a mass profile, which in turn assigns a statistical likelihood score to validate those same images. This optimization loop carries a risk of confirmation bias as a sufficiently flexible model might self-consistently fit an incorrect or accidental distribution of background sources.
Regarding the operational technical limitations, one of the main problems comes from the inherent complexity and uncertainty in astronomical photometry. Color-validation methods rely heavily on high-precision photometry. The necessary precision may not always be reached as it is degraded by observational noise, calibration problems and deblending errors. This technical limitation couples with an intrinsic conceptual limitation: different galaxies can naturally share an identical SED (Spectral Energy Distribution). This creates a degeneracy in color-space (see section 7.2.6 and 7.2.7 for examples in the results). While these contaminations could potentially be filtered using a geometric criterion, implementing a spatial constraint introduces the need for a prior knowledge regarding the lensing configuration. Just like preliminary mass model, this geometric filter introduces an operational bias that could lead to both false positives and accidental rejection of true atypical lens systems.
A final operational technical limitation in the image-matching process is the combinatorial complexity. Indeed, when a system with N candidates is evaluated, it involves $\frac{N^2-N}{2}$ potential pairs. This scaling significantly increases the computational need of this step, especially when it is combined with already demanding algorithms used in other stages of the analysis.

5 Objective and contribution of the work

Strong lensing effects in galaxy cluster fields appear as the manifestation of multiple images of a background source. Detecting these multiple images is a key step toward multiple applications in modern extragalactic astrophysics and cosmology. As outlined in the previous sections, these applications can range from the inference of cosmological constant through the monitoring of multiply-images quasar (Wong et al., 2024) to cluster mass-modeling (Smith et al., 2025). Many of these applications linked to mass modeling rely on the input of multiple images systems as an initial constrain. However, their matching in distinct sets is a difficult endeavor. Few automated methods currently exists, and most algorithms are subject to either human bias or an iterative process, based on an initial set of images, which can be prone to confirmation bias.

The objective of this work is to investigate the use of photometric comparison of sources as a preliminary criterion for matching multiple images set in strong lensing systems. The expected result takes the form of a semi-automated pipeline that produces pairwise comparisons of sources based solely on their flux estimated in different bands. This pipeline is intended to be light and transparent, requiring only the strict minimum amount of information aside from the initial images and allowing the full tracking of the results through the pipeline. It relies on the achromatic property of strong lensing by making use of the photometric properties of galaxies detected in multi-band images, their SEDs.

This pipeline represents an investigation, a proof of concept, based on a straightforward idea: "If two galaxies have very similar SEDs, they could be multiple images of the same background source". While relying on a simple assumption, it allows the construction of a structured and exploitable output. The pipeline presented in this work takes as input a set of multi-band FITS (Flexible Image Transport System) images from strong lensing system. Using an original metric based on the SEDs of these sources, the pipeline then creates a catalog that registers their mutual similarity. The pipeline is designed through different independently developed segments/blocs and tuned to fit one into the other. Its structure can be briefly summarized as follows:

1. **Image processing**
   Loads the images, realigns them if necessary and creates a “white-light image”.

2. **Detection of sources**
   Identifies the pixels above a certain threshold count value arbitrarily taken for source detection, deblends, and creates a segmentation map.

3. **Creation of the photometric catalog**
   Uses a segmentation map to create a photometric catalog containing information about the different detected sources (position, flux, associated errors).

4. **Galaxy differentiation**
   Separates cluster and field galaxies, defines of a zone of influence around the lens elements, segments the reference catalog into environmental subsets.

5. **Computation of similarity**
   Applies a SED-matching and mutual nearest neighbor (MNN) based metric to create a dictionary ranking sources by pairwise similarity.

There are multiple motivations behind this project. It represents a new and computationally efficient way of comparing galaxies as it relies directly on direct photometric comparison. While color criteria are typically relegated to a secondary validation role in traditional strong lensing pipelines, this work places them as the primary filtering mechanism. It does not rely on any prior mass model or external input such as pre-existing candidate catalogs. Working directly on the raw images, the pipeline performs the entire photometric analysis and candidate selection internally. Consequently, this statistics-based approach serves as a valuable first exploration tool at the start of an analysis phase, which can be easily integrated into more complex pipelines.
This method generates a dictionary in which every detected galaxy is associated to a catalog ranking the other sources by pairwise similarity. The final results of this method are thus more interpretable as their origin is clearly traceable along the pipeline and does not originate from a black-box algorithm. This method aims to be flexible and extensible as it could integrate high-fidelity cluster finder based on probabilistic classification (e.g. *redMaPPer*: Rykoff et al., 2014).

In the following sections, the specific processing steps will be detailed and illustrated by their application on real cluster data.

6 Description of the pipeline

This section is dedicated to the description of the pipeline. It has been developed based on a specific cluster, SPT–CL J0356-5337, and further tests are needed to assess how it holds on when applied to other clusters. Its elaboration has been made using widely used python libraries: `pandas` (Harris et al., 2020), `photutils` (Bradley et al., 2026), `astropy` (Astropy Collaboration et al., 2022), `matplotlib` (Hunter, 2007) and `scipy` (Virtanen et al., 2020) among others. The code created for this work can be asked directly to the author or can be found on GitHub[2].

Before starting the description of the pipeline, a preliminary overview of the reference system SPT–CL J0356-5337 is needed. The galaxy cluster SPT–CL J0356-5337 (Figure 3) is a great example of a merging cluster (Mahler et al., 2020; Smith et al., 2025). It is composed of two main structures located at the same redshift ($z \sim 1.03$) and separated by ~ 170 kpc. On the left, a component linked to the brightest cluster galaxy (BCG). On the right, a component linked to a group of luminous red cluster member galaxies (LRGs). Those two structures also have equal radial velocities (gap $< 300km^{-1}$). This implies that they might be merging in the plane of the sky, as their radial velocities difference is relatively low and they are located around the same redshift. The mass distribution of these two substructures corresponds to two distinct halos of comparable masses, with a ratio around 1 : 1.2 to 1 : 1.6. These mass ratios hint toward a possible major merger.

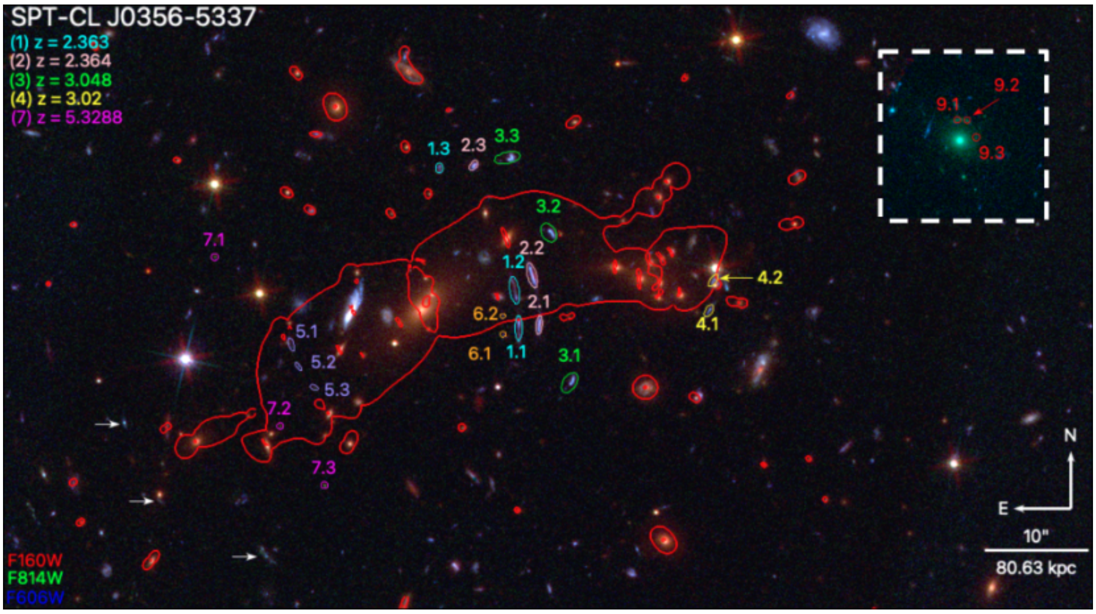

Figure 3: HST image of SPT–CL J0356-5337 (Smith et al., 2025). The multiple images candidate systems have been color-coded. The red outline represents the critical curve at $z = 3$

.

[2] https://github.com/VaitOnline/Master-Thesis.git

For this cluster, eight main candidate systems have been identified and outlined in Figure 3. Among the identified systems, five were selected as primary constraints for the mass distribution modeling: 1, 2, 3, 4, and 7. These systems serve as the main benchmark for the pipeline presented in this work. Its performance is evaluated based on its accuracy in reconstructing and matching the multiple images of each system to their respective common sources.

The selection of SPT–CL J0356-5337 as a primary test for the development of this pipeline is motivated by different factors. It provides an optimal balance in source density. This means that it is sufficiently populated with confirmed multiple images systems to serve as a robust benchmark, yet it is clear enough to allow the manual evaluation of false positives and problems. The availability of high-resolution images, essential in this pipeline, also played a role in this selection.

6.1 BLOC 1: *Image processing*

The first step in this pipeline is the importation of the data which consists of multi-band images of the lens galaxy cluster. For this work, we used images taken by the Hubble Space Telescope (HST). This space telescope was initially launched in 1990 into low earth orbit and remains in operation to this day. It was funded and built by the National Aeronautics and Space Administration (NASA) with contribution from the European Space Agency (ESA). This telescope provides detailed data in the UV, visible and infrared. Among the instruments active on board, this work specifically utilizes data from the Advanced Camera for Surveys (ACS) for the optical bands and the Wide Field Camera 3 (WFC3) for the near-infrared channel.

While the pipeline can ingest as many different band images as needed, for our initial case study (here SPT–CL0356-5337) we used the following: F606W and F814W (mounted on ACS), alongside F110W and F160W (mounted on WFC3/IR). This choice of filters allows for the gathering of information on a wide section of the visible spectrum and part of the IR. This choice also enables the reconstruction of the SED of the sources which will be a crucial part of this work. It is worth mentioning that, as these images originate from different instruments, they possess distinct pixel resolutions: typically $\sim 0.05\,\mathrm{arcsec/pixel}$ for ACS (Avila, 2016) and $\sim 0.13\,\mathrm{arcsec/pixel}$ for WFC3/IR (Sahu, 2021). For this reason, verifying the spatial alignment is a mandatory preprocessing step before the analysis.

These images are provided in the form of FITS, a standard format widely used in astronomy to store scientific data. They are composed of different blocs called HDUs (Header Data Units):

- **Header**
  It is the descriptive part of the file. It contains keywords that indicate the type of data, the dimensions (number of pixels, number of planes), the physical units, date of observation, instrument used, and exposure time among others.

- **Data**
  It is the matrix of values that corresponds to the image pixels. It can contain NaN, noise, physical values, etc. These are the numerical values that will be analyzed later on via different methods such as the detection of sources and photometry.

- **WCS (World Coordinate System)**
  It is a specific component of the header that contains a description of the coordinate system. It allows the link between the pixels of the image and celestial coordinates (RA, DEC). It is accessible in the header via specific keywords. It contains the position of the reference pixel (the central pixel in the data matrix most of the time), the coordinates of that reference in celestial coordinates, and the matrix of transformation among others.

Upon loading, the images are split respectively between their header and data. The data will lie at the center of the analysis while the header will be used for the transformation of the data (units, position, exposure time). The display of the different images can be done using simple functions to visualize what will be worked with.

In this work, the two images of SPT–CL J0356-5337 centered in the visible (F606W and F814W), do not have the same shape as the two in the near infrared (F110W and F160W) as shown in Figure 4. This is due to the fact that, as mentioned before, they have not been obtained with the same instrument aboard the HST. The images in the visible have been obtained using the Advanced Camera for Surveys (ACS) while the images in the near IR have been obtained using Wide Field Camera 3 (WFC3). It is also worth noting that the images have been displayed by cutting at the 5th and 99.5th percentile, just for a better display. This simplification coupled to the fact that the images are already in counts per second (number of photons hitting a pixels detector per second) explains the small values on the colorbars.

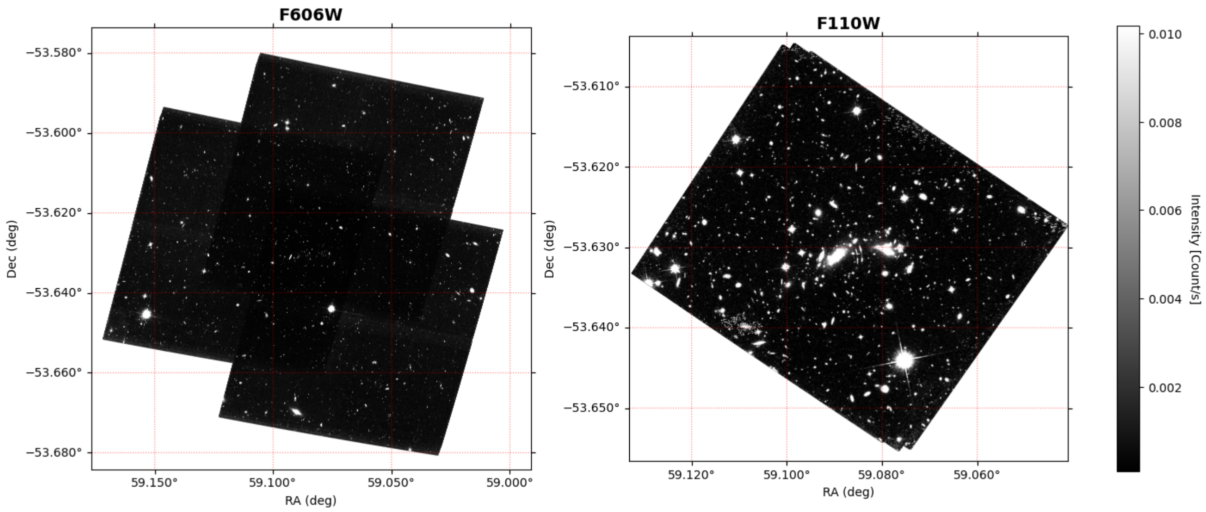

Figure 4: Comparison of the FoV of an image taken with ACS (left) and with WFC3 (right). The image in the F110W band, if reprojected, would be located at the hyper-center of the image in the F606W band

To identify the sources present in the data, we constructed a white-light image. A white-light image is a synthetic broadband frame obtained by co-adding individual images acquired across multiple bands. This pixel-wise summation produces a single frame containing the integrated flux over an extended wavelength baseline, which maximises the cumulative signal-to-noise ratio and improves the detectability of faint sources. In the context of this work, this approach additionally ensures that the full spatial morphology of each source is captured at the detection stage, rather than being restricted to its emission within a single band. This consideration is particularly relevant for extended features such as gravitational arcs.

The co-addition procedure imposes an important requirement on astrometric alignment: each pixel must map onto an identical sky coordinate across all filter frames. Any residual misalignment would introduce spatial blurring in the white-light image and compromise following analysis such as photometry, in which flux dispersed over an artificially broadened profile would produce systematic errors (Figure 5). The astrometric consistency of the input frames was therefore verified by comparing the world coordinates of the reference pixel across all images, using the WCS keywords encoded in the FITS headers via the `astropy WCS` class (Table 1).
This verification revealed a residual misalignment, which, if uncorrected, would propagate directly into the co-added image as a spatial blur.

	Right Ascension [deg]	**Declination [deg]**
F606W	59.08399282	−53.62887798
F814W	59.08399282	−53.62887798
F110W	59.08702463	−53.63010735
F160W	59.08701825	−53.63010111

Table 1: WCS Coordinates of the reference pixel for each images used in this work.

To align those images, we start by defining a reference image. In this work, we arbitrarily chose the F814W image. Because its dimensions are larger than the images in the near IR due to the field of view of the instrument, this method did not require padding on the image before the alignment. Once the reference image has been defined, its header is saved as it contains the information on the system in celestial coordinates. This image will thus define the final "spatial grid" so that each image ends up with the same number of pixels, dimensions, and reference pixel value.

Each image is processed as follows. The corresponding FITS file is loaded, and both the pixel data and the WCS are extracted. The WCS is then used to reproject the image onto the reference coordinate system. This process consists of computing, for each pixel of the original frame, its corresponding position in the reference grid, accounting for astrometric scale and any additional geometrical transformations. Since the reprojected pixel positions do not in general correspond to the native pixel grid of the reference frame, a simple shift is not enough to achieve a precise alignment. The flux value at each new grid position is thus estimated via bilinear interpolation, which reconstructs the signal at a sub-pixel location as a weighted average of the four nearest neighbors in the original image. This average is weighted inversely proportional to the distance from the interpolated position. The reprojected image thus shares the pixel grid and astrometric solution of the reference frame with consistent spatial coherence across all filters before their co-addition. The header of the image is updated to correspond to the coordinate system of the reference image. The new image is then saved as a new FITS file with the corresponding header.

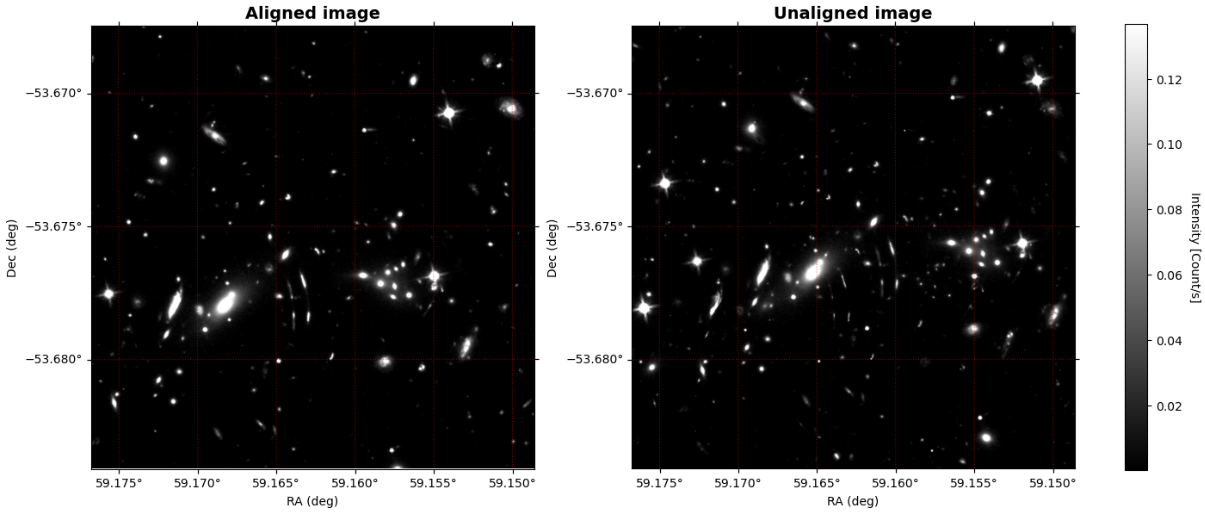

Figure 5: Comparison between the white light image created with and without preliminary alignment of the HST images in the different bands. The observable misalignment in right ascension and declination is respectively of 0.00179786° and −0.00122937°. This converts to a total distance of ~ 7.84 arcsec.

As a precision, it is worth noting that a padding was added when needed if the dimension of the image to align was shorter than the reference one. This padding comes in the form of layers of pixel with NaN values. It enables all the images to have the same dimensions.

This process of alignment still has some limitations. It relies on the hypothesis that the WCS in the FITS files header are very well calibrated. If the initial images have very different resolutions, a compromise has to be found on the final grid and the precision of the alignment will suffer from it. This is not the case here.

Once the images have been properly processed and aligned, their data matrices can be stacked and summed in order to create the white light image. This can be seen as a superposition of multiple matrices, adding the value of the same respective pixel in each matrix. The final product of this bloc of the pipeline is thus a white light image created with the aligned original images. Acting as the primary detection image, this high-signal-to-noise reference encompasses the total flux across multiple part of the spectrum to optimize source extraction.

6.2 BLOC 2: *Detection of the sources*

Now that the images have been properly aligned and that a white light image has been created, the different sources present in the image can be detected. For this project, we implement an image segmentation approach. This technique identifies discrete sources by grouping contiguous pixels that exceed a specified significance threshold above the local background noise. The objective is to detect and isolate the different astrophysical objects for further analysis. The core mechanic relies on generating a segmentation map that assigns a unique integer ID to each detected source, while background pixels are assigned a value of zero. This map serves as the foundation for the creation of a photometric catalog, enabling localized, non-redundant measurements of individual objects. To optimize this process and mitigate the risks of over- or under-segmentation, fine-tuning of the detection criteria (such as the convolution kernel, minimum pixel area, and deblending thresholds) is required. It is also worth noting that while image segmentation isolates the spatial footprint of a source, it does not analytically model its luminous profile, contrarily to profile-fitting methods (e.g. PSF-fitting or aperture photometry).

The segmentation map is constructed from the white-light image, produced in the preceding step (6.1). This choice offers multiple advantages. Firstly, the enhanced signal-to-noise ratio resulting from the multi-filter combination facilitates the detection of faint objects, particularly in noisy regions of the image. Secondly, the white-light image provides a synthetic broadband representation of the field, capturing both red sources, which are primarily visible in the infrared, and blue sources, which are dominant in the optical, ensuring spectral completeness at the detection stage. This spectral and spatial consistency means that the field needs to be segmented only once, after which photometric extraction can be performed in each filter independently, without repeating the detection step per band. A further benefit is the suppression of false positives like noise artefacts confined to a single filter that are naturally diluted in the co-added image. However, this approach is not universally optimal, as broadband co-addition can dilute spectrally localised features, potentially missing sources with significant flux only in a narrow wavelength range. The developed function to construct the segmentation map is fully based on functions from the `photutils` python library (Bradley et al., 2026).

The first step in this detection method is to account for NaN values. These are found in the zones outside the field of view of the instrument as well as in the added padding. A mask corresponding to the position of the NaNs in the value matrix of the white light image is created to keep their position in memory if needed. These values are then replaced with the median of the image so they do not bias the statistical measurements or influence the detections.

The second step is the estimation of the background and noise. The objective is to compute the average background as well as the RMS (Root Mean Square) noise of the image. With this in mind, we start by dividing the image into small squares (*Tilling*). The size of those squares has been arbitrarily set to 50 pixels for this project. Indeed, we want this background to take the shape of a local map. A background estimation method based on SExtractor is then applied (Bertin and Arnouts, 1996). It uses sigma clipping on a histogram made of the pixels in each square to exclude outliers from the computation of the background. These outliers appear in the form of hot pixels or bright objects, which should not be considered for this computation. This assures that only coherent values are kept for the background estimation. For a given sample/box, we compute the median and standard deviation and then exclude every values outside of the interval:

$$\text{median} - 3\sigma \leq x \leq \text{median} + 3\sigma$$

This formula is particularly robust when there is an asymmetric component, in this case the bright sources that are in minority. This exclusion method is applied successively until no more significant changes appear from one application to the next one.
The output of this method is two maps. The first map contains the value of the background in each cell taken as the remaining mode after sigma clipping. It is computed as:

$$\text{Mode} = (2.5 \times \text{Median}) - (-1.5 \times \text{Mean})$$

The second is a map containing the RMS, standard deviation after sigma clipping. These two maps represent respectively the background levels and the statistical noise. The background is then subtracted from the original image which has for objective to isolate the significant astrophysical signal.

The third step is the estimation of the detection threshold. Pixels above this threshold will be defined as significant and potentially part of a source. It is defined as following:

$$\text{Threshold} = \text{Coefficient} \times \text{RMS}$$

The coefficient was arbitrarily fixed to 3 to guarantee detections far above the statistical noise, effectively filtering it. As the RMS is really a map of the local standard deviation, the detection threshold will also be a map and the threshold will vary in each box of the image previously defined.

For this project, we can see that a small part of the light from the BCG has been taken into account (Figure 6). This is mostly due to the size of the BCG being larger than the tilling square. However, it has been kept this way as satisfactory results were obtained despite that. The error introduced in the magnitude of the BCG does not bear much importance for this pipeline as cluster members will be automatically detected and excluded later on. Furthermore, a small part of the diffuse light originating from the

BCG, which has been taken as background, could have been subtracted from neighboring sources, effectively removing part of the contamination. Although this last point remains an assumption, this version produced better results than one with larger tilling and has thus been kept.

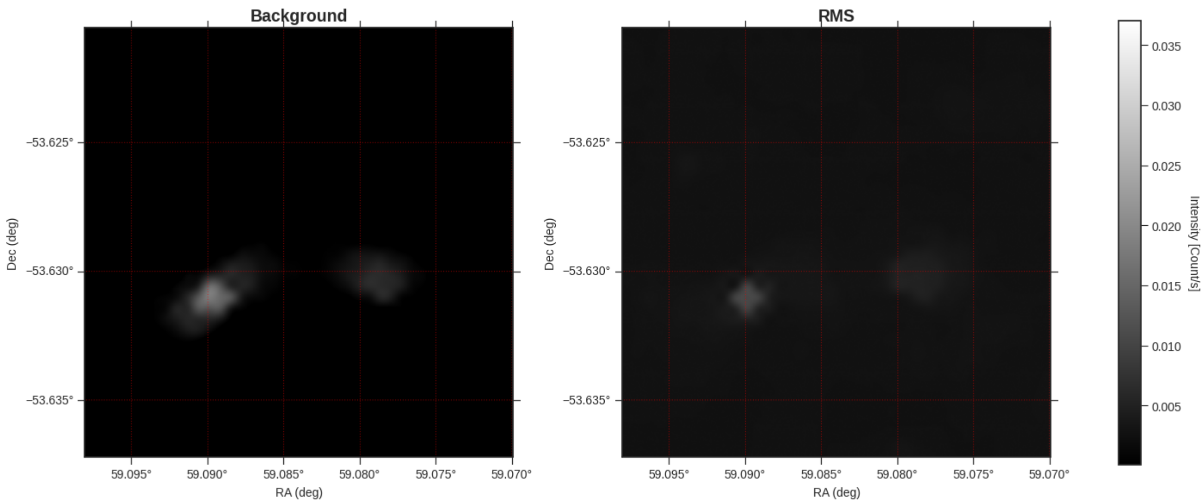

Figure 6: Representation of the background and RMS noise of the white light detection image around the center of the merging cluster. The mostly-close to 0 values were expected in this case as the images were already pre-processed before acquisition and the background should thus have already been mostly subtracted.

The fourth step is the convolution of the original image, which is crucial to improve the detection of sources. It consists of smoothing the image so that the significant structures are enhanced and random noise is diminished. Indeed, it improves the spatial connectivity of significant pixels during the detection stage. To smooth the image, we progressively apply a gaussian kernel to the image (Figure 7). Each pixel thus take the value of a weighted average by a gaussian kernel of his neighbors. The gaussian shape of the kernel is adequate as it models precisely enough the typical shape of the center of a galaxy. It is worth specifying that, even though galaxies are elongated astronomical objects, their central part can be roughly approximated to a bell shaped luminous profile. The gaussian shape does not favor any direction, contrarily to asymmetric kernels. This type of kernel adapts well to any type of source (round, elliptical, irregular) as long as they are spatially coherent, which means no gap in their profile. This method can thus be seen as a low-pass filter that eliminates the noise and preserve the continuity of light in the galaxy.

For this project, we initialised a gaussian kernel with a standard deviation of 3 and a kernel size of 9. This is a common compromise. Although a gaussian is theoretically infinite, its value becomes negligible after 3σ. This means that we truncate the gaussian after 4.5 pixels, which is enough to encapsulate a gaussian until 3σ on each side of the center.

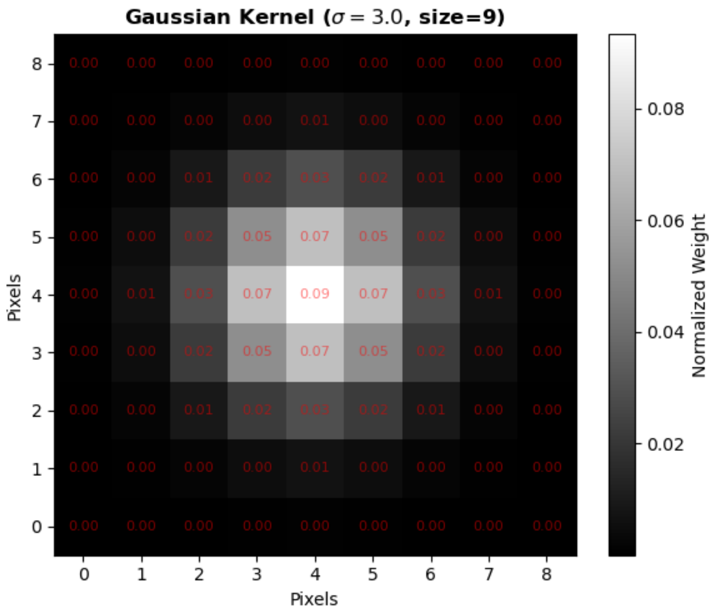

Figure 7: Gaussian kernel of 9x9 pixels used to smooth the image before detection.

The fifth step in this bloc is the actual detection of the sources. This comes in two phases: thresholding and labelling. We start by going over each pixel of the convolved image, which has been previously background subtracted. When a pixel has a value above the local threshold, it is considered as potentially part of a source. As explained before, the threshold is, in this case, a 2D map where each pixel has a value of n times the local statistical noise. This step generates a binary image: 1 for a pixel above the threshold, and 0 otherwise. A "connect-component labeling" approach is then used to identify clusters of connected pixels that have a value of 1 in the image. Each connected region becomes a connected source and sees itself attributed a unique integer label. Those connections are made by 8-connectivity, which means that the function looks at the neighboring pixels in each direction, including diagonals. The detection of a group of pixels being considered as an object can be controlled by fixing the minimal number of pixels that a group has to contain. Although it is normally fixed to five (one central pixel and four neighbors without the diagonal), it was here arbitrarily fixed to 80. This number may seem high but we are working with an image of dimension exceeding 10 000 pixels, and where the sources that need to be detected are galaxies and not very small point-like sources.
The final product is a segmentation map, a 2D image where each pixel contains 0 for the background (nothing was detected) or n ($n > 1$) for each detected sources.

The last step consists of deblending the previously detected sources using the segmentation map and background-subtracted white light image. Sources deblending is based on the Watershed principle, already used in SExtractor (Beucher, 1992). It is an algorithm widely used in image segmentation to separate regions that are connected but have multiple intensity peaks. In the `photutils` library, it is implemented as follows:

- The different intensity peaks are found in each individual segment of the image. The delimitation of the segment is done based on the provided segmentation map.
- It generates iteratively a deeper and deeper smoothed cut of the image. The number of cuts and the way they are separated can be fixed manually and have to be tuned.
- On each level, the algorithm assesses how the different "ponds" develop around the peaks.
- If two regions in a segment are separated by a dip deep enough, called contrast, they are considered as two separate sources.

This method is thus really sensible to the image, the contrast, and the number of levels considered. For this project, we only deblended the sources if the independent sources created from a given segment contained at least 100 pixels. The number of levels was here arbitrarily fixed to 16, dispersed linearly, with the contrast at 0.03. After deblending, each sub-source is given a new label and the final result is an updated segmentation map (Figure 8). The number of labels in the final segmentation map is thus higher than in the original one.

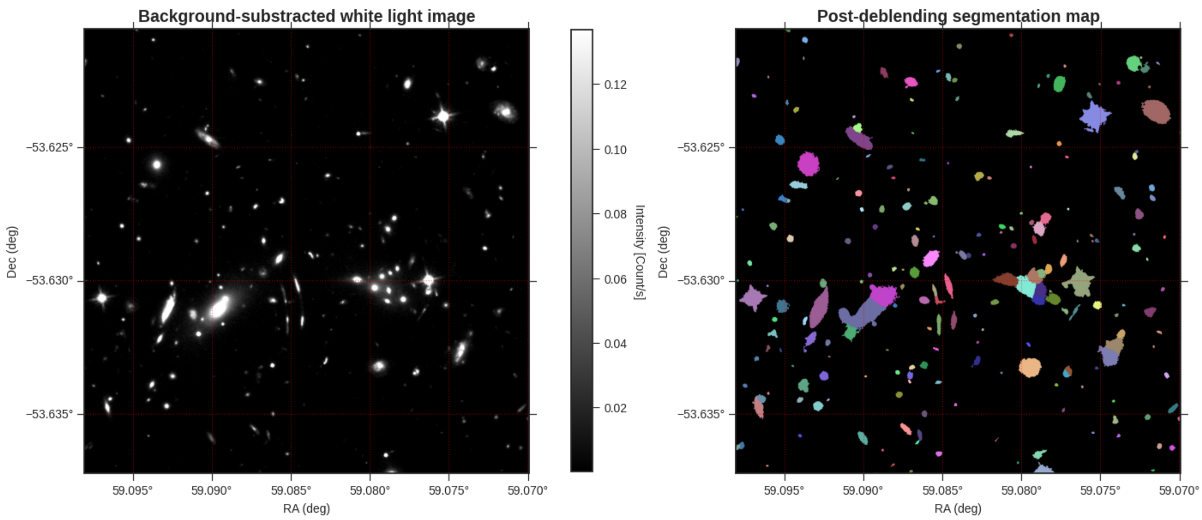

Figure 8: Segmentation map (right) created based on the background-subtracted white light image (left). Each different color corresponds to a different de-blended source.

The quality of the segmentation map was assessed based on its ability to accurately detect and deblend the different known multiple image sets. The inspection was performed manually.

Set ID	Detection	De-blending	Usability
Set 1	All sources detected	Source 1.2 was not correctly deblended	Partially ✓
Set 2	All sources detected	Successfully deblended	Yes ✓
Set 3	All sources detected	Successfully deblended but require some manual adjustment (fusion of labels)	Yes ✓
Set 4	All sources detected	Source 4.1 could not be resolved due to a bright neighboring source	No
Set 5	All sources detected	Fusion of source 5.1 with a neighbor	Partially ✓
Set 6	Missing 6.1	/	No
Set 7	All sources detected	Successfully deblended	Yes ✓
Set 9	Not detected (too faint and close to bright source)	/	No

Table 2: Multiple image set inspection. The sets are labelled as in Figure 3 (Smith et al., 2025). The usability of a set translate the completeness of its recovery and photometric accuracy.

To evaluate the performance of the segmentation bloc, we adopt a selection criterion based on Smith et al., 2025. In their reference study, only sets 1, 2, 3, 4, and 7 were used as constraints for the lens modeling. These specific sets thus constitute the benchmark for this pipeline's assessment. The resulting segmentation map successfully recovers, at least partially, all targeted sets with the exception of set 4. The final performance analysis of the pipeline is thus based around its efficiency in detecting matching these specific structures (Table 2).

6.3 BLOC 3: *Creation of the photometric catalog*

Now that the different sources have been detected in the white light image and saved as a segmentation map, their photometric properties can be extracted from the original image. This is done in a series of multiple steps, which will be detailed in this subsection.

The first step is to make use of the preliminary created white light image to extract the structural and positional information about the sources. For this purpose, the various computational steps made in section 6.2 to obtain the background, local noise and convolved image, will be done again. The extraction of information on the different sources is done successively by applying the segmentation map previously created as a boolean mask, which allows for the isolation of the different sources. The photometric analysis of the images was developed using the `photutils` Python package (Bradley et al., 2026). Specific core routines from this library were combined into a dedicated, self-contained pipeline made for this project. The architecture of this procedure and the integration of these routines are detailed below.

The analysis begins with the extraction of a list containing the unique integers that correspond to the segment ID. The list will be used later on as a "group by key" to concatenate the information extracted in the different bands.
The centroid position of each source is then computed. It is done by adjusting a quadratic polynomial on a box of 5×5 pixels centered on the brightest pixel of the source. The centroid thus corresponds to the maximum of this polynomial, which is found by evaluating the first derivatives. Mathematically, we have:

$$\begin{aligned}
f(x,y) &= a_0 + a_1 x + a_2 y + a_3 x^2 + a_4 y^2 + a_5 xy \\
\frac{\partial f}{\partial x} &= a_1 + 2a_3 x + a_5 y \\
\frac{\partial f}{\partial y} &= a_2 + 2a_4 y + a_5 x \\
\text{Centroid} &= \left(\frac{\partial f}{\partial x} = 0, \frac{\partial f}{\partial y} = 0 \right)
\end{aligned}$$

The obtained coordinates are then transformed from pixels to RA/Dec by making use of the World Coordinate System in the initial file. This extraction is made on the convolved image, as gaussian smoothing mitigates the isolated noisy pixels that would have artificially pulled the centroid position.
By making used of the newly defined centroid position, the covariance matrix of the flux distribution can be computed. It describes how the flux is spread around the centroid and is expressed as:

$$\Sigma = \begin{pmatrix} \mu_{xx} & \mu_{xy} \\ \mu_{xy} & \mu_{yy} \end{pmatrix}$$

Where the covariance is computed source-wise, just like the centroid, by

$$\mu_{xy} = \frac{\sum_{i\in\text{segment}}(x_i - x_c)(y_i - y_c)\cdot I_i}{\sum_{i\in\text{segment}} I_i}$$

in which I_i corresponds to the count, or flux, of each pixel belonging to a source. Diagonalising this covariance matrix allows us to find the principal axes of the source, characterized by its eigenvalues. The semi-major axis and semi-minor axis are thus expressed respectively by $a = \sqrt{\lambda_{max}}$ and $b = \sqrt{\lambda_{min}}$. The orientation with respect to the x axis can also be computed. It corresponds to the angle between this axis and the direction of the semi-major axis, expressed as $\theta = \arctan\left(\frac{v_y}{v_x}\right)$ where v_i are the components of the eigenvector associated with λ_{max}.

The second step in the extraction of our sources' information is to extract their fluxes in the different available bands. For this purpose, the different images are successively processed using the `Photutils` package in the same way than in section 6.2: computation and subtraction of the background, convolution, and masking of NaN pixels. The boolean mask provided by the segmentation map is then applied on the background subtracted image. The count, or flux, of each pixel belonging to a source is then summed to produce the total flux as:

$$F = \sum_{i\in S} I_i$$

The same process is followed for the flux associated error, based on the local RMS previously computed:

$$\Delta F = \sqrt{\sum_{i\in S} \sigma^2_{\text{tot},i}}$$

Once all those pieces of information extracted, they are concatenated in a table grouped by source ID. This table corresponds to the photometric catalog of SPT–CL J0356-5337 and will serve as basis for the following analysis.

The last step in the creation of the catalog consists in discarding sources that lack a photometric measurement in at least one of the considered bands. This situation naturally happens when the images are acquired with different instruments whose fields of view (FoV) do not necessarily match. Although all instruments target the same region and their FoV thus generally overlap at the center of the field, differences in coverage may result in sources located at the periphery of the field. They are thus being detected in some bands but not in others. Incomplete sources are therefore excluded from the final catalog to ensure that all retained sources have a full spectral coverage across the available bands. For this project, as explained in section 6.1, the images taken in the near infra-red (NIR) are much smaller than the others due to their difference in instrument origin. For this reason, keeping only the sources detected in those bands will assure a full spectral coverage, as it ensure detection in the other bands at the same time.

The final product of this bloc of the pipeline is thus a photometric catalog. This catalog contains information about the sources position, structure, emission and associated errors.

6.4 BLOC 4: *Galaxy differentiation*

A photometric catalog containing the positional, structural and photometric information of the different sources was obtained. At the moment, the catalog created for the elaboration of this pipeline counts 925 sources. This section will detail how this catalog will be cleaned, cut and transformed in order to compare, in the most effective way, the sources' approximated spectral energy distributions.

To ensure physical consistency, a flux-quality filter is applied to the initial catalog. This step accounts for the specificities of the multi-band photometry method, where source detection and segmentation boundaries are defined on the co-added white light image, while photometry is extracted within these fixed areas for each individual band. This consistent aperture approach ensures that flux measurements track identical spatial regions across wavelengths. However, for sources with negligible emission in a specific band, the direct summation of pixels within the white-light mask can be dominated by local noise, occasionally creating a non-physical negative integrated flux. To maintain a robust and reliable sample, these low-significance detections are excluded through this quality cut, resulting in a final clean catalog of 894 sources. Ideally, rather than a strict zero-flux cut, these sources should be treated by defining a physical lower bound consistent with the local noise level such as $0 - n\sigma$.

In order to have robust results, special attention has to be paid to the noise in the detection. Indeed, some sources present an insufficient signal-to-noise ratio in at least one of the bands. On one hand, it means that the flux measurements are dominated by noise. The shape of the SED is thus not efficiently constrained within that band. On the other hand, it will later affect the comparison of the SEDs.
For these reasons, the sources displaying a S/N ratio below a given threshold in at least one of their bands have been discarded from the catalog. For this project, it reduced the catalog size to 786 sources.
Another important step in the refinement of this catalog is to transform it. Indeed, the summed pixel counts taken as flux for each of the sources can come in different units depending on the pre-processing. While these units can sometimes be physical, they present themselves in analog to digital unit (ADU) per seconds for our SPT–CL J0356-5337 data set. It corresponds to the number of photons hitting the detector in a period of 1s. As it depends on the instrument used, it was transformed into AB magnitude as we want this unit to be generalized in order to compare it to the scientific literature. It is a system that takes as a reference point an imaginary source that emits a constant flux of 3.63×10^{-20} erg cm$^{-2}s^{-1}Hz^{-1}$. This conversion is possible by making use of the conversion factor *PHOTFLAM*, which says what amount of energy correspond to 1 electron/s, and the pivot wavelength of the filter *PHOTPLAM*, which is a propriety of the filter that characterizes the conversion flux density by unit of frequency and by unit of wavelength.

The apparent magnitude is thus given by m as:

$$\begin{aligned} Z_{AB} &= -2.5log_{10}(PHOTFLAM) - 5log_{10}(PHOTPLAM) - 2.408 \\ m &= -2.5log_{10}(F_{ADU/s}) + Z_{AB} \end{aligned}$$

The error associated to the magnitude can also be computed by using the rule for error propagation in a function of one variable:

$$\sigma_m = \left|\frac{dm}{dF}\right| \times \sigma_F$$

Z_{AB} is a constant and $log_{10}(F) = \frac{ln(F)}{ln(10)}$, which leads to:

$$\begin{aligned} \frac{dm}{dF} &= -\frac{2.5}{ln(10)} \cdot \frac{d}{dF} ln(F) \\ &= -\frac{2.5}{ln(10)} \cdot \frac{1}{F} \end{aligned}$$

The final error to the magnitude in the AB system is thus expressed as:

$$\sigma_m = \frac{2.5}{ln(10)} \cdot \frac{\sigma_F}{F}$$

6.4.1 Extraction of the cluster members

6.4.1.1 Linear regression

Once all of these preliminary corrections have been made to the photometric catalog, the biggest false positive origin in this analysis has to be adressed. When we look at a galaxy cluster, the sources in the FoV fall into 3 main categories:

- **Stars** from our own galaxy which lie in the foreground of the cluster.
- **Field galaxies** which are galaxies that lie in the same line of sight than the cluster but do not share the same redshift (foreground or background of the cluster).
- **Cluster galaxies** which constitute the primary luminous components of the cluster. They all share approximatively the same redshift $z_{cluster}$ and are thus gravitationally bound.

All of these different categories of element are projected onto the plane of the sky when creating an image. They can however be classified through their spectroscopic/photometric redshift by searching for specific absorption, emission or break in their spectra. Because of their common redshift, cluster members also share the same characteristics and thus the same color. This can be used to approximate their identification when their redshift is not known or available. For this analysis, close attention has been paid to cluster members, which require a short preliminary introduction.

As detailed in section 2.2.1, clusters are bathed in a hot and dense gas (ICM). This hostile medium directly acts on the gas content of the galaxies inside of it through different processes. One of these is ram pressure stripping (Gunn and Gott, 1972). The pressure in the ICM tears the cold gas of the galaxies, effectively deleting its star formation ability. Cut out from gas and without way to create new stars, the stellar population of the galaxies evolve passively. Hot and massive blue stars consume their fuel and die. Progressively, the galaxy is only left with cooler red stars that have a long life span. The galaxies die as their blue stars vanish without being replaced (Bruzual and Charlot, 2003). This homogeneity in the stellar populations is observable in the color-magnitude diagram via the red sequence, a linear relation on which the old cluster member galaxies regroup. The small dispersion around this relation is thus interpreted as a similar formation at high redshift (Bower et al., 1992). The slope of this linear relation is due to the mass-metallicity relation. The more massive galaxies are more able to retain their components due to their larger gravitational potential, effectively rendering their stellar population more metallic and thus redder (Gladders et al., 1998).

This section is dedicated to the extraction of cluster members from our photometric catalog as they would appear very similar after χ analysis, their SED being similar. As mentioned before, detecting cluster members corresponds to approximating the red sequence. With the motivation of creating a light pipeline, existing algorithms making use of the redshift will not be used here. However, it is worth reminding at this state that any bloc of this pipeline can be replaced by better performing existing algorithms, although more demanding. An alternative would be to use *redMaPPer* (Rykoff et al., 2014). This algorithm iteratively calibrates a red sequence model trained from a spectroscopic training sample. It then computes a membership probability for each galaxy in the field based on its magnitude and associated error in different bands.

The first step to identify the cluster members through a red sequence selection is to create the color-magnitude diagram (Figure 10). It takes the form of a scatter plot with the magnitude of the sources in a given band as x-axis and a color index created via subtraction of two different bands as y-axis. Although color-magnitude diagrams are usually created based on a red and a blue band for their color index, it is not the case for this work. Indeed, the color index is expressed as the subtraction of F110W and F160W. This choice purely relies on the ability to make a comparison with the scientific literature as it is a development pipeline, and therefore needed a reference on which to base itself. The reference diagram is the color-magnitude diagram from Smith et al., 2025 (Figure 9).

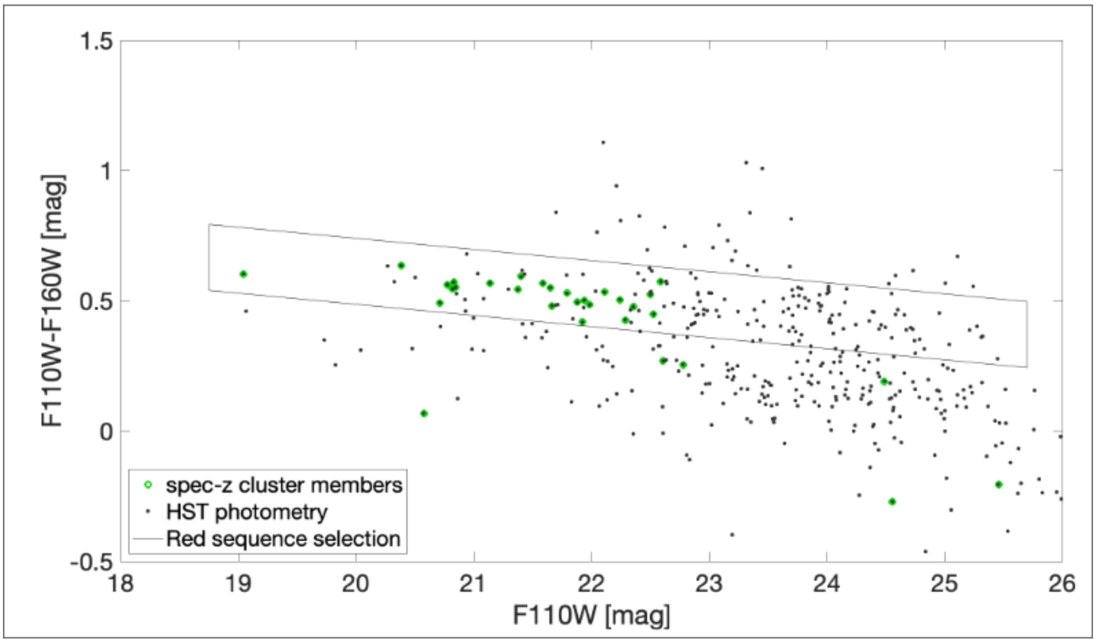

Figure 9: Color-magnitude diagram of SPT–CL J0356-5337 in the HST/WFC3 FoV from Smith et al., 2025. The sources highlighted in green marks the spectroscopically-selected cluster members. The solid line shows the cluster member selection based on a linear fit on the highlighted sources.

Just as in the reference diagram, an overdensity of sources can be seen starting around mag $\sim 21 - 22$ between color index $\sim 0.5 - 0.75$. This region contains a bulk of spectroscopically-confirmed cluster members on MUSE data. This overdensity then fades into a confusion zone around mag $\sim 24 - 25$ where the source density becomes more uniform. This confusion zone is only enlarged in the case of this work as the total amount of source in the photometric catalog is greater than the one from the reference by a factor 4. The main reason behind this is that our detection encompass the entirety of the HST/WFC3 field. Sources that lie on the edge of the FoV will be present in the catalog, even though they do not lie anywhere close to SPT–CL J0356-5337 BCG.

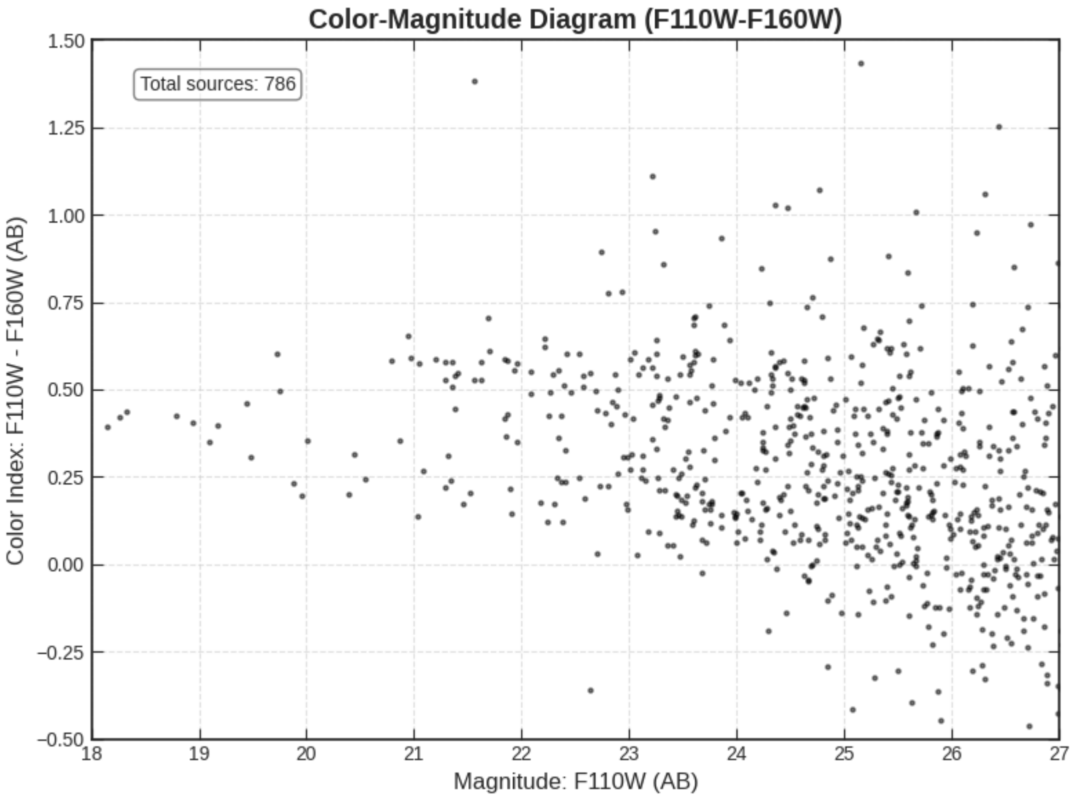

Figure 10: Color-magnitude diagram of SPT–CL J0356-5337 in the HST/WFC3 FoV created with this work's photometric catalog. The color index represents F110W-F160W.

The method used in this project to isolate the red sequence will be to perform a linear fit on a region of overdensity. A confidence interval will then be defined around this fit in order to accept or exclude sources located in its vicinity. The first step in this selection is to create a 2D-histogram. It is done with the use of the `numpy` library (Harris et al., 2020). To quantify the distribution, the 2D color-magnitude space is discretized into a grid of bins. Each cell in the grid is associated to a specific range of magnitude and color index, and its assigned value corresponds to the local galaxy number density. A linear regression is used to characterize the red sequence. To perform this fit, we represent the distribution by the centroid of each bins, which are then weighted by their respective local number density. A new mesh-grid is thus created, matching the dimensions of the initial 2D-histogram, where each node encodes the local density of galaxies (Figure 12).

To ensure the robustness of the regression and minimize the influence of contaminating highly dense areas in the histogram such as the confusion zone, a boolean mask is applied to the parameter space. This mask isolates the red sequence using boundaries.
On one hand, the magnitude range of the mask is constrained arbitrarily between mag 21 - 23. This interval corresponds to the range where the over-density trend is clearly distinguishable in the color-magnitude diagram created for this work and from the reference, even though it does not encompass the BCG. Indeed, in a color-magnitude diagram, the red sequence typically appears as high-density horizontal zones features.

On the other hand, the color-index range of the mask has been constrained by finding local minima in the color-index distribution. To focus on the red sequence horizontal trend, we first filter the detection catalog on the previously defined magnitude boundaries. By analysing the color-index histogram of the filtered catalog, one can isolate the specific region of the red sequence. The core of this method relies on kernel density estimation (KDE), which provides a continuous approximation of the underlying probability density function. It reveals natural over-densities that might be hidden in a standard binned histogram. The density gaps are then identified by locating either the local minima of the KDE or the first inflection point following its last peak. In the latter case, the second derivative of the KDE function has to be computed first. This inflection criterion has been adopted to counter the issue of a minimum being located at a really high color value, which would bias the boundary. The final product of the self-created "Gap Finder" algorithm automatically outputs the position of the gaps in a given histogram as shown in Figure 11.

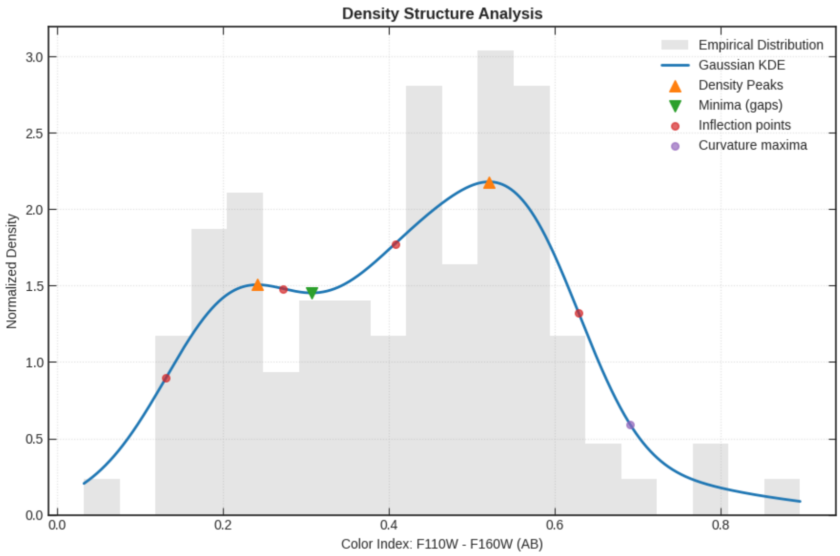

Figure 11: Histogram of the color index of sources in our selected magnitude range for the F110W filter where analytical information on the density of the distribution have been outlined. They have been obtained via a self-created "Gap Finder" algorithm and will be used to motivate our selection of overdensity regions.

The area where the known part of the red sequence lies has now been constrained by magnitude and color-index boundaries. These boundaries will thus be used to create a boolean mask on which a linear regression is performed (Figure 12). The regression line, fitted on the red sequence, with the equation $y = -0.049x + 1.588$ spans across the previously created mesh-grid in the color-magnitude space.

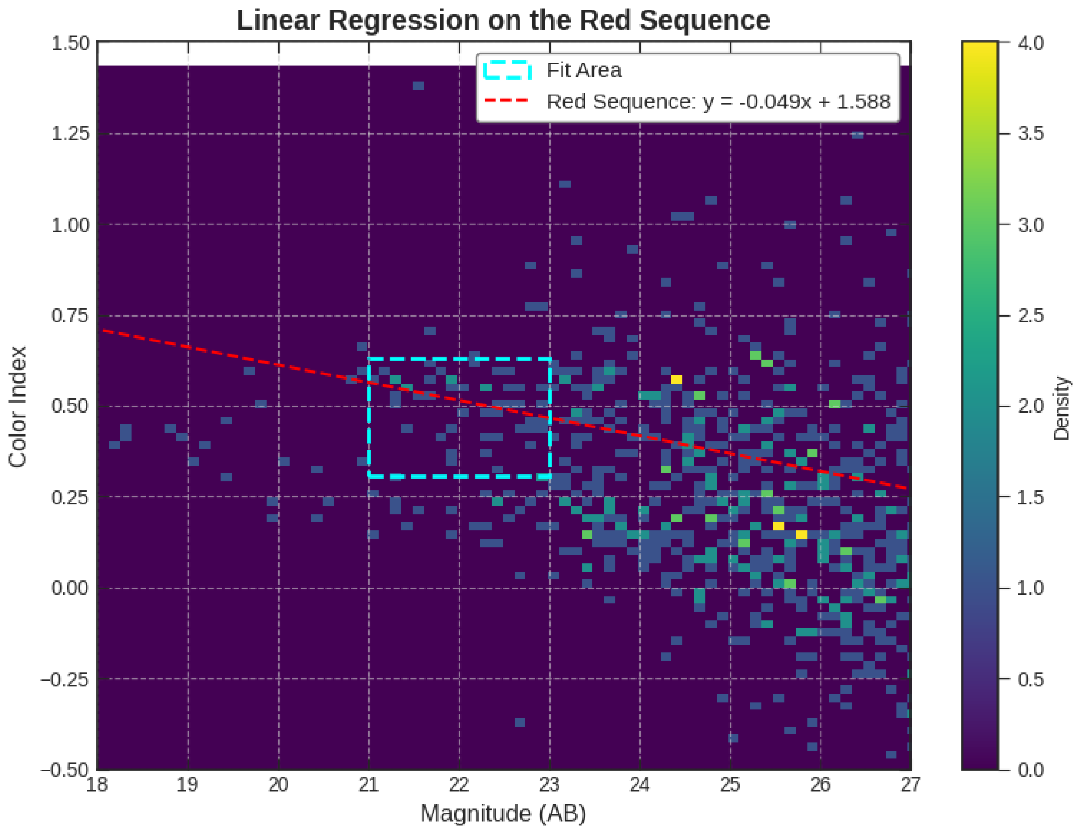

Figure 12: 2D histogram in color-magnitude space. The linear regression (red) weighted by galaxy density is fitted on the boolean mask (cyan) encompassing the red sequence.

Now that the red sequence has been approximated, the galaxies following that linear tendency have to be identified. To this end, we compute, for each galaxy, its residual to the best-fit line, representing the red sequence, defined as:

$$\delta = \text{color} - (a \cdot \text{mag} + b)$$

The distribution of these residuals allows the distinction between galaxies belonging to the red sequence and those belonging to the field.

In order to characterize the dispersion around the linear relation in the most robust way, the final choice for this work in terms of selection method was made in favor of the Median Absolute Deviation Standard Deviation (MAD STD). Contrarily to the standard deviation[3], the MAD is weakly sensitive to outliers and thus provide a robust estimation of the dispersion of the red sequence. It is expressed as follows for different elements i:

$$\text{MAD} = \text{median}(|x_i - median(x)|)$$

[3]As a reminder: $\sigma_X = \sqrt{E(X^2) - E(X)^2}$ with $E(X)$ the expected value (mean) of a variable X

However, the MAD alone does not give a value that can be compared to the standard deviation. Indeed, the standard deviation is the region where the inflexion point lies on a gaussian distribution. In a normal distribution, around $\sim 68\%$ of the data lie within $\pm 1\sigma$. Because the MAD is based on a median of a median, it encompasses precisely 50% of the data, which is less than a classical STD. To correct it, we multiply the MAD by a conversion factor:

$$\text{MAD STD} = 1.4826 \times \text{MAD}$$

This factor ensures the transition from encompassing 50% of the data to 68% like classical standard deviation. In simpler terms, the MAD STD is the expression of the classical standard deviation of a dataset if it had no aberrant values.

Because the density of sources around the linear fit is not comparable in the whole color-magnitude space, a magnitude dependence has to be introduced in the form of bins. The catalog is thus cut into magnitude bins and the dispersion around the best-fit line is computed independently in each bin. This choice allows to take into consideration the local and intrinsic variations of the photometric dispersion in function of the luminosity. This includes the augmentation of the noise for faint sources which we previously defined as the confusion zone. A global estimation would introduce a bias by assuming a constant width for the red sequence.

In each of these bins, the galaxies have been selected by applying a sigma-clipping criterion. Only the sources with a residual that satisfies $|\delta| \leq N \times \sigma_{MAD}$, with N an adjustable parameter that controls the width of detection, are selected. This criterion became an adaptable envelope that surrounds the linear relation, with a width that varies with the magnitude.
The selection range in magnitude has been set arbitrarily from ~ 18 to 23. It allows for the selection of the brightest sources of the cluster as well as sources up to $100\times$ fainter. This selection categorizes 53 galaxies as cluster members as shown in Figure 13.

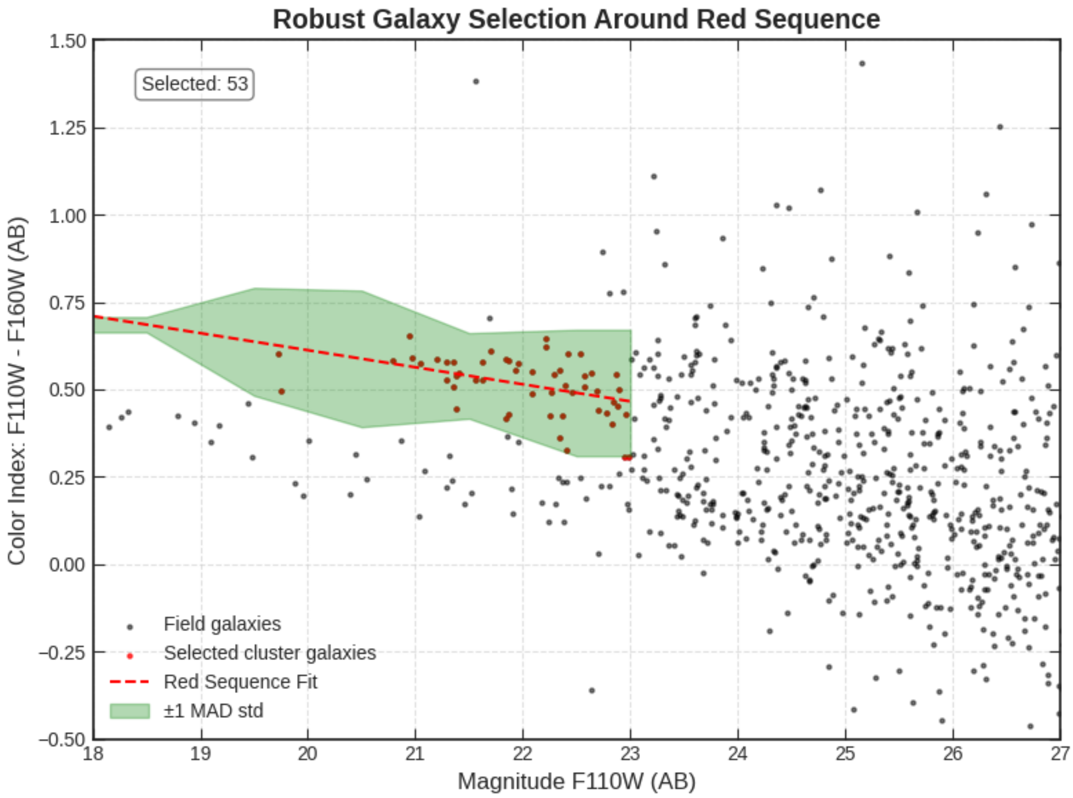

Figure 13: Selection of cluster members for SPT–CL J0356-5337 via a MAD STD criterion around a linear regression on the red sequence.

To validate the selection, we verified that the identified cluster members have a color index of a redder population. This was achieved by computing the $F606W - F110W$ color index. Since magnitudes are inversely proportional to the logarithm of the flux, a larger (more positive) index corresponds to a higher relative flux in the redder band (F110W) compared to the bluer band (F606W), thus confirming the expected red-leaning trend. Traditionally we could re-select every cluster members based directly on the color-magnitude diagram of these two bands, effectively eliminating the need for this criterion. This color-magnitude diagram along with the selected cluster members can be found in the appendix (Figure 27). However, as mentioned before, this pipeline being a proof of concept at the development stage, comparisons with reliable scientific sources were needed, thus justifying our choice of bands in the first place. To determine the optimal threshold for this color cut, the "Gap Finder" algorithm developed for this work was again employed. A curvature maximum at 1.468, located immediately following the primary density peak, was selected arbitrarily (Figure 14). This threshold was chosen as it effectively encompasses the majority of the first peak without overflowing upon the second, a compromise that would not have been achieved with other selection criteria. The former peak represents the blue component of the distribution, whereas the latter, shifted toward the right, identifies the redder population. When applied, the color cut excludes 3 sources for a total of 50 cluster members. The final selection can be seen in the color-magnitude diagram of Figure 15.

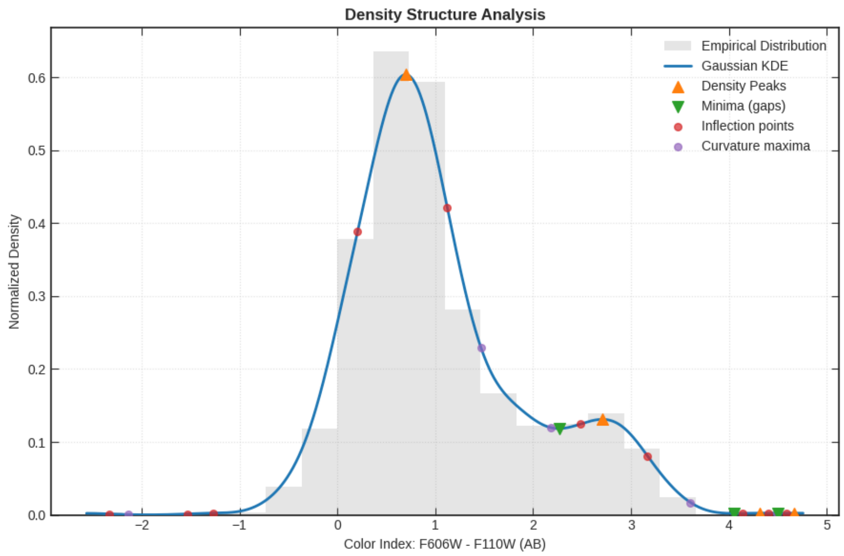

Figure 14: Histogram of the color index F606W-F110W where analytical information on the density of the distribution have been outlined by our "Gap Finder" algorithm.

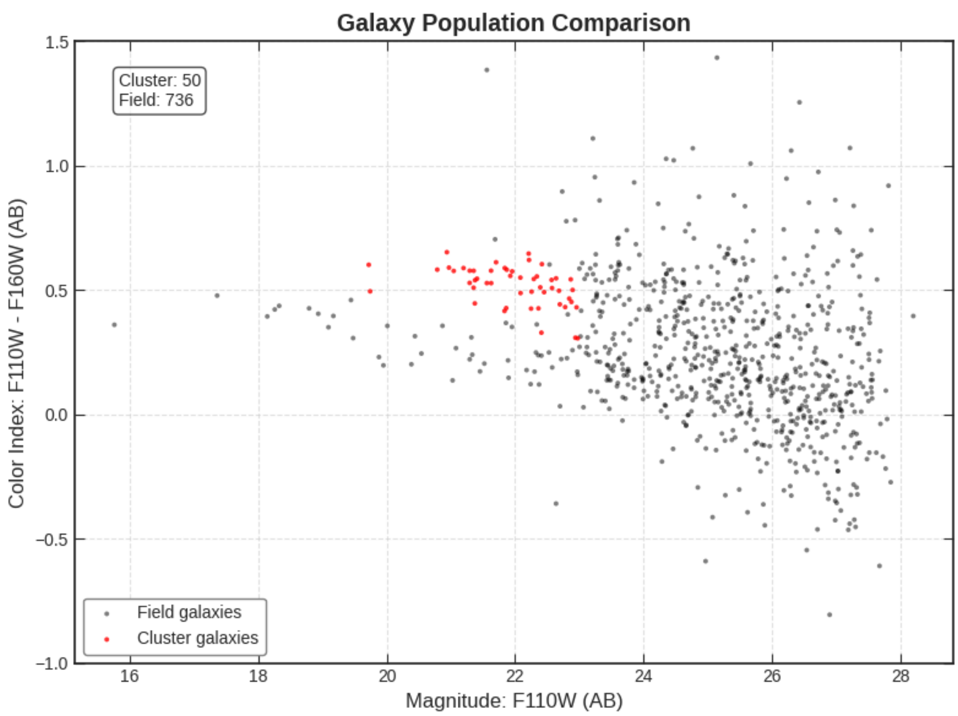

Figure 15: Color-magnitude diagram of SPT–CL J0356-5337 in the HST/WFC3 FoV with the selected cluster members outlined in red.

6.4.1.2 Alternative approximation

While the methodology detailed in the previous section requires significant parametrization and fine-tuning for the moment, a more direct alternative involves the use of the previously identified density gaps. This approach is based on a color-color diagram with a single-criterion cut applied to each axis. Only sources satisfying these threshold conditions are retained. Additionally, a magnitude constraint was implemented, defined as $mag_{BCG} \leq mag \leq mag_{BCG} + 5$. This selection includes sources ranging from the brightness of the BCG down to a factor of 100 times fainter. That boundary coincides with the point where magnitude uncertainties begin to increase exponentially (Figure 29 in the appendix).
This method offers the advantage of being driven only by density gaps. By removing the proximity requirement relative to the best-fit line, the selection is more permissive (Figure 28 in the appendix). Furthermore, it enables the exploration of lower-magnitude regimes, such as the confusion zone, where the MAD standard deviation method would no longer be robust. A comparison of the two methods can be seen in Figure 16 and a comparison on an RGB image is available in the appendix (Figure 31).

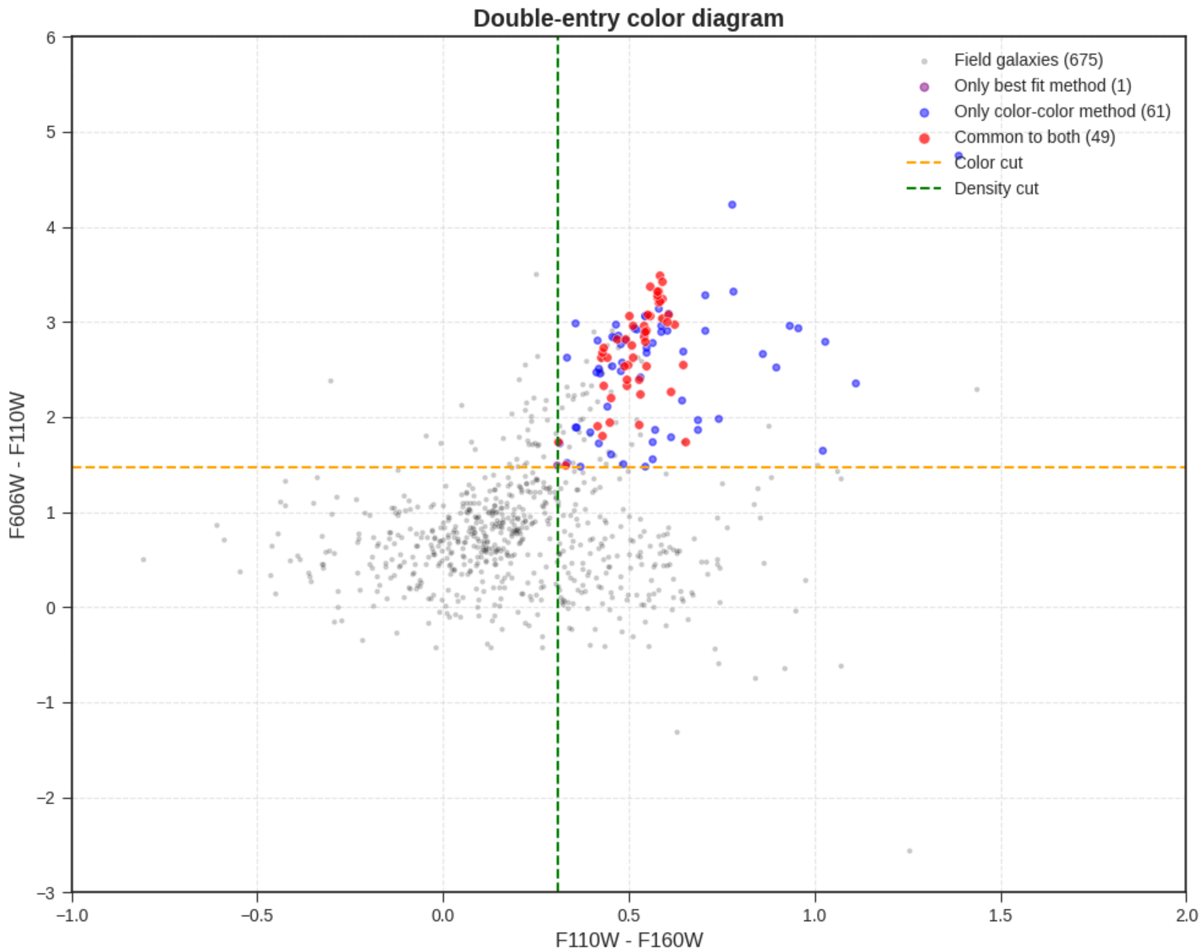

Figure 16: Color-color diagram of SPT–CL J0356-5337 in the HST/WFC3 FoV. A comparison in cluster member selection is displayed using different colors.

6.4.2 Area of influence

Prior to the SED comparison, a spatial fragmentation was performed on the photometric catalog containing the field galaxies. This step is motivated by the geometry of gravitational lensing. Indeed, multiple images of a lensed source are intrinsically clustered around their respective deflectors. By restricting the comparisons to localized regions of the FoV, we eliminate non-physical matches, lower the amount of false positives and reduce the computational cost. The implementation of this approach is described in this section.

The core of this approach involves transforming discrete cluster members into circular zones of influence. This geometric approximation identifies regions where background galaxies are susceptible to strong lensing effects. Specifically, the computation of these radii serves to delimit the typical spatial extent over which a galaxy's gravitational potential is strong enough so that it could manifest strong lensing evidence. The following development proposes an empirical approach combining distance from cluster member magnitudes and their luminosity (used here as a proxy of mass), which ensures that the model remains physically motivated while keeping computational simplicity.

For a source perfectly placed behind a lens, the strong lensing zone can be approximated by the Einstein radius (Figure 2 for lens notations):

$$\theta_E = \sqrt{\frac{4GM}{c^2}\frac{D_{LS}}{D_{OS}D_{OL}}}$$

With G, M and c being respectively the gravitational constant, the mass of the lens and the speed of light.
We make thus the approximation that multiple images will be found in a sphere of radius $R \sim \theta_E$ around the galaxies[4]. The following problem arises: we do not know the different distances in that relation. To address this issue, we make the following approximation:

$$\theta_E \sim \sqrt{\frac{4GM}{c^2}} \sim \sqrt{M} \Rightarrow \boxed{R \propto M^{1/2}}$$

Assuming a constant mass-to-light ratio[5] ($M/L \approx cst$, as first order approximation (Bell and de Jong, 2001)):

$$\boxed{M \propto L^{\alpha}} \text{ with } \alpha \simeq 1$$

[4]It would be more precise to say around the cluster. But by summing the different zones of influence later on, we will roughly approximate the one of the entire cluster.

[5]Technically, the M/L ratio is not strictly constant as it depends on the galaxy's stellar population (age, metallicity, and initial mass function). However, $\alpha \simeq 1$ remains a robust first-order approximation for the relatively homogeneous galaxies found in cluster environments.

We can also compute from the expression of the magnitude (Pogson, 1856) that:

$$
\begin{aligned}
& m = -2.5\log_{10}(F) + C \\
\iff \quad & \log_{10}(F) = \frac{C - m}{2.5} \\
\iff \quad & F = 10^{(C-m)/2.5} = 10^{\frac{C}{2.5}} \cdot 10^{-0.4m} \\
\iff \quad & \boxed{F \propto 10^{-0.4m}}
\end{aligned}
$$

The following relation can thus be obtained:

$$
\begin{aligned}
R \propto \theta_E \propto M^{1/2} \propto L^{1/2} \propto (10^{-0.4m})^{1/2} \\
\Rightarrow \boxed{R \propto 10^{-0.2m}}
\end{aligned}
$$

With this relation, a linear function of the magnitude can be used to approximate the zone of influence as radius $= a \cdot 10^{-0.2m} + b$.
That linear relation can be normalized for a reference magnitude m_0 and a proportionality constant A, we have $R_0 = A \cdot 10^{-0.2m_0}$.

Finally, for a reference magnitude m_0 and reference radius R_0 that have to be fine tuned based on the system, the zone of influence of the galaxies can be approximated by:

$$
\boxed{R(m) = R_0 \cdot 10^{-0.2(m-m_0)}}
$$

The reference parameters were visually calibrated by setting a scale radius of $R_0 = 800$ pixels for $m_0 = m_{BCG}$. This ensures that the BCG's potential encompasses the nearby gravitational arcs produced by strong lensing. The magnitude in the red band $F110W$ of each cluster member was then used to compute its radius of influence via the previously created relation. We used the magnitude in $F110W$ to compute the radius as this is the most sensitive filter and beyond the 4000Å break of cluster member galaxies ensuring that significant flux of the galaxy is present.

As it is the cluster's potential that is responsible for the strong lensing effect rather than the independent galaxies, we roughly model its shape. For each cluster member, we create a circular aperture of radius equal to its radius of influence centered on the sources centroid. This opening was then transformed into a binary mask, 1 corresponding to the inside of the zone. Each new mask created is added to a general mask incrementally. If two masks overlap, we simply merge them to create a single area. In the end, the different masks are labelled. This means that previously independent cluster members that have overlapping zones of influence will be merged as one single mask under the same label. It is worth mentioning, that the final step of this pipeline being based on pairwise matching, the mask that did not contain at least two sources have been discarded.

The different mask created based on the cluster member identified in section 6.4 can be represented in figure 17.

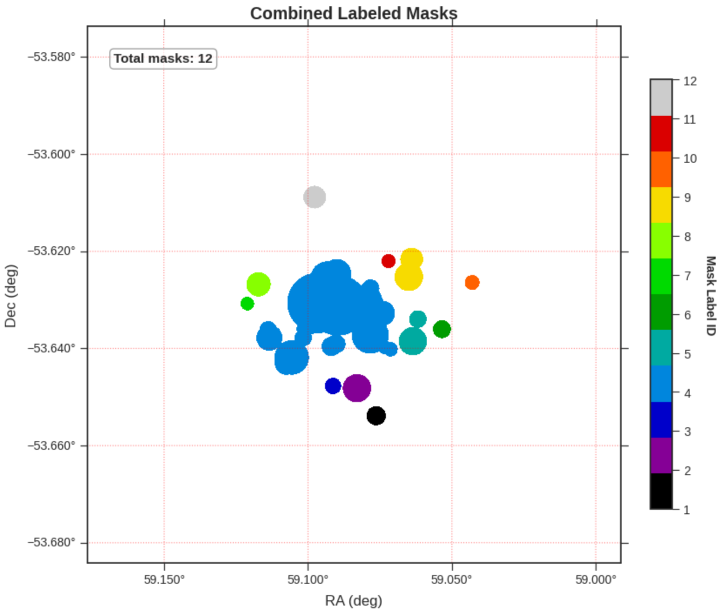

Figure 17: Combined labelled masks of the cluster members. This map shows the projected strong lensing zone in the RA/Dec plane. Each color represents a distinct connected component where individual galaxy masks overlap. The large central structure (Label 4) illustrates the merging of several masks in the cluster core, while peripheral galaxies remain as isolated labels.

A visual inspection of this image reveals that several isolated masks likely originates from wrongly identified cluster members located too far from the center of the cluster (periphery of the FoV). Given that these masks have not been merged with the main potential well and cover a negligible area, the matching of multiple images within them is highly unlikely. These galaxies are likely insufficiently massive and/or too distant from the cluster center to produce significant lensing effects. Although they could have been excluded, they were retained for the sake of completeness. As expected, the cluster members close to the BCG have merged into a single, larger structure (Mask No. 4). It can be seen as a first-order approximation of the overall cluster morphology, even though it is a rough estimate. This combined mask defines the primary strong lensing region where the collective gravitational potential is highest, and it is within this specific area that the discovery of multiple images is most likely.

The final step of this section is then to project this masked distribution onto the field galaxy catalog. The position of each source is analysed and the catalog is fragmented based on which mask a source belongs to. In addition to regrouping same region sources, it excludes the ones located too far from cluster members for visible lensing effects to take place. The final product of this section is thus a list of catalogs, each containing sources around the same group of cluster members.

6.5 Bloc 5: *Computation of similarity*

The catalog containing the detected field galaxies has now been fragmented into different groups containing potential pairwise matches among them. The next and final step of this pipeline is to assign a similarity score to each of the pairs in the different groups. For this purpose, we implemented a χ-type metric between two sources, A and B:

$$\chi^2(\alpha) = \Sigma_i \frac{(F_{A,i} - \alpha F_{B,i})^2}{\sigma_{A,i}^2 + \alpha^2 \sigma_{B,i}^2}$$

This metric is based on a sum of the flux across multiple bands i. It is designed to process an arbitrary number of filters. The term in the denominator combines the uncertainties. The term α serves as a normalization parameter to account for luminosity invariance. Since a faint source can share the same spectral shape as a more luminous one, one of the two compared SEDs must be rescaled to the other. This is achieved by determining the value of α that minimizes the metric, resulting in χ^2_{min}. Furthermore, as the metric's value naturally increases with the number of bands, even when the SEDs are closely matched, χ^2_{min} is normalized by the number of degrees of freedom. In this study, the number of degrees of freedom is defined as dof $= N-1$, where N represents the number of photometric bands and the subtraction of one accounts for the free parameter α determined during the minimization process.

$$\chi^2_{reduced} = \frac{\chi^2_{min}}{N-1}$$

This metric is computed for every pair of sources within a catalog fragment. The results are stored in a dictionary where each key corresponds to a source or segment ID, associated to a DataFrame of all other sources. These candidates are ranked by similarity in descending order based on their $\chi^2_{reduced}$ values.

This was implemented as an $\mathcal{O}(N^2)$ complexity algorithm, where N is the amount of source in one catalog. However, its computation time has been reduced due to the symmetric nature of the comparison and counts a finite number of operations $\frac{N(N-1)}{2}$. It has been fully vectorized via the `numpy` library.

The χ^2-type metric thus characterizes if two SEDs are similar. However, it does not capture if the similarity match is stable in a catalog, if it is a real similarity or just an accident, or even the reciprocity. For these reasons, we make the last transformation of this pipeline by introducing the notion of Mutual Nearest Neighbour (MNN). Two sources A and B are MNN if they are in each other's nearest-neighbor sets such that:

- B lies among the nearest neighbors of A
- A lies among the nearest neighbors of B

With this in mind, we chose to weight the $\chi^2_{reduced}$ metric with a term characterizing the mutuality in the similarity detection.

$$\boxed{\frac{2}{pos_{A\to B} + pos_{B\to A}}}$$

This expression is a function of the relative ranking of the two sources within each other's similarity catalogs. For two sources that identify each other as their respective best matches, the value approaches 1. Otherwise, it progressively decreases toward zero as ranks increase. This MNN term is then used to weight the SEDs similarity which has also been transformed accordingly with our problem.

In photometry, the total pixel noise encompasses several independent contributions, primarily the detector readout noise, the Poisson noise from the sky background, and minor calibration uncertainties. In practice, the added effect of these fluctuations can be modeled as a first-order Gaussian approximation, $\epsilon \sim \mathcal{N}(0, \sigma^2)$, where the standard deviation σ is the local Root Mean Square (RMS) of the background. Based on this Gaussian error model, the compatibility between two SEDs can be quantified using a likelihood-based similarity measure, normalized between 0 and 1.:

$$\boxed{exp\left(-\frac{\chi^2}{2}\right)}$$

All in all, a composite similarity metric between two sources SEDs can be expressed as:

$$\boxed{\text{Similarity} = exp\left(-\frac{\chi^2}{2}\right) \cdot \frac{2}{pos_{A\to B} + pos_{B\to A}}}$$

It should be emphasized that while this approach relies on several approximations and does not claim absolute precision, it is nonetheless rooted in physical principles and statistical motivation. It can thus be classified as a heuristic score probabilistically motivated rather than a real probabilistic model. At the end of this pipeline, all sources located within the same zone around identified cluster members have undergone pairwise comparisons. Each resulting pair has been assigned a similarity index to quantify the strength of their spectral match. Each detected source is now thus assigned a DataFrame ranking all other sources in its vicinity by decreasing order of similarity index.

7 Results and limitations

7.1 Global analysis

As mentioned in Section 6.2, the performance of this pipeline is evaluated based on its ability to successfully match the pairs in multiple images (sets 1, 2, 3, 5, and 7) as classified by Smith et al., 2025. However, it is worth to first examine the broader context. Specifically, we compare the similarity scores obtained within these confirmed lensed systems to the distribution of scores computed across all galaxy pairs within the cluster. The global distribution with the highlighted assessment sets are represented in Figure 18.

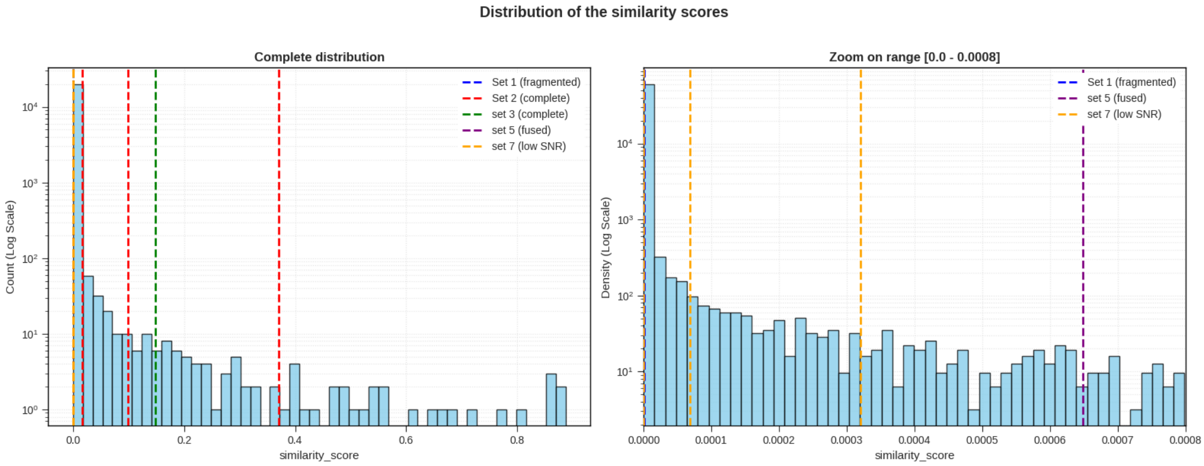

Figure 18: Distribution of similarity scores, with vertical lines highlighting the positions of pairs (two sources) in known multiple-image sets. Sets labeled as "fragmented" correspond to over-deblended sources, while "fused" sets indicate sources merged with neighboring objects. The left panel shows the full score distribution on a logarithmic scale, while the right panel provides a close-up view of the lowest bin near zero. This visualization demonstrates that true multiple-image pairs are not confined to the highest-scoring tier. Instead, they are outperformed by a large population of unlensed, high-scoring pairs. This significant overlap underlines that some true pairs exhibit critically low similarity scores, remaining buried within the background noise.

First, it is worth noting that the similarity scores of the multiple-image pairs are highly dependent on the quality of the segmentation of the sources and photometric accuracy. As shown in the left panel of Figure 18, the "complete" systems (such as Set 2 and part of Set 3) successfully stand out from the background, achieving relatively high similarity scores (0.1 to 0.4) and ranking in the upper part of the distribution. However, systems severely affected by imaging artifacts, such as Set 5 ("fused"), show scores near zero due to the contamination by the blending.

Surprisingly, Set 1 ("fragmented") also displays a very low global similarity score, even when isolating a pair of images that are individually unaffected by over-deblending. However, as it will be detailed later, a singular analysis of this specific pair reveals that the local ranking remains perfect. Indeed, the true counterpart is successfully identified as the

top match for the reference image. The collapse of its global score is thus entirely driven by an elevated χ^2 value. This is probably due to photometric differences or localized background noise which will heavily penalize the exponential term of our metric despite the optimal mutual ranking.
Secondly, the global distribution highlights the challenge of contamination by the unlensed pairs. The pipeline successfully pushes the vast majority of the 19,925 unlensed pairs into the very first bin, near zero, as shown by the logarithmic scale (Figure 18). However, as the distribution of unlensed pairs possesses a long, decaying tail that extends up to scores of ~ 0.9, a non-negligible number of random pairs still outscores the genuine lensed images. This outlines that while a simple quantile-based threshold is insufficient to isolate all multiple images due to photometric imperfections, the pipeline remains efficient at rejecting the bulk of the unlensed population. Figure 19 shows the 50 pairs with the highest similarity scores out of the 19,925 total combinations in the cluster. In these highlighted ellipses, only the Set 2 is partially recovered among the top-ranked pairs. Additionally, most of the unrelated images present in this top-50 list lack the characteristic circular or tangential symmetry expected in strong lensing configurations. Implementing a less-permissible geometric constraint to filter out these asymmetric configurations represents a promising future addition to significantly reduce contamination by unlensed pairs.

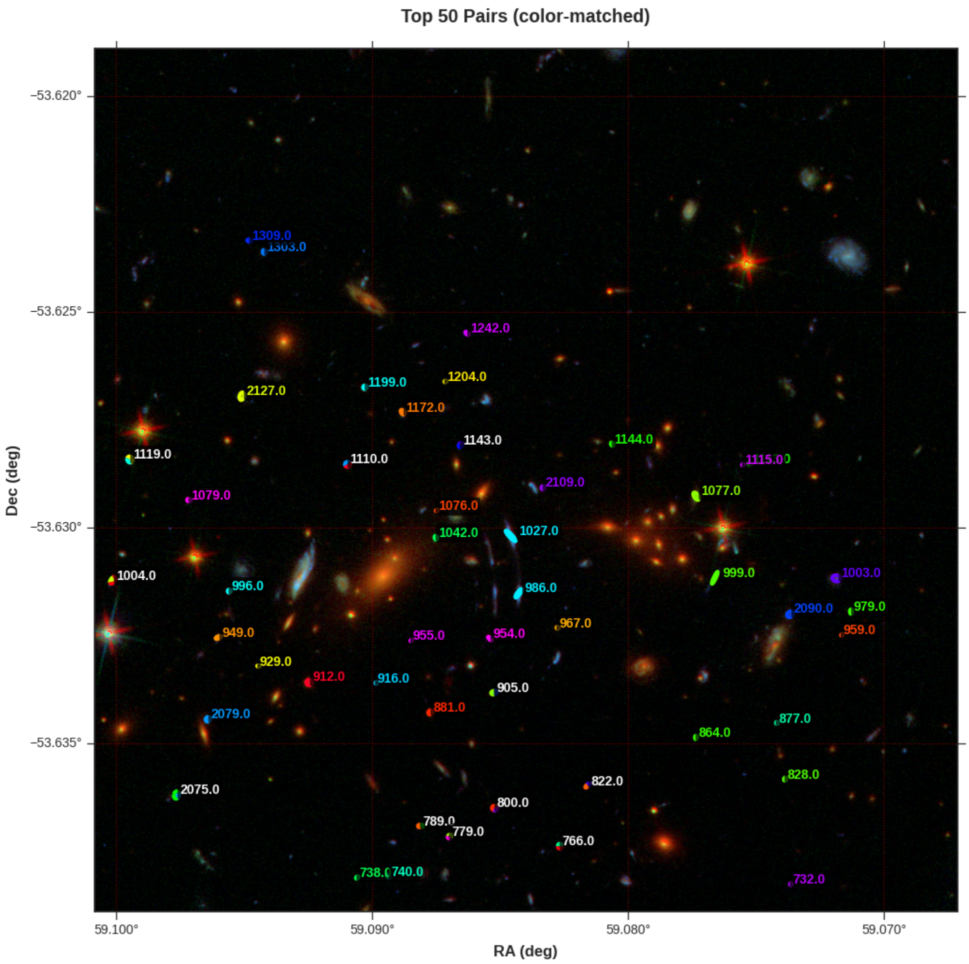

Figure 19: Spatial distribution of the top 50 pairs with the highest similarity scores. Each pair is visually mapped using matching colored ellipses, and source IDs in white indicate objects appearing in multiple top-tier pairings. To maintain clarity and prevent visual overcrowding, the representation is strictly limited to the 50 highest-scoring pairs. This plot highlights that the selected pairs are widely scattered across the field and lack the characteristic tangential alignment or geometric symmetry expected for genuine multiple images distributed around the cluster's center of mass.

7.2 Case-by-case analysis

Having analyzed the global properties of the score distribution, this subsection focuses on a more detailed, case-by-case analysis. The different image sets are isolated, and their SEDs are visually inspected to understand their direct influence on the final similarity score. It is worth noting that the SEDs presented below are extracted in the observer frame and are thus not corrected for redshift. For a proper physical comparison, wavelengths must be scaled by a factor of $(1+z)^{-1}$. As example, given that the cluster SPT–CL J0356-5337 lies at $z \sim 1.03$ (Smith et al., 2025), observer-frame wavelengths must be divided by 2.03 to determine the corresponding rest-frame wavelengths for cluster member galaxies.

A visual representation of the spatial position of every sources detailed/mentioned in this subsection can be seen in the Figure 30 in the appendix.

7.2.1 Set 1

This specific set is characterized by a source that has suffered from over-deblending. The lower region of segment 2096 was fragmented and blended with a neighboring source. This artifact is clearly visible in the plotted SEDs, where segments 2096 and 2097 display significant deviation compared to the other set members (Figure 20). Specifically, the blue end of the spectrum is mainly captured in segment 2096 and appears substantially lower in segment 2097. This spectral behavior is consistent with the imaging data, as segment 2097 lacks the dense blue core originally present in the source. Furthermore, the SED of segment 2096 exhibits a noticeable drift around 1150 nm, which matches the expected contamination from the redder neighboring source with which it was merged.

For this system, the pipeline failed to associate the over-deblended segment with the other members of the set. Furthermore, both genuine members were incorrectly matched with segment 2061 and exhibit a low mutual similarity score of $\sim 10^{-7}$. Although the SED of segment 2061 matches perfectly with segment 1172 and nearly perfectly with segment 977, its photometry and spatial position remain questionable. Indeed, the deblending threshold applied to this segment and its neighboring source needs further investigation, as the two objects are nearly overlapping. Furthermore, this source is located significantly further away from the core configuration than the other images in the set. This case might once again point out the necessity of incorporating a less-permissible geometric constraint to filter out these potential outliers.

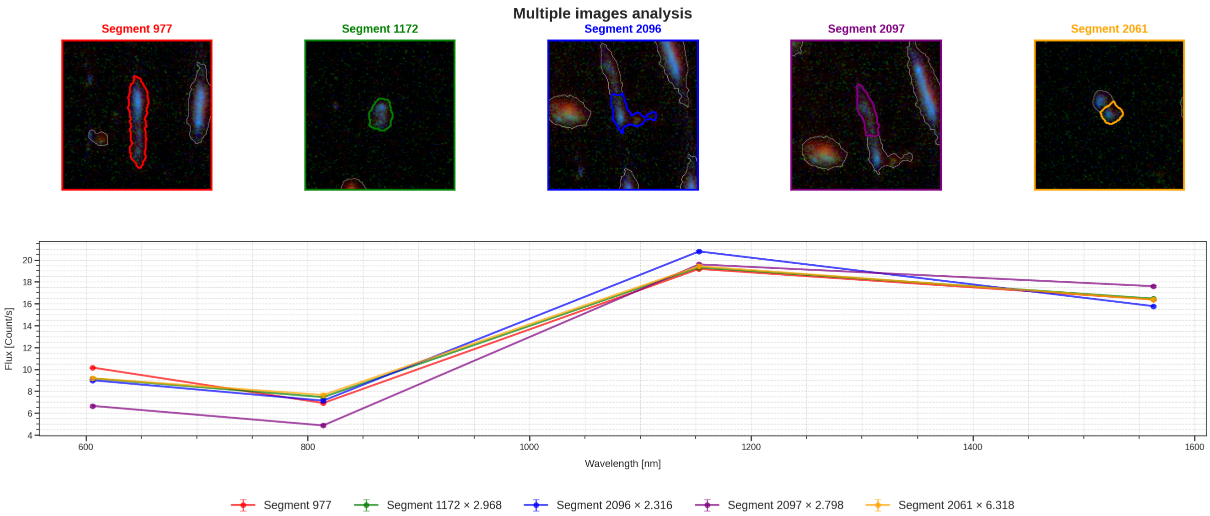

Figure 20: Comparison of the SEDs for the Set 1 members alongside the similar galaxies identified by the pipeline. Colored outlines define the boundaries of the segmentation masks. Each SED has been rescaled using the optimal offset from the χ^2-like metric. The true multiple images correspond to segments 977, 1172, and the combined segments 2096 and 2097. Segment 2061 is also displayed as it shows a high similarity score within the set. This highlights the challenges associated with source segmentation.

7.2.2 Set 2

This second system serves as an excellent example of the pipeline's best performance. The three distinct sources are mutually identified as the top match within each other's similarity rankings. This correlation is clearly reflected in the SED profiles (Figure 21), where the different curves overlap nearly perfectly. Beyond just having optimal mutual rankings, this system stands out as the highest-scoring set across the entire sample. As shown in Figure 18, the three corresponding pairs have similarity metrics of 0.370, 0.099, and 0.017, respectively. It is worth noting that even when a substantial SED overlap exists for these real multiple-image pairs, their similarity scores remain significantly below 1 and are surpassed by the higher-scoring pairs. This suggests that while SED-matching serves as a powerful exploratory tool for validation between sources, it may not function as a stand-alone extraction method. Indeed, as seen in Section 7.1 and detailed later, relying solely on this criterion leads to contamination mismatch, as a major fraction of the top-ranking pairs consists of unlensed sources.

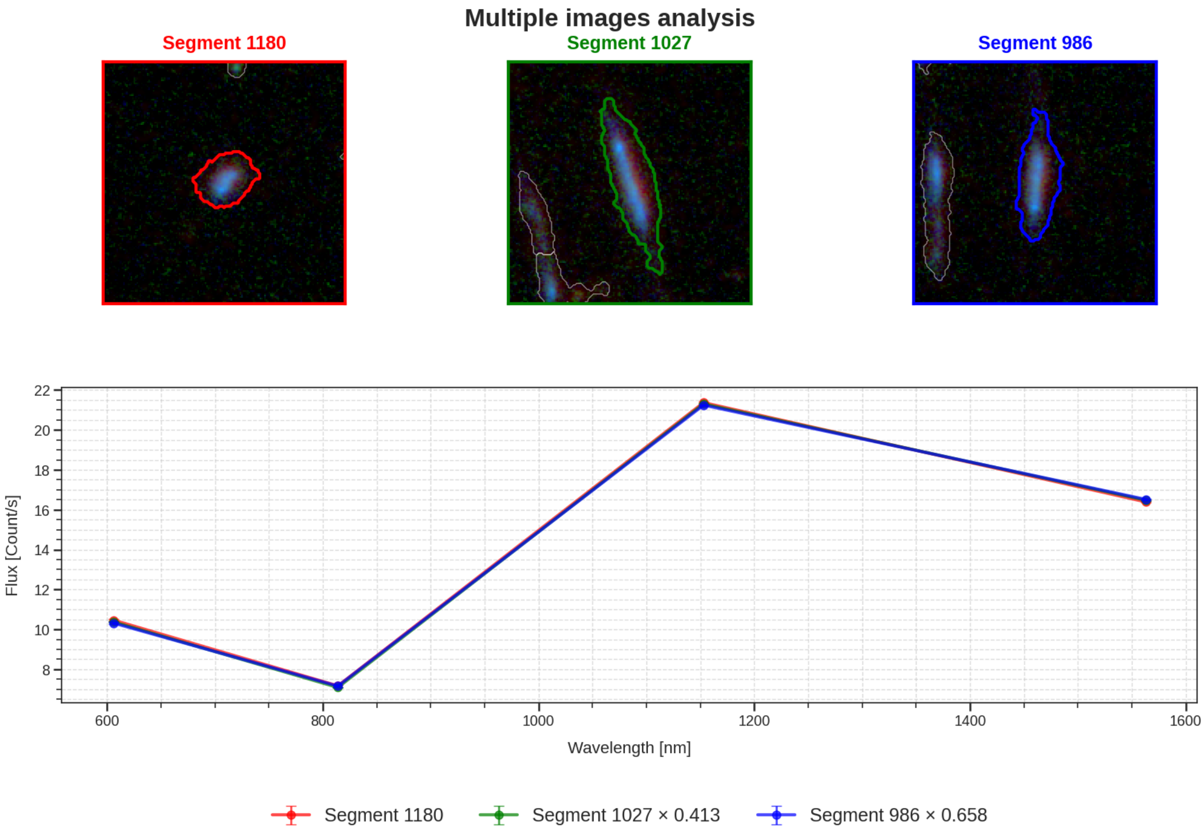

Figure 21: Comparison of the SEDs for the Set 2 members. Colored outlines define the boundaries of the segmentation masks. Each SED has been rescaled using the optimal offset from the χ^2-like metric. These three segments have been identified as the most similar to one another by the pipeline by cross-identification.

7.2.3 Set 3

This third set demonstrates mixed results. On one hand, segments 928 and 1093 are mutually identified as most similar, with a score of 0.149. On the other hand, segment 1188 is not associated with its true counterparts. This discrepancy is clearly shown in the SEDs. While the first two segments have a perfect overlap, the profile of segment 1188 shows a notable drift, particularly at shorter wavelengths. Instead, the pipeline identifies segment 657 as the top match for segment 1188. However, despite being ranked as the most similar candidate, their respective SEDs do not accurately overlap (Figure 22).

This detection failure could mainly be attributed to the unusual morphology of the source, which features two distinct, detached structures. Given that the source is well-isolated, local contamination from neighboring objects would be unexpected. Instead, the discrepancy likely points to inaccurate photometry due a faulty segmentation of segment 1188 such as a flux deficit caused by unrecovered emission. However, visual inspection does not clearly confirm such a deficit, and this mismatch thus remains an unresolved anomaly. In the end, this case underscores the extreme care required when performing photometry on complex, non-contiguous structures.

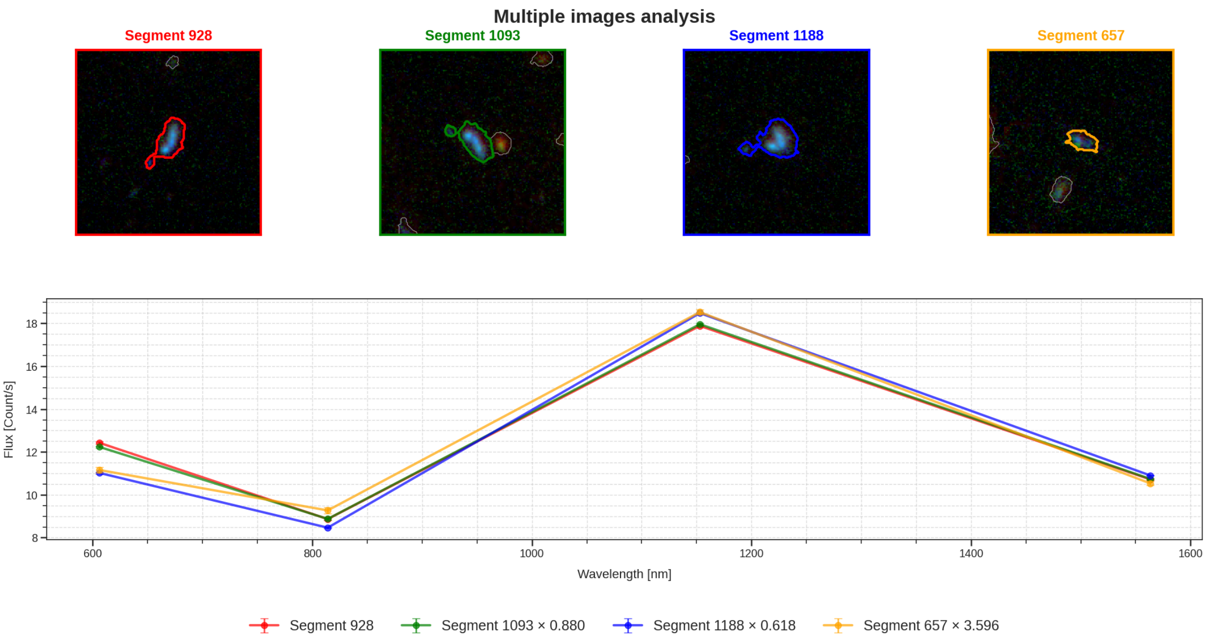

Figure 22: Comparison of the SEDs for the Set 3 members alongside the similar galaxies identified by the pipeline. Colored outlines define the boundaries of the segmentation masks. Each SED has been rescaled using the optimal offset from the χ^2-like metric. The true multiple images correspond to segments 928, 1093, and 1188. Segment 657 is also displayed as it shows a high similarity score with the set. This highlights the challenges associated with faint-sources comparison and unusual source's morphology during the photometry.

7.2.4 Set 5

Although this system was only classified as a candidate in the reference article and not included as a primary constraint for the lens model, its analysis remains valuable for evaluating the pipeline's limitations. In fact, this example represents a complete mismatch within this framework, as the three set members fail to be linked with one another. This outcome was anticipated for segment 973, being heavily blended with neighboring sources, and becomes clearly evident by its highly divergent spectral profile (Figure 23). On the other hand, segments 929 and 948 were incorrectly matched with segments 949 and 1073. Their respective similarity scores of 0.19 and 0.14 initially hint toward a good match. However, the spatial position of these candidates lacks the characteristic circular geometry expected in multiple-image configurations.

Furthermore, it is worth noting that these sources all exhibit a very low total flux, making their measurements uncertain. Such faint objects should have been theoretically excluded by the signal-to-noise ratio threshold applied to the catalog. However, in this work, the photometric error was defined strictly as the local RMS of the background. A more rigorous estimation of the associated uncertainties would potentially be beneficial for this type of pipeline, especially given its heavy influence on the χ^2-like metric.

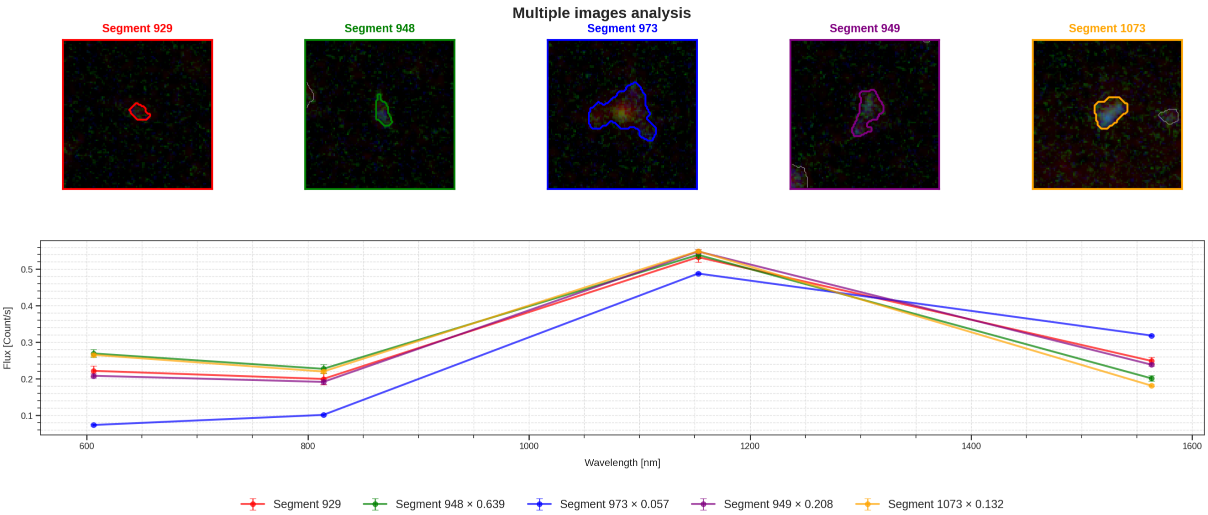

Figure 23: Comparison of the SEDs for the Set 5 members alongside the similar galaxies identified by the pipeline. Colored outlines define the boundaries of the segmentation masks. Each SED has been rescaled using the optimal offset from the χ^2-like metric. The true multiple images correspond to segments 929, 948, and 973, the latter being merged with a neighboring source. Segment 949 and 1073 are also displayed as they show a high similarity score with the set. This highlights the challenges associated with faint-sources comparison and segmentation.

7.2.5 Set 7

This final set did not pass the signal-to-noise ratio selection criterion. Indeed, like the previously analyzed Set 5, these sources possess a very low intrinsic flux. The data points in the first photometric band display extremely low values while maintaining visible error bars (Figure 24). Since our selection criterion is designed to exclude any source falling below the SNR threshold in at least one band, this single low-flux data point was sufficient to successfully discard the entire system from the final analysis.

In order to perform an analysis despite this exclusion, the system was manually reinjected into the pipeline. However, this case serves as a reminder that the parametrization of the signal-to-noise ratio threshold requires careful tuning for future iterations. That being said, the pipeline successfully identified the three sources as mutual best matches, although with low similarity scores ($\sim 10^{-4}$, $\sim 10^{-5}$ and $\sim 10^{-16}$). Interestingly, a slight discrepancy arises in the respective ranking DataFrames. Indeed, segment 884 exhibits a slightly different spectral profile than the others. This variation was captured by the pipeline as, while the other sources successfully grouped themselves within the similarity DataFrame of segment 884, the pipeline preferred a different ranking configuration for segment 827.

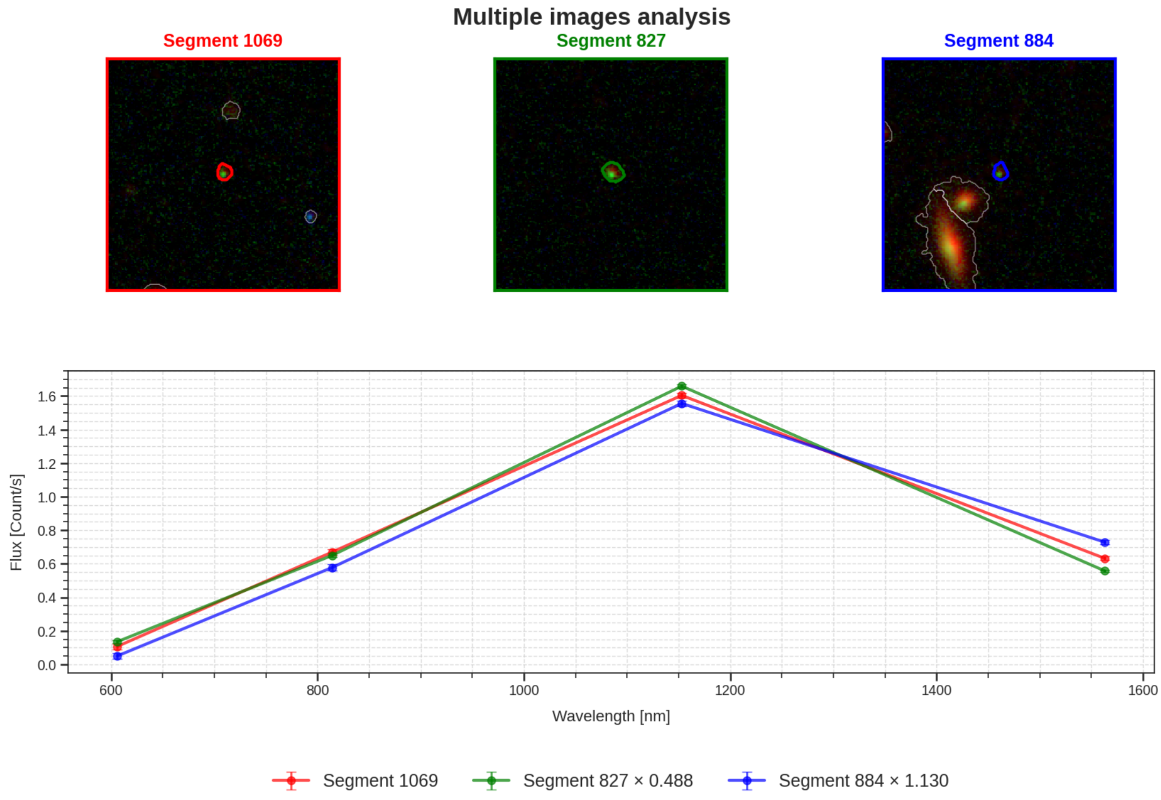

Figure 24: Comparison of the SEDs for the Set 7 members. Colored outlines define the boundaries of the segmentation masks. Each SED has been rescaled using the optimal offset from the χ^2-like metric. These images did not pass the Signal-to-Noise criterion. The three segments have been identified as top-match after cross-validation although with a low similarity score. Segment 827 was not found at the top of each ranking dictionary.

7.2.6 Best matches

As a further exploration of the results, it is interesting to analyze the nature of the highest-scoring pairs in the global distribution. They are displayed pairwise from left to right in Figure 25. All selected pairs in this case have similarity scores above 0.8, which is confirmed by the perfect overlap of their SEDs.
A detailed inspection of these three top-matches could hints toward different types of pipeline contamination. Physical causes can be proposed for each pair to justify the high matching score.
The first pair (segments 912 and 1110) could consists of two early-type galaxies. Based on their color compared to other known cluster members, these sources are likely remnants that were missed by the initial red sequence selection criterion. Because those galaxies share nearly identical stellar populations, their χ^2 minimization is optimal, leading to a high similarity score.
The second pair associates segment 766 with segment 1004. Here, the match could be due to local contamination, as segment 1004 is located in the immediate vicinity of a bright and saturated foreground star. This contamination heavily distorts the extracted SED and results in an accidental alignment with segment 766.
The third pair (segments 769 and 1240) represents very faint, low-flux sources. In this low signal-to-noise ratio regime, the SEDs are nearly flat as they are dominated by the associated background noise. This lack of features could again result in a faulty pairing.
This analysis of the top-matches, although maybe not representative of all the best matches, outlines the complexity of the problem. Indeed, the origins of contamination are multiple. Further fine tuning is thus necessary to make this pipeline fully reliable.

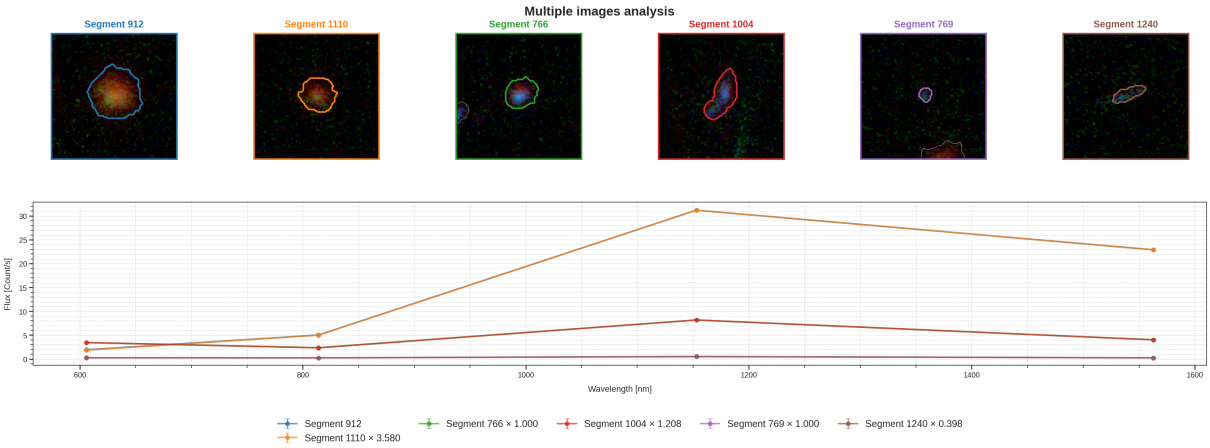

Figure 25: Comparison of the SEDs for the best pairs identified by the pipeline. The pairs are ordered from left to right as: 912-1110, 766-1004 and 769-1240. The colored outlines indicate the boundaries of the segmentation masks. Each SED has been rescaled with an optimal offset to show the configuration that minimizes the χ^2-like metric. Each case could illustrate a distinct origin for unlensed high-similarity pairs.

7.2.7 Cluster members

Following the previous analysis of the best matches, an additional inspection on known cluster members can be performed. For this purpose, we isolate the groups of Luminous Red Galaxies (LRGs) as defined in Section 6. Unsurprisingly, their respective SEDs exhibit an excellent overlap, which matches the relation observed in the examples of Section 7.2.6 (Figure 26).
This uniformity is a direct consequence of the physics of LRGs, which are dominated by evolved stellar populations leading to standardized spectral shapes. Furthermore, without any prior filtering, these cluster members naturally optimize the χ^2-like metric, creating a substantial reservoir of high-scoring pairs. This result outlines the critical importance of implementing a robust red sequence rejection algorithm. Rather than being just an optimization step, the removal of the red sequence is a mandatory requirement to prevent the pipeline's top rankings from being systematically contaminated by the cluster's passive galaxy population.

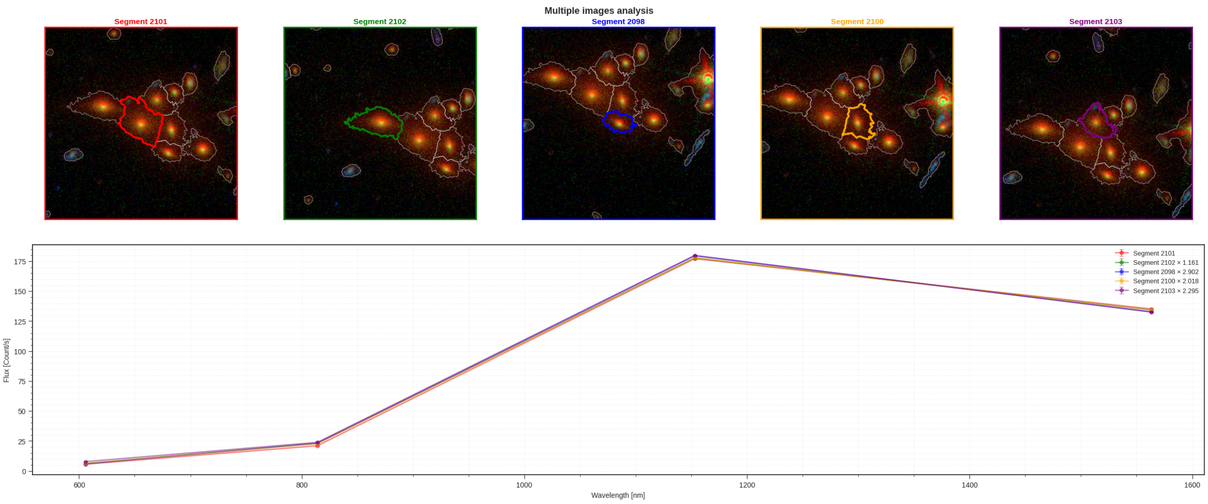

Figure 26: Comparison of the SEDs for known cluster members. The colored outlines indicate the boundaries of the segmentation masks. Each SED has been rescaled with an optimal offset to show the configuration that minimizes the χ^2-like metric. Their near-perfect overlap shows that the red sequence extraction is a critical step to prevent the introduction of unlensed high-similarity pairs.

8 Conclusion

This work presents a first step toward an automated detection algorithm designed to identify multiple-image sets in crowded cluster fields. The pipeline first performs multi-band photometry to create a reference detection catalog, built from a co-added white light image combining data across all available bands. It then conducts a separation between field galaxies and cluster members by fitting a linear regression on the cluster's red sequence. The total flux of the galaxies classified as cluster members is then used as a mass proxy to define a localized "area of influence", restricting the pairwise comparisons to physically justifiable regions. Within these zones, potential strongly lensed candidates are evaluated using a two-stage similarity score. The first stage is based on a χ^2-like metric, where the SEDs are rescaled relative to one another for minimization. The second stage combines a normal probability re-expression with a mutual nearest-neighbor criterion to refine the pairing. The final product is a pairwise similarity ranking for each source.

The resulting similarity ranking assigned to each candidate source thus provides a framework for identifying multiple images of the same lensing system, as true counterparts are expected to mutually rank at the top of each other's lists. The analysis of this output on the galaxy cluster SPT–CL J0356-5337 reveals that photometric precision and galaxy differentiation are the most sensitive parameters. By challenging the initial assumption of perfect SED similarity, they directly limit both the purity and completeness of our final sample. While the pipeline successfully rejected the bulk of the 19925 candidate pairs by pushing the huge majority to the lowest similarity bin, a non-negligible tail of false positive extends up to scores of ~ 0.9. In its current state, a simple threshold on the SED-matching pipeline is insufficient to isolate multiple images, highlighting the need for additional criteria such as potential spatial constraints.

The pipeline achieved its best performance for Set 2 as the three distinct lensed images were mutually identified as top matches with high similarity ranging from 0.017 to 0.37 due to satisfactory SEDs overlap. However, the performances went down for systems suffering from flux contamination by neighboring sources and crowded-field blending. Sets 1 and 5 revealed two well-defined challenges that offer clear directions for improvement. In Set 5, contamination from a neighboring source reduced the similarity score toward zero, while Set 1 exposed a sensitivity to over-deblending that introduced a significant spectral shift. Rather than mere limitations, these cases serve as valuable diagnostics. They precisely identify where the algorithm's reliance on global extraction parameters reaches its boundaries. This could highlight the need to transition toward localized, fine-tuned thresholds during the segmentation, and deblending. Implementing such a case-by-case photometry could perhaps improve the precision in crowded cluster cores but will come at the expense of full automation.

Detecting faint sources and accurately measure their uncertainty also challenges our matching algorithm. Lower-flux systems, such as Set 7, failed to pass the initial Signal-to-Noise ratio selection criterion. Indeed, a single low-flux data point in the first photometric band fell below the threshold for two images of the set, which discarded the system. Furthermore, very-faint unlensed sources, like segment 769 and 1240, achieved artificial top-matching scores above 0.8 because their flat and noise-dominated SEDs optimized χ^2 minimization. This highlights a vulnerability in our error estimation which was strictly approximated using the RMS of the background sky. Future work could thus implement a dynamic optimization of the SNR threshold based on specific cluster environments. This approach could potentially improve the accuracy of recuperating faint, low surface brightness objects, which can be critical components of lensing systems.

The high-scoring unlensed pairs suffered from contamination by various physical look-alikes and remaining cluster members. Such faint sources are typically missed by our prior red sequence identification because of their low luminosity. Alongside early-type galaxies like segments 912 and 1110, their identical or featureless spectral shapes naturally optimize the χ^2-like metric, creating a significant source of sample contamination. Crucially, this result proves that a robust red sequence rejection algorithm is a mandatory requirement rather than just an optimization step. However, it also hints toward a potential alternative use of SED-matching for the differentiation of cluster members in a field. Future work could thus focus on improving cluster member decontamination by integrating pre-existing subtraction algorithms and tighter color-magnitude cuts before computing similarities.

While the current framework serves as a reliable verification tool for evaluating pre-existing candidates, scaling it to execute a blind detection of new multiple-image sets within a cluster catalog requires breaking away from manual cross-identification. To automatically isolate multiple-image sets from the thousands of random combinations, future work could investigate unsupervised clustering techniques. By analyzing mutual pairwise similarities simultaneously rather than relying on isolated pairs, these algorithms could isolate potential candidate sets for efficient visual verification. Most importantly, the majority of our high-scoring unlensed mismatches, such as the pairs involving segments 949 and 1073, could potentially be discarded because they lack the characteristic configurations of strong lensing. Integrating a spatial constraint term into the ranking metric that penalizes configurations not expressing the tangential, radial, or circular symmetries expected around a cluster core, will drastically improve the pipeline's purity. Ultimately, further developments must continue this analysis on larger and more diverse set of sight-lines. Testing the pipeline with cluster of different lensing efficiency, different redshift spaces, and varying blank and crowded fields will thus be an additional step to establish this method as a complement to standard gravitational lens-modeling tools.

Finally, while Euclid's spatial resolution is more limited compared to HST or JWST, this work can be seen as a pioneering step in the automated search for multiple images. Developed in parallel to dominant Machine Learning techniques, this pipeline provides a complementary method that has the advantage of being intuitively comprehensible and transparent.

Appendix

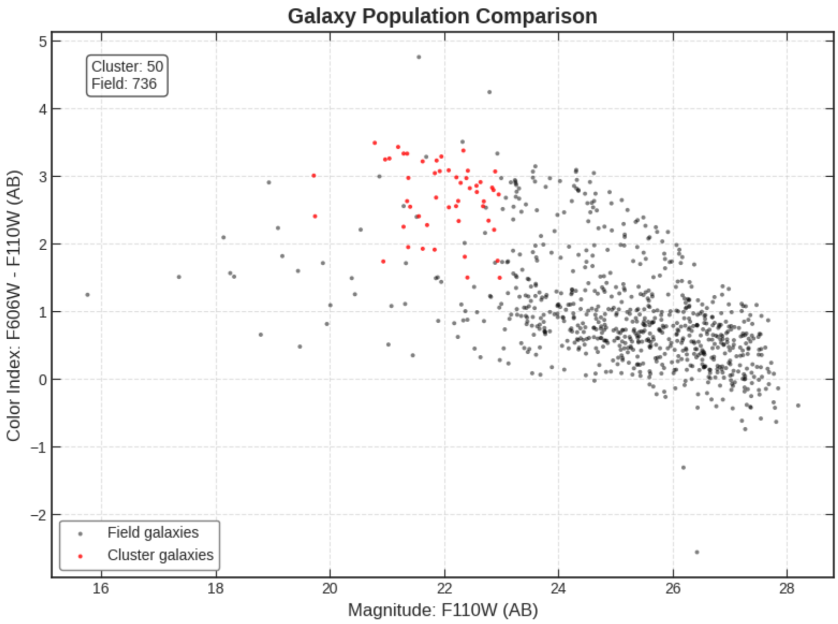

Figure 27: Color-magnitude diagram of SPT–CL J0356-5337 in the HST/WFC3 FoV created with this work photometric catalog. The color index represents F606W-F110W. The selected cluster members with the best-fit method have been outlined in red. A noticeable dispersion toward bluer colors suggests a potentially over-permissive selection criterion.

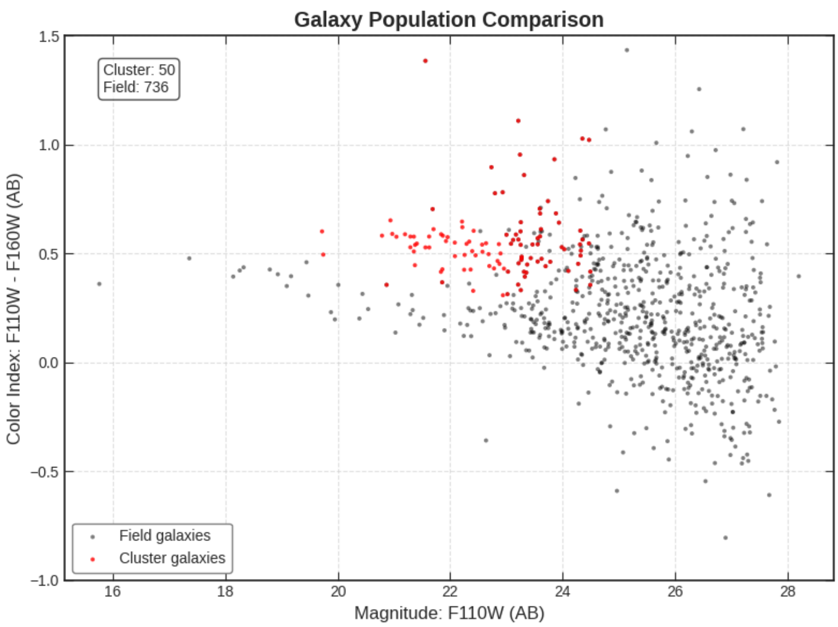

Figure 28: Color-magnitude diagram of SPT–CL J0356-5337 in the HST/WFC3 FoV created with this work photometric catalog. The color index represents F110W-F160W. The selected cluster members with the color-color method have been outlined in red. As mentioned in the text, it is more permissible than the best-fit method.

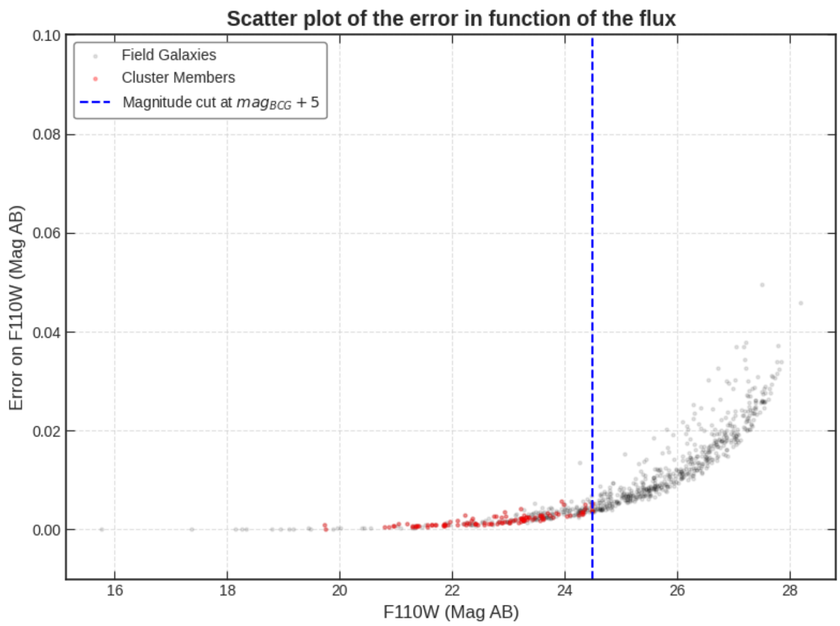

Figure 29: Evolution of the error with the magnitude. The selected cluster members with the color-color method have been outlined in red.

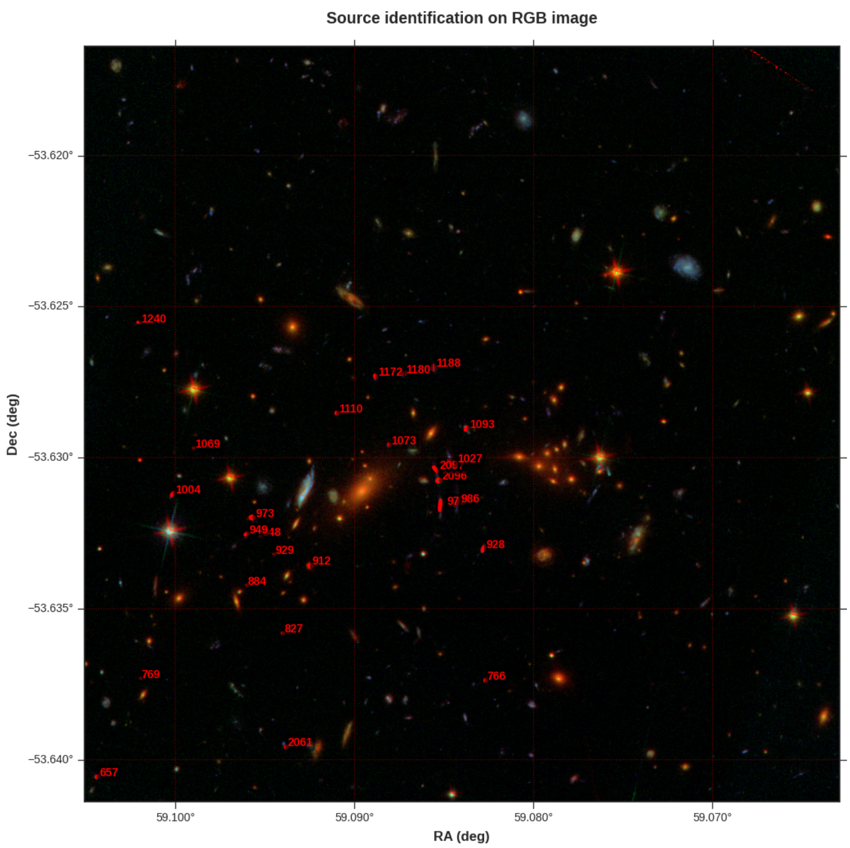

Figure 30: Visualization of the spatial position of each sources analyzed in the results section. Sources concerned have been outlined with a red ellipse and the id of their segment has been written next to it.

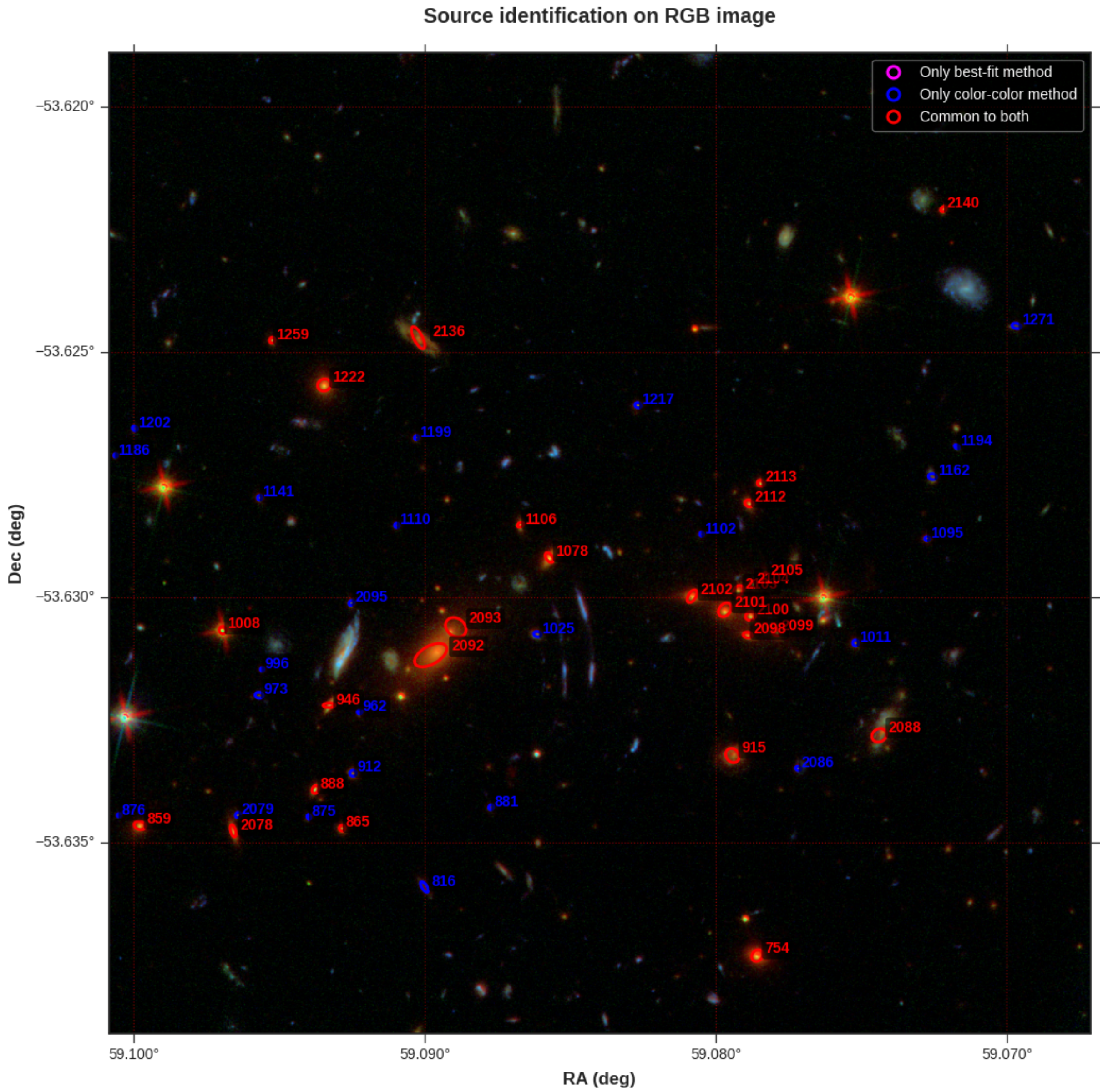

Figure 31: Visual comparison of the selection of cluster members selected via the two methods presented in section 6.4.1.2. The RGB image has been created via a python script using Astropy.

References

Abell, G. O. (1958). The distribution of rich clusters of galaxies. *The Astrophysical Journal Supplement Series*, *3*, 211. https://doi.org/10.1086/190036

Alard, C. (2006, June 30). Automated detection of gravitational arcs. https://doi.org/10.48550/arXiv.astro-ph/0606757

Avestruz, C., Li, N., Zhu, H., Lightman, M., Collett, T. E., & Luo, W. (2019). Automated lensing learner: Automated strong lensing identification with a computer vision technique. *The Astrophysical Journal*, *877*(1), 58. https://doi.org/10.3847/1538-4357/ab16d9

Avila, R. (2016). ACS instrument handbook. Retrieved June 5, 2026, from https://www.stsci.edu/files/live/sites/www/files/home/hst/documentation/_documents/acs/acs_ihb_cycle24.pdf

Bahcall, N. A. (1996, November 19). Clusters and superclusters of galaxies. https://doi.org/10.48550/arXiv.astro-ph/9611148

Bell, E. F., & de Jong, R. S. (2001). Stellar mass-to-light ratios and the tully-fisher relation. *The Astrophysical Journal*, *550*, 212–229. https://doi.org/10.1086/319728

Bertin, E., & Arnouts, S. (1996). SExtractor: Software for source extraction. *Astronomy and Astrophysics Supplement Series*, *117*, 393–404. https://doi.org/10.1051/aas:1996164

Beucher, S. (1992). The watershed transformation applied to image segmentation. *Scanning Microscopy Supplement*, 299–314.

Biermann, P. (1978). On the abundances of the chemical elements in intergalactic matter. *Astronomy and Astrophysics*, *62*, 255–258. Retrieved February 21, 2026, from https://ui.adsabs.harvard.edu/abs/1978A&A....62..255B

Böhringer, H., Dolag, K., & Chon, G. (2012). Modelling self-similar appearance of galaxy clusters in x-rays. *Astronomy & Astrophysics*, *539*, A120. https://doi.org/10.1051/0004-6361/201118000

Bower, R. G., Lucey, J. R., & Ellis, R. S. (1992). Precision photometry of early-type galaxies in the coma and virgo clusters: A test of the universality of the colour-magnitude relation - II. analysis. *Monthly Notices of the Royal Astronomical Society*, *254*(4), 601–613. https://doi.org/10.1093/mnras/254.4.601

Bradač, M., Clowe, D., Gonzalez, A. H., Marshall, P., Forman, W., Jones, C., Markevitch, M., Randall, S., Schrabback, T., & Zaritsky, D. (2006). Strong and weak lensing united. III. measuring the mass distribution of the merging galaxy cluster 1es 0657558. *The Astrophysical Journal*, *652*(2), 937–947. https://doi.org/10.1086/508601

Bradley, L., Sipőcz, B. M., Robitaille, T. P., Tollerud, E. J., Vinícius, Z., Deil, C., Barbary, K., Wilson, T. J., Busko, I., Donath, A., Günther, H. M., Cara, M., Lim, P. L., Meßlinger, S., Conseil, S., Droettboom, M., Bostroem, K. A., Bray, E. M., Bratholm, L. A., … Rathi, S. (2026, April 18). *Photutils*. Zenodo. https://doi.org/10.5281/zenodo.19636730

Bradt, H., Mayer, W., Naranan, S., Rappaport, S., & Spada, G. (1967). Evidence for x-radiation from the radio galaxy m87. *The Astrophysical Journal*, *150*, L199. https://doi.org/10.1086/180125

Broadhurst, T., Benitez, N., Coe, D., Sharon, K., Zekser, K., White, R., Ford, H., Bouwens, R., Blakeslee, J., Clampin, M., Cross, N., Franx, M., Frye, B., Hartig, G., Illingworth, G., Infante, L., Menanteau, F., Meurer, G., Postman, M., … Zheng, W. (2005). Strong-lensing analysis of a1689 from deep advanced camera images. *The Astrophysical Journal*, *621*(1), 53–88. https://doi.org/10.1086/426494

Bruzual, G., & Charlot, S. (2003). Stellar population synthesis at the resolution of 2003. *Monthly Notices of the Royal Astronomical Society*, *344*, 1000–1028. https://doi.org/10.1046/j.1365-8711.2003.06897.x

Bryan, G. L., & Norman, M. L. (1998). Statistical properties of x-ray clusters: Analytic and numerical comparisons. *The Astrophysical Journal*, *495*, 80–99. https://doi.org/10.1086/305262

Bullock, J. S. (2002). Shapes of dark matter halos. *The Shapes of Galaxies and Their Dark Halos*, 109–113. https://doi.org/10.1142/9789812778017_0018

Carrasco, M., Zitrin, A., & Seidel, G. (2020). MIFAL: Fully automated multiple-image finder ALgorithm for strong-lens modelling – proof of concept. *Monthly Notices of the Royal Astronomical Society*, *491*(3), 3778–3792. https://doi.org/10.1093/mnras/stz3040

Clowe, D., Bradac, M., Gonzalez, A. H., Markevitch, M., Randall, S. W., Jones, C., & Zaritsky, D. (2006). A direct empirical proof of the existence of dark matter. *The Astrophysical Journal*, *648*(2), L109–L113. https://doi.org/10.1086/508162

Colaboration, P., Aghanim, N., Ashdown, M., Aumont, J., Baccigalupi, C., Ballardini, M., Banday, A. J., Barreiro, R. B., Bartolo, N., Basak, S., Battye, R., Benabed, K., Bernard, J.-P., Bersanelli, M., Bielewicz, P., Bock, J. J., Bond, J. R., Borrill, J., Bouchet, F. R., … Zonca, A. (2020). Planck 2018 results. VI. cosmological parameters. *Astronomy & Astrophysics*, *641*, A6. https://doi.org/10.1051/0004-6361/201833910

Collaboration, A., Price-Whelan, A. M., Lim, P. L., Earl, N., Starkman, N., Bradley, L., Shupe, D. L., Patil, A. A., Corrales, L., Brasseur, C. E., Nöthe, M., Donath, A., Tollerud, E., Morris, B. M., Ginsburg, A., Vaher, E., Weaver, B. A., Tocknell, J., Jamieson, W., … Zonca, A. (2022). The astropy project: Sustaining and growing a community-oriented open-source project and the latest major release (v5.0) of the core package. *The Astrophysical Journal*, *935*(2), 167. https://doi.org/10.3847/1538-4357/ac7c74

Cowie, L. L., & Perrenod, S. C. (1978). The origin and distribution of gas within rich clusters of galaxies - the evolution of cluster x-ray sources over cosmological time scales. *The Astrophysical Journal*, *219*, 354. https://doi.org/10.1086/155785

Dodelson, S. (2003). *Modern cosmology*. Academic Press.

Einasto, J. (1965). On the construction of a composite model for the galaxy and on the determination of the system of galactic parameters. *Trudy Astrofizicheskogo Instituta Alma-Ata*, *5*, 87–100. Retrieved February 23, 2026, from https://ui.adsabs.harvard.edu/abs/1965TrAlm...5...87E

Fabian, A. C. (1994). Cooling flows in clusters of galaxies. *Annual Review of Astronomy and Astrophysics*, *32*, 277–318. https://doi.org/10.1146/annurev.aa.32.090194.001425

Fabian, A. C., Sanders, J. S., Allen, S. W., Crawford, C. S., Iwasawa, K., Johnstone, R. M., Schmidt, R. W., & Taylor, G. B. (2003). A deep chandra observation of the perseus cluster: Shocks and ripples [ADS Bibcode: 2003MNRAS.344L..43F]. *Monthly Notices of the Royal Astronomical Society*, *344*, L43–L47. https://doi.org/10.1046/j.1365-8711.2003.06902.x

Forman, W., Kellogg, E., Gursky, H., Tananbaum, H., & Giacconi, R. (1972). Observations of the extended x-ray sources in the perseus and coma clusters from UHURU. *The Astrophysical Journal*, *178*, 309. https://doi.org/10.1086/151791

Gladders, M. D., López-Cruz, O., Yee, H. K. C., & Kodama, T. (1998). The slope of the cluster elliptical red sequence: A probe of cluster evolution. *The Astrophysical Journal*, *501*, 571–577. https://doi.org/10.1086/305858

Gunn, J. E., & Gott, J. R., Iii. (1972). On the infall of matter into clusters of galaxies and some effects on their evolution. *The Astrophysical Journal*, *176*, 1. https://doi.org/10.1086/151605

Guth, A. H. (2000). Inflation and eternal inflation. *Physics Reports*, *333-334*, 555–574. https://doi.org/10.1016/S0370-1573(00)00037-5

Harris, C. R., Millman, K. J., van der Walt, S. J., Gommers, R., Virtanen, P., Cournapeau, D., Wieser, E., Taylor, J., Berg, S., Smith, N. J., Kern, R., Picus, M., Hoyer, S., van Kerkwijk, M. H., Brett, M., Haldane, A., del Río, J. F., Wiebe, M., Peterson, P., ... Oliphant, T. E. (2020). Array programming with NumPy. *Nature*, *585*(7825), 357–362. https://doi.org/10.1038/s41586-020-2649-2

Hartley, P., Flamary, R., Jackson, N., Tagore, A. S., & Metcalf, R. B. (2017). Support vector machine classification of strong gravitational lenses. *Monthly Notices of the Royal Astronomical Society*, *471*(3), 3378–3397. https://doi.org/10.1093/mnras/stx1733

Hu, W., & Sugiyama, N. (1996).
Small scale cosmological perturbations: An analytic approach.
The Astrophysical Journal, *471*(2), 542–570. https://doi.org/10.1086/177989
Hunter, J. D. (2007). Matplotlib: A 2d graphics environment.
Computing in Science & Engineering, *9*(3), 90–95.
https://doi.org/10.1109/MCSE.2007.55
Jing, Y. P., & Suto, Y. (2002).
Triaxial modeling of halo density profiles with high-resolution n-body simulations.
The Astrophysical Journal, *574*, 538–553. https://doi.org/10.1086/341065
Jullo, E., & Kneib, J.-P. (2009).
Multiscale cluster lens mass mapping - i. strong lensing modelling.
Monthly Notices of the Royal Astronomical Society, *395*, 1319–1332.
https://doi.org/10.1111/j.1365-2966.2009.14654.x
Jullo, E., Kneib, J.-P., Limousin, M., Elíasdóttir, Á., Marshall, P. J., & Verdugo, T.
(2007). A bayesian approach to strong lensing modelling of galaxy clusters.
New Journal of Physics, *9*, 447. https://doi.org/10.1088/1367-2630/9/12/447
Kaiser, N. (1986). Evolution and clustering of rich clusters.
Monthly Notices of the Royal Astronomical Society, *222*(2), 323–345.
https://doi.org/10.1093/mnras/222.2.323
Kazantzidis, S., Zentner, A. R., & Kravtsov, A. V. (2006).
The robustness of dark matter density profiles in dissipationless mergers.
The Astrophysical Journal, *641*(2), 647–664. https://doi.org/10.1086/500579
Kneib, J.-P., & Natarajan, P. (2011). Cluster lenses.
The Astronomy and Astrophysics Review, *19*(1), 47.
https://doi.org/10.1007/s00159-011-0047-3
Kneib, J.-P., Ellis, R. S., Smail, I., Couch, W. J., & Sharples, R. M. (1996).
Hubble space telescope observations of the lensing cluster abell 2218.
The Astrophysical Journal, *471*(2), 643. https://doi.org/10.1086/177995
Kochanek, C. S. (2004, July 12). Gravitational lensing: Strong, weak and micro.
https://doi.org/10.48550/arXiv.astro-ph/0407232
Kravtsov, A., & Borgani, S. (2012). Formation of galaxy clusters.
Annual Review of Astronomy and Astrophysics, *50*(1), 353–409.
https://doi.org/10.1146/annurev-astro-081811-125502
Lecun, Y., Bottou, L., Bengio, Y., & Haffner, P. (1998).
Gradient-based learning applied to document recognition.
Proceedings of the IEEE, *86*(11), 2278–2324. https://doi.org/10.1109/5.726791
Liddle, A. R., & Lyth, D. H. (2000). *Cosmological inflation and large-scale structure.*
Cambridge University Press. https://doi.org/10.1017/CBO9781139175180
Lin, Y.-T., & Mohr, J. J. (2004). K-band properties of galaxy clusters and groups:
Brightest cluster galaxies and intracluster light.
The Astrophysical Journal, *617*(2), 879–895. https://doi.org/10.1086/425412

Lithwick, Y., & Dalal, N. (2011). Self-similar solutions of triaxial dark matter halos. *The Astrophysical Journal*, *734*(2), 100. https://doi.org/10.1088/0004-637X/734/2/100

Lotz, J. M., Koekemoer, A., Coe, D., Grogin, N., Capak, P., Mack, J., Anderson, J., Avila, R., Barker, E. A., Borncamp, D., Brammer, G., Durbin, M., Gunning, H., Hilbert, B., Jenkner, H., Khandrika, H., Levay, Z., Lucas, R. A., MacKenty, J., … Mountain, M. (2017). The frontier fields: Survey design and initial results. *The Astrophysical Journal*, *837*, 97. https://doi.org/10.3847/1538-4357/837/1/97

Lovisari, L., & Maughan, B. J. (2022). Scaling relations of clusters and groups, and their evolution. https://doi.org/10.1007/978-981-16-4544-0_118-1

Lynden-Bell, D. (1967). Statistical mechanics of violent relaxation in stellar systems. *Monthly Notices of the Royal Astronomical Society*, *136*, 101. https://doi.org/10.1093/mnras/136.1.101

Mahler, G., Sharon, K., Gladders, M. D., Bleem, L., Bayliss, M. B., Calzadilla, M. S., Floyd, B., Khullar, G., McDonald, M., Remolina González, J. D., Schrabback, T., Stark, A. A., & Van Den Busch, J. L. (2020). Strong lensing model of SPT-CL j0356–5337, a major merger candidate at redshift 1.0359. *The Astrophysical Journal*, *894*(2), 150. https://doi.org/10.3847/1538-4357/ab886b

McNamara, B. R., & Nulsen, P. E. J. (2007). Heating hot atmospheres with active galactic nuclei. *Annual Review of Astronomy and Astrophysics*, *45*, 117–175. https://doi.org/10.1146/annurev.astro.45.051806.110625

Merritt, D., Graham, A. W., Moore, B., Diemand, J., & Terzic, B. (2006). Empirical models for dark matter halos. i. nonparametric construction of density profiles and comparison with parametric models. *The Astronomical Journal*, *132*(6), 2685–2700. https://doi.org/10.1086/508988

Metcalf, R. B., Meneghetti, M., Avestruz, C., Bellagamba, F., Bom, C. R., Bertin, E., Cabanac, R., Courbin, F., Davies, A., Decencière, E., Flamary, R., Gavazzi, R., Geiger, M., Hartley, P., Huertas-Company, M., Jackson, N., Jullo, E., Kneib, J.-P., Koopmans, L. V. E., … Vernardos, G. (2019). The strong gravitational lens finding challenge. *Astronomy & Astrophysics*, *625*, A119. https://doi.org/10.1051/0004-6361/201832797

Miralda-Escude, J., & Fort, B. (1993). Gravitational lensing pairs in clusters of galaxies: A new probe to the high-redshift universe. *The Astrophysical Journal*, *417*, L5. https://doi.org/10.1086/187080

Natarajan, P., De Lucia, G., & Springel, V. (2007). Substructure in lensing clusters and simulations. *Monthly Notices of the Royal Astronomical Society*, *376*(1), 180–192. https://doi.org/10.1111/j.1365-2966.2007.11399.x

Natarajan, P., Kneib, J.-P., Smail, I., Treu, T., Ellis, R., Moran, S., Limousin, M., & Czoske, O. (2009). The survival of dark matter halos in the cluster cl 0024+16. *The Astrophysical Journal*, *693*(1), 970. https://doi.org/10.1088/0004-637X/693/1/970

Navarro, J. F., Frenk, C. S., & White, S. D. M. (1995). Simulations of x-ray clusters. *Monthly Notices of the Royal Astronomical Society*, *275*, 720–740. https://doi.org/10.1093/mnras/275.3.720

Navarro, J. F., Frenk, C. S., & White, S. D. M. (1996). The structure of cold dark matter halos. *The Astrophysical Journal*, *462*, 563. https://doi.org/10.1086/177173

Navarro, J. F., Frenk, C. S., & White, S. D. M. (1997). A universal density profile from hierarchical clustering. *The Astrophysical Journal*, *490*(2), 493–508. https://doi.org/10.1086/304888

Peacock, J. A. (1998). *Cosmological physics*. Cambridge University Press. https://doi.org/10.1017/CBO9780511804533

Peebles, P. J. E. (1980). *The large-scale structure of the universe*. Retrieved January 6, 2026, from https://ieeexplore.ieee.org/book/9453387

Peebles, P. J. E. (1982). Large-scale background temperature and mass fluctuations due to scale-invariant primeval perturbations. *The Astrophysical Journal*, *263*, L1. https://doi.org/10.1086/183911

Peterson, J. R., Kahn, S. M., Paerels, F. B. S., Kaastra, J. S., Tamura, T., Bleeker, J. A. M., Ferrigno, C., & Jernigan, J. G. (2003). High-resolution x-ray spectroscopic constraints on cooling-flow models for clusters of galaxies. *The Astrophysical Journal*, *590*, 207–224. https://doi.org/10.1086/374830

Pogson, N. (1856). Magnitudes of thirty-six of the minor planets for the first day of each month of the year 1857. *Monthly Notices of the Royal Astronomical Society*, *17*, 12–15. https://doi.org/10.1093/mnras/17.1.12

Press, W. H., & Schechter, P. (1974). Formation of galaxies and clusters of galaxies by self-similar gravitational condensation. *The Astrophysical Journal*, *187*, 425. https://doi.org/10.1086/152650

Refsdal, S. (1964). On the possibility of determining hubble's parameter and the masses of galaxies from the gravitational lens effect. *Monthly Notices of the Royal Astronomical Society*, *128*, 307. https://doi.org/10.1093/mnras/128.4.307

Robertson, B. E., Ellis, R. S., Furlanetto, S. R., & Dunlop, J. S. (2015). Cosmic reionization and early-forming galaxies: A joint analysis of new constraints from planck and the hubble space telescope. *The Astrophysical Journal*, *802*(2), L19. https://doi.org/10.1088/2041-8205/802/2/L19

Rykoff, E. S., Rozo, E., Busha, M. T., Cunha, C. E., Finoguenov, A., Evrard, A., Hao, J., Koester, B. P., Leauthaud, A., Nord, B., Pierre, M., Reddick, R., Sadibekova, T., Sheldon, E. S., & Wechsler, R. H. (2014).

redMaPPer i: Algorithm and SDSS DR8 catalog.
The Astrophysical Journal, *785*(2), 104.
https://doi.org/10.1088/0004-637X/785/2/104

Saha, P., & Williams, L. L. R. (1997).
Non-parametric reconstruction of the galaxy lens in PG 1115 + 080.
Monthly Notices of the Royal Astronomical Society, *292*(1), 148–156.
https://doi.org/10.1093/mnras/292.1.148

Sahu, K. C. (2021). WFC3 data handbook.
Retrieved June 5, 2026, from https://www.stsci.edu/files/live/sites/www/files/home/hst/instrumentation/wfc3/_documents/wfc3_dhb.pdf

Sarazin, C. L. (1986). X-ray emission from clusters of galaxies.
Reviews of Modern Physics, *58*(1), 1–115.
https://doi.org/10.1103/RevModPhys.58.1

Schneider, P., Ehlers, J., & Falco, E. E. (1992, January 1). *Gravitational lenses*.
https://doi.org/10.1007/978-3-662-03758-4

Schneider, P., & Sluse, D. (2013).
Mass-sheet degeneracy, power-law models and external convergence: Impact on the determination of the hubble constant from gravitational lensing.
Astronomy & Astrophysics, *559*, A37.
https://doi.org/10.1051/0004-6361/201321882

Seidel, G., & Bartelmann, M. (2007).
Arcfinder: An algorithm for the automatic detection of gravitational arcs.
Astronomy & Astrophysics, *472*(1), 341–352.
https://doi.org/10.1051/0004-6361:20066097

Smith, G., Mahler, G., Napier, K., Sharon, K., Bayliss, M., Benson, B., Bleem, L., Floyd, B., Gladders, M. D., Khullar, G., & Schrabback, T. (2025, August 18). The z=1.03 merging cluster SPT-CL j0356-5337: New strong lensing analysis with HST and MUSE. https://doi.org/10.48550/arXiv.2507.07404

Sonnenfeld, A., Chan, J. H. H., Shu, Y., More, A., Oguri, M., Suyu, S. H., Wong, K. C., Lee, C.-H., Coupon, J., Yonehara, A., Bolton, A. S., Jaelani, A. T., Tanaka, M., Miyazaki, S., & Komiyama, Y. (2018). Survey of gravitationally-lensed objects in HSC imaging (SuGOHI). i. automatic search for galaxy-scale strong lenses.
Publications of the Astronomical Society of Japan, *70*, S29.
https://doi.org/10.1093/pasj/psx062

Sparke, L. S., & Gallagher, J. S., III. (2007, February 1). *Galaxies in the universe*.
Retrieved February 21, 2026, from
https://ui.adsabs.harvard.edu/abs/2007gaun.book.....S

Staniszewski, Z., Ade, P. A. R., Aird, K. A., Benson, B. A., Bleem, L. E., Carlstrom, J. E., Chang, C. L., Cho, H.-M., Crawford, T. M., Crites, A. T., de Haan, T., Dobbs, M. A., Halverson, N. W., Holder, G. P., Holzapfel, W. L., Hrubes, J. D., Joy, M., Keisler, R., Lanting, T. M., . . . Zenteno, A. (2009).
Galaxy clusters discovered with a sunyaev-zel'dovich effect survey.

The Astrophysical Journal, *701*(1), 32.
https://doi.org/10.1088/0004-637X/701/1/32

Sunyaev, R. A., & Zeldovich, Y. B. (1972). The observations of relic radiation as a test of the nature of x-ray radiation from the clusters of galaxies. *Comments on Astrophysics and Space Physics*, *4*, 173. Retrieved February 22, 2026, from https://ui.adsabs.harvard.edu/abs/1972CoASP...4..173S

Suyu, S. H., Bonvin, V., Courbin, F., Fassnacht, C. D., Rusu, C. E., Sluse, D., Treu, T., Wong, K. C., Auger, M. W., Ding, X., Hilbert, S., Marshall, P. J., Rumbaugh, N., Sonnenfeld, A., Tewes, M., Tihhonova, O., Agnello, A., Blandford, R. D., Chen, G. C.-F., ... Spiniello, C. (2017). H0licow i. h_0 lenses in COSMOGRAIL's wellspring: Program overview. *Monthly Notices of the Royal Astronomical Society*, *468*(3), 2590–2604. https://doi.org/10.1093/mnras/stx483

Virtanen, P., Gommers, R., Oliphant, T. E., Haberland, M., Reddy, T., Cournapeau, D., Burovski, E., Peterson, P., Weckesser, W., Bright, J., van der Walt, S. J., Brett, M., Wilson, J., Millman, K. J., Mayorov, N., Nelson, A. R. J., Jones, E., Kern, R., Larson, E., ... van Mulbregt, P. (2020). SciPy 1.0: Fundamental algorithms for scientific computing in python. *Nature Methods*, *17*(3), 261–272. https://doi.org/10.1038/s41592-019-0686-2

Walsh, D., Carswell, R. F., & Weymann, R. J. (1979). 0957 + 561 a, b: Twin quasistellar objects or gravitational lens? *Nature*, *279*(5712), 381–384. https://doi.org/10.1038/279381a0

Weinberg, S. (1994, February 1). *Dreams of a final theory: The scientist's search for the ultimate laws of nature* [Google-Books-ID: Qd0MEtsBr7oC]. Knopf Doubleday Publishing Group.

Wen, Z. L., & Han, J. L. (2024). A catalog of 1.58 million clusters of galaxies identified from the DESI legacy imaging surveys. *The Astrophysical Journal Supplement Series*, *272*, 39. https://doi.org/10.3847/1538-4365/ad409d

Wen, Z. L., Han, J. L., & Liu, F. S. (2012). A catalog of 132,684 clusters of galaxies identified from sloan digital sky survey III. *The Astrophysical Journal Supplement Series*, *199*, 34. https://doi.org/10.1088/0067-0049/199/2/34

Wong, K. C., Dux, F., Shajib, A. J., Suyu, S. H., Millon, M., Mozumdar, P., Wells, P. R., Agnello, A., Birrer, S., Buckley-Geer, E. J., Courbin, F., Fassnacht, C. D., Frieman, J., Galan, A., Lin, H., Marshall, P. J., Poh, J., Schuldt, S., Sluse, D., & Treu, T. (2024). TDCOSMO. XVI. measurement of the hubble constant from the lensed quasar WGD$\,$2038$-$4008. *Astronomy & Astrophysics*, *689*, A168. https://doi.org/10.1051/0004-6361/202450979

Zeeman, E. C. (1976). Catastrophe theory. *Scientific American*, *234*(4), 65–83. Retrieved June 3, 2026, from https://www.jstor.org/stable/24950329

Zeldovich, Y. B., & Sunyaev, R. A. (1969).
The interaction of matter and radiation in a hot-model universe.
Astrophysics and Space Science, *4*(3), 301–316.
https://doi.org/10.1007/BF00661821

Zitrin, A., Fabris, A., Merten, J., Melchior, P., Meneghetti, M., Koekemoer, A., Coe, D., Maturi, M., Bartelmann, M., Postman, M., Umetsu, K., Seidel, G., Sendra, I., Broadhurst, T., Balestra, I., Biviano, A., Grillo, C., Mercurio, A., Nonino, M., . . . Moustakas, J. (2015).
Hubble space telescope combined strong and weak lensing analysis of the CLASH sample: Mass and magnification models and systematic uncertainties.
The Astrophysical Journal, *801*, 44.
https://doi.org/10.1088/0004-637X/801/1/44

Zwicky, F. (1937). On the masses of nebulae and of clusters of nebulae.
The Astrophysical Journal, *86*, 217. https://doi.org/10.1086/143864

Zwicky, F., Herzog, E., Wild, P., Karpowicz, M., & Kowal, C. T. (1961, January 1).
Catalogue of galaxies and of clusters of galaxies, vol. i. Retrieved April 24, 2026, from https://ui.adsabs.harvard.edu/abs/1961cgcg.book.....Z